Department of Physics and Astronomy

Heidelberg University

Master thesis

in Physics

submitted by

Miriam Lena Gerharz

born in Lahnstein

2021

Temporal phase and polarization interferometry at x-ray energies

---

Reconstruction of phase-related observables and temporal pulse shaping

This Master thesis has been carried out by

Miriam Lena Gerharz

at the

Max Planck Institute for Nuclear Physics

under the supervision of

apl. Prof. Dr. Jörg Evers

Temporäre Phasen- und Polarizationsinterferometrie im Röntgenbereich

Im Bereich der Röntgenquantenoptik sind viele experimentelle Schemata und Techniken, die im optischen Bereich weit verbreitet sind, schwer zu realisieren. Hauptschwierigkeiten sind Messungen von komplexen Phasen auf der Seite der Detektion und temporäre Pulsmodelierung auf der Lichtseite. In dieser Arbeit wird eine Methode zur Rekonstruktion komplexer Lichtfeld-Phasen und Bewegungen als mit Phasen verbundene Observablen entwickelt. Sie basiert auf temporärer Phaseninterferenz, wobei die Interferenz mit einer wohlbekannten Referenzprobe als Funktion der Zeit gemessen wird. Außerdem wird die experimentelle Realisierung von temporärer Pulsmanipulation inklusive der Erzeugung von Doppelpulsen mit Hilfe eines Polarizationsinterferometers demonstriert. Es ist das erste Experiment, das mechanisch induzierte Brechungsindexverstärkung nutzt, welche die Interferenz kontrolliert. Zusätzlich bietet das im Minimum betriebene Polarizationsinterferometer ein Werkzeug, um Hintergrundrauschen im Experiment zu analysieren. Dieses Rauschen beinhaltet das Vorhandensein von Schallwellen im Labor und in den Proben wie auch kleine unkontrollierte Bewegungen der Proben. Die in dieser Arbeit präsentierten Methoden sind unabhängig von der Wellenlänge und daher im Prinzip auf beliebige Energien übertragbar.

Temporal phase and polarization interferometry at x-ray energies

In x-ray quantum optics, many experimental schemes and techniques that are widely used at visible frequencies are hard to implement. Key difficulties are the measurement of complex phases on the detection side and temporal pulse shaping on the light source side. In this thesis, a method to reconstruct complex phases of light fields and motions as a phase-related observable from experimental data is developed. It is based on temporal phase interference, in which the interference with a well-known reference sample can be measured as a function of time. Furthermore, the experimental realization of temporal pulse shaping including the creation of double pulses with a polarization interferometer is demonstrated. It is the first experiment using mechanically-induced refractive index enhancement, which controls the polarization interference. In addition, the polarization interferometer operated at minimal intensity provides a tool to analyze background noise in the experiment. This noise includes the presence of sound waves both in the laboratory and in the samples as well as small uncontrolled vibrations of the samples. The presented methods in this thesis are not wavelength-dependent and can thus in principle be used at arbitrary energies.

Contents

Chapter 1

Introduction

In the middle of difficulty lies opportunity.

Albert Einstein

In this chapter, the work carried out within the scope of this thesis is motivated by giving an overview of the state of the art and indicating current problems. Afterwards, a short outline of the thesis is given.

Motivation

X-ray quantum optics is a relatively new field, that builds a bridge between standard quantum optics at visible frequencies and x-ray science [1]. Already right after their discovery by Röntgen in 1895 [2], especially in medicine, x-rays had important applications as an imaging tool [3]. X-ray diffraction also played a decisive role in resolving the structure of DNA [4, 5]. Nowadays, the associated sub-Ångstrom wavelengths are key to high resolution imaging [6] providing insight into the structures of the organic world, such as proteins [7] or viruses [8], as well as anorganic structures such as crystals [9]. Modern methods even allow to follow chemical reactions [10]. As an underlying concept, x-rays let us measure distances between atoms and molecules on the short scales [11] as well as properties of matter at relatively high energies [12, 13, 14].

Quantum optics on the other hand has become more and more relevant in the second half of last century after the first successful operation of a laser reported in 1960 [15]. Due to their well-known properties, lasers enable to measure and control light-matter interactions [16, 17]. Among the huge number of applications, these techniques give rise to atomic clocks [18], testing fundamentals of quantum physics [19, 20], quantum computing [21, 22], trapping and cooling of atoms [23, 24, 25], moving physical objects with optical tweezers [26] and high precision interferometry allowing to measure as tiny variations in length as caused by gravitational waves [27].

With the development of x-ray sources such as synchrotrons, especially in the last years, the field of x-ray quantum optics has become an active research field [1, 28, 29]. Several effects known from quantum optics in the optical regime have successfully been demonstrated in the x-ray regime as well. In x-ray quantum optics with electrons those are for example the Hanbury Brown-Twiss effect [30], ghost imag-

ing [31], two-photon X-ray spectroscopy [32, 33], time and energy correlations [34, 35, 36] and many more [1]. In nuclear quantum optics among others, the following schemes have been realized experimentally: collective Lamb shift [37], superradiance [38], electromagnetically induced transparency [39], spontaneously generated coherences [40] as well as coherent control of excitons [41]. In addition, experimental tools such as short x-ray pulse trains [42], entanglement [43] and dynamical control of light-matter interactions [44, 45] have been demonstrated.

The above named experiments show that in principle it is possible to transform successful schemes from the optical to the x-ray regime. One of the main difficulties is that current light sources, such as PETRA III at DESY in Hamburg [46] and ESRF in Grenoble [47], on average provide less than one resonant photon per pulse. Hence, only low intensity effects can be studied. New light sources, e.g. XFELs [48, 49], fourth generation synchrotrons [50, 51] and XFELOs [52], enable new promising experiments, that have already been performed [38] or are proposed [29, 39, 53, 54].

In nuclear quantum optics, on which we will focus in this thesis, synchrotron radiation is often used as the light source. On the matter side, Mössbauer nuclei play a key role because of their extreme properties. Due to the Mössbauer effect [55, 56], recoilless photon emission is possible as the entire lattice of the solid state body absorbes the photon momentum. Thus, while having a transition frequency above 10 keV (14.4 keV for ^{57}Fe), the linewidth is on the level of neV (4.7 neV for ^{57}Fe) [57], which makes nuclear transitions advantageous for precision spectroscopy [58, 59, 60]. Mössbauer spectroscopy has broad applications such as in geoscience [61], archaeology [62] and biochemistry [63]. A Mössbauer spectrometer was even send on a Mars mission giving evidence for water [64]. The corresponding long lifetimes of Mössbauer nuclei are favorable for measuring and manipulating the emitted light [41, 57, 65]. In addition, the decoherence is very low with quality factors on the level of the best optical clocks [18, 29, 66]. Mössbauer transitions can be seen as a two-level system [67] with low coherences and nearly no line broadening because of being in the solid state [57]. Therefore, they are a promising platform for qubits.

Although there are several interesting physical effects, here we will concentrate on interferometry. Several different types of interferometers, e.g. Michelson interferometer [68], Mach-Zehnder interferometer [69, 70], Fabry-Perot interferometer [71] and atom interferometers [72, 73], are widely used in different fields of physics [27, 68, 74, 75]. All of the named interferometers are spatial ones, i.e. the two paths are separated spatially. At x-ray energies, spatial interferometers are challenging because they need to be stabilized on the order of the wavelength, which is sub-Ångstrom for hard x-rays. Nonetheless, a Mach-Zehnder interferometer has been build from a single crystal [76].

Besides the widely-used spatial interferometry, where interference is encoded in spatial interference patters, also temporal phase interferometers exist. In those interferometers, the interference influences the temporal properties of the detected light [77]. A reference sample with a well-known phase is placed behind the sample to be analyzed and the relative phase between those samples is measured in time space. Here, the interference paths are given by the two samples. Those kind of

interferometers have also been realized at x-ray energies [78, 79].

A different interferometer is the polarization interferometer [80, 81]. Here, the two arms are represented by two orthogonal polarization states, e.g. created by a polarizing beam splitter. Also at x-ray energies, polarization interferometers have been demonstrated already [82].

Temporal phase and polarization interferometry are tools to tackle current problems at x-ray energies. Among other difficulties, phase and motion reconstruction, temporal pulse shaping and noise analysis in nuclear forward scattering are important topics and will be discussed in the following.

The phase of the complex electric field of the light is not directly measurable because conventional light detectors, such as e.g. avalanche photodiodes (APDs), only give access to intensities [83]. Knowledge on the phase relation is necessary for Fourier transforms from time to frequency space and vice versa. In addition, some effects only leave signatures in the phase and are thus not detectable. The lack of phase detection is known as the phase problem and is a severe issue at different wavelengths [84, 85], including hard x-ray energies. An early solution was to use the interference between the sample and a well known reference, the holographic principle proposed by Gabor in 1948 [86]. This is still the principal behind spectral [87, 88] and temporal phase interferometry [78, 79, 89], which among other techniques, e.g. ptychography [90], are used to retrieve phase information at x-ray energies. Some current phase reconstruction techniques at x-ray energies [78, 79] neglect the interaction between the two samples in temporal phase interferometry for simplicity. This approximation is only valid under certain conditions.

Connected to the reconstruction of complex phases of the light field is the reconstruction of small motions. Those motions usually leave strong signatures in the phase, which allows to extract the motion directly from the phase [41, 65, 79]. Small motions, on the sub-Ångstrom level, and their measurements are crucial in many fields, such as precision engineering [91], fundamental quantum physics [92], optomechanics [93] and measuring external influences, e.g. gravitational waves [27]. In addition, for motion-controlled experimental schemes like in [41, 65, 94, 95], the knowledge of the exact motion is necessary for its optimization and controllability. Currently used reconstruction schemes [41] are inefficient on measurement and evaluation. Especially, if several motions have to be reconstructed during an experiment for optimization and control, faster methods have to be used. In addition, it would be desirable to have a motion reconstruction scheme that does not depend on any model assumptions or material parameters.

Besides the detection systems, at hard x-ray energies also the light manipulation tools are limited. Because of the real part of the refractive index of any material being close to unity at those energies [14], using diffractive or refractive elements like at optical wavelength, e.g. waveplates, is restricted. Thus, alternative methods are necessary, resulting in the development of an impressive toolbox. Among those are deformable [96] or micromechanical mirrors [97, 98], rotational shutters [99] and off-Bragg phase modulation [100]. Adjustable methods include the use of sound waves [101, 102], piezoelectric [103] or photo-acoustic [104] diffraction con-

trol, magnetic [44] or optical properties switching [105] and mechanically-induced refractive index enhancement [94, 95]. Combined with a polarimeter the latter one builds a controllable polarization interferometer [95]. Temporal pulse shaping with a polarization interferometer has already been demonstrated in the optical regime [106]. At x-ray energies it can be used for fast and adaptive pulse shaping in temporal domain as proposed theoretically in [95] and provides an alternative to other techniques for temporal pulse shaping [41, 42, 107, 108, 109]. Especially the creation of pulse sequences is desirable, e.g. for Ramsey spectroscopy.

The polarization interferometer works at minimal intensity, such that noise disturbes the destructive interference. Because this reduces the visibility of controlled interference changes, noise reduction is desired. Therefore, it is necessary to understand the background noise in the experiment. Besides, in [41, 110] an Allan deviation [111] has been performed to characterize the stability of the system, but a systematic noise analysis has not been done. The setup in [41, 110] and the polarization interferometer are similar, such that a combined noise analysis is possible. An understanding of the background noise is necessary for the theoretical simulation and optimization of future experimental schemes.

Outline of thesis

In this thesis, experimental setups needed for the realization of quantum optical schemes at x-ray energies, such as phase and motion reconstruction, temporal pulse shaping and a noise analysis tool, are developed.

After this introduction, background information will be provided in Chapter 2. Besides the properties of ^{57}Fe as one of the most used Mössbauer nuclei and basic principles behind nuclear forward scattering, the standard experimental setup and data evaluation are explained.

The main part is divided into two parts. The first part (Chapters 3 and 4) focuses on temporal phase interferometry, while in the second part (Chapters 5 and 6) measurements with a controllable polarization interferometer are evaluated.

In Chapter 3, heterodyne phase reconstruction is introduced as one solution to the phase problem at x-ray energies. After explaining the basic setup of Callens et al. [78], the scheme is analyzed more closely. At quantum beat minima, interaction between sample and analyzer sample cannot be neglected anymore and new correction terms to the basic model by Callens et al. are introduced. Including those correction terms results in an extended heterodyne phase reconstruction that also works at intensity minima and has successfully been used on experimental data.

Chapter 4 presents and analyzes a new scheme for motion reconstruction that is based on heterodyne phase detection. The principal idea is that the motion-induced phase can be calculated as the difference between the phase in the static case and with motion. Similar to an idea originally presented in [79], the motion-induced phase directly gives the motion. As will be discussed, the new scheme is much more efficient than the one that was formerly used in [41, 65] both for measurement and

evaluation times. This improvement is essential to characterize several motions in real time during the experiment. In addition, the new method gives further insights into the computational steps because it needs much less model assumptions and material properties, such that intermediate results can be tested for plausibility.

The first experimental realization of temporal pulse shaping with polarization interferometry at x-ray energies as presented in [95] is investigated in Chapter 5. The central idea is to control the interference between the two samples in time domain by moving one of the two samples on the order of the wavelength. The light output from the interferometer is directly related to the samples' interference and can thus be controlled by the motion. It is demonstrated that temporal single pulse shaping is possible with this setup. Different experimental settings and parameters are analyzed. In addition, first proof of principle measurements for the creation of double pulses are performed. Those measurements demonstrate, that as proposed in [95], the controllable polarization interferometer can be used for temporal pulse shaping and creation of pulse trains.

Besides the pulse shaping, the polarization interferometer provides a new tool for background noise analyzes as explained in Chapter 6 because it operates close to minimal intensity. A new measurement mode is introduced, where sequences of 40 pulses are collected. A piezo motion is applied only for one pulse so that the motion decay can be studied over 39 bunches. This new mode allowed us to see sound waves traveling through the sample material because they leave a signature upon their revival about 15 bunches after the piezo motion is applied. This observation would not have been possible with the old mode with only four pulse sequences. Besides, the evolution of interference over the whole 40 bunches is evaluated. Furthermore, models for the background noise are tested. Those tests allow to model noise in future theoretical simulations of experimental schemes.

Finally, a summary and outlook are given in Chapter 7.

Chapter 2

Background

In this chapter the theoretical background of nuclear forward scattering exemplified by the isotope ^{57}Fe and experimental methods used in the evaluated experiments will be explained.

All spectra throughout this thesis are calculated with the software package `pynuss` [112], which is based on the software package `conuss` [113].

In Section 2.1 and Section 2.2, the basics of nuclear transition at the example of ^{57}Fe and the theory of nuclear forward scattering are explained, respectively. Afterwards, the influence of a moving sample is discussed in Section 2.3. The chapter ends with the experimental setup and data evaluation being explained in Section 2.4 and Section 2.5.

2.1 Nuclear transitions of ^{57}Fe

Throughout this thesis the magnetic dipole transition of ^{57}Fe as one of the most popular Mössbauer transitions [57] will be used. As a Mössbauer-active element it has a nearly recoil-free, resonant absorption and emission of x-rays.

In Fig. 2.1a the level scheme of ^{57}Fe is shown. In absence of a hyperfine field, this nucleus can be regarded as a simple two-level-system with transition frequency and wavelength [57, 114]

$$\omega_0 = 14.4\,\mathrm{keV}, \quad \lambda = 0.861\,\text{Å} \tag{2.1}$$

and linewidth [57, 114]

$$\gamma = 4.7\,\mathrm{neV}. \tag{2.2}$$

Already a weak external magnetic field of about 30 mT [115] can align the strong internal magnetic hyperfine field of 33 T caused by spin polarization [57]. Because the nuclear spins are $I_g = \frac{1}{2}$ and $I_e = \frac{3}{2}$ for the ground and excited state, respectively, hyperfine splitting occurs. In the case of an internal magnetic field of 33 T, we have a splitting of $\delta_g = 39.7\,\gamma$ and $\delta_e = 22.5\,\gamma$ for the ground and the excited state, respectively [114]. Due to the selection rules for magnetic dipoles, only the transitions with $m_e - m_g = 0, \pm 1$ can be driven. The properties of the six allowed transitions are given in Table 2.1. The six transitions have different detunings

$$\Delta_{\mathrm{hyp}} = \omega_0 - \omega_{\mathrm{transition}} = m_g \delta_g + m_e \delta_e. \tag{2.3}$$

Because of the selection rules, they also have different transition dipole moments. Their spatial arrangement is shown in Fig. 2.1b. The linearly polarized transitions

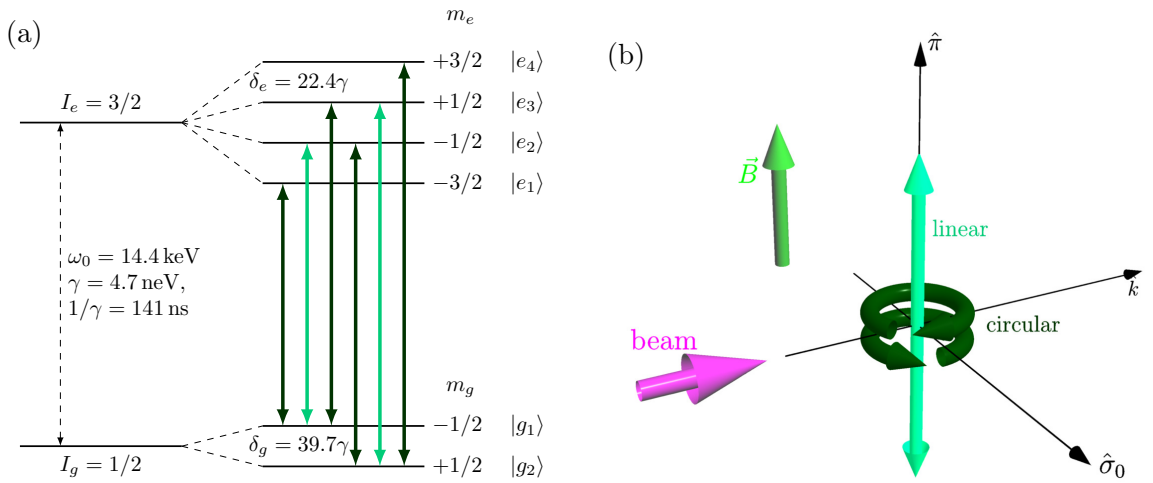

Figure 2.1: (a) The level scheme of the six M1 allowed transitions in ^{57}Fe. On the left side, the transitions without a magnetic hyper fine splitting can be seen. On the right side, the allowed transitions with the hyperfine splitting are displayed. Levelspacings are not to scale. (b) The polarization arrangement of the hyperfine splitted lines. Directions depend on the angle of the magnetic field $\vec{B}$. The $\hat{\pi}$-axis always points along the magnetic field. The colors in both figures indicate, whether the line is linearly (light green) or circularly (dark green) polarized.

n	Transition	m_g	m_e	Δ_{hyp}	Polarization	c_μ
1	$\|g_1\rangle \leftrightarrow \|e_1\rangle$	$-1/2$	$-3/2$	-53.6γ	σ_-	1
2	$\|g_1\rangle \leftrightarrow \|e_2\rangle$	$-1/2$	$-1/2$	-31.1γ	π^0	$\sqrt{2/3}$
3	$\|g_1\rangle \leftrightarrow \|e_3\rangle$	$-1/2$	$+1/2$	-8.6γ	σ_+	$\sqrt{1/3}$
4	$\|g_2\rangle \leftrightarrow \|e_2\rangle$	$1/2$	$-1/2$	8.6γ	σ_-	$\sqrt{1/3}$
5	$\|g_2\rangle \leftrightarrow \|e_3\rangle$	$1/2$	$+1/2$	31.1γ	π^0	$\sqrt{2/3}$
6	$\|g_2\rangle \leftrightarrow \|e_4\rangle$	$1/2$	$+3/2$	53.6γ	σ_+	1

Table 2.1: Properties of the six transition lines of ^{57}Fe adapted from [114]. Circular electric dipole moments are indicated by $\sigma_\pm$, linear ones by π^0. The six lines have different Clebsch-Gordan coefficients c_μ.

are always parallel to the orientation of the magnetic field, while the circular ones are perpendicular.

Throughout this thesis, when talking about light fields, without loss of generality we will always only consider the electric component because it is more familiar. If the incoming beam is linearly polarized in a certain direction, which usually is the case for synchrotron radiation, the orientation of the magnetic field determines which lines are driven. Thus, the direction of the magnetic field has to be described relative to the the beam polarization. Usually, this is described with two angles namely

- the inclination angle θ, i.e. the angle between beam propagation axis and the magnetic field,
- the azimuthal angle α, i.e. the angle between the magnetic field and the direction perpendicular to the linear polarization of the beam.

The perpendicular component in the definition of α is used because we have a magnetic dipole transition, but consider the electric field of the light.

Throughout this thesis, it is $\theta \approx \pi/2$ and the azimuthal angle α, that is sufficient to describe the orientation of the magnetic field in this case, is called angle of magnetization. This is illustrated in Fig. 2.2, where the incoming beam is assumed to be linearly polarized along the $\hat{\sigma}_0$-axis [116]. For example, in case of $\alpha = \pi/2$ only the two linear transitions are driven, while for $\alpha = 0$ this is the case only for the four circular transitions. Any angle in between results in all lines taking part in scattering processes.

From Table 2.1, it can be seen, that the frequency shifts caused by magnetic hyperfine splitting ($\Delta_{\mathrm{hyp}} < 252\,\mathrm{neV}$) are many orders of magnitude smaller than the transition frequency (14.4 keV). Therefore, the relevant energy scale is the detuning $\Delta = \omega - \omega_0$, which will be used throughout this thesis.

2.2 Nuclear forward scattering

A widespread scheme using Mössbauer nuclei is nuclear forward scattering. The principal setup is shown in Fig. 2.2. The sample of interest is excited, e.g. with synchrotron radiation or radioactive light sources, and the photons behind the sample are detected. Moving the sample on the order of wavelength, which can be done by placing it on a piezo electric element (piezo), and changing the angle of magnetization α influences the measured spectra. It can be shown that the forward direction is enhanced in the scattering process [29, 117].

2.2.1 Calculation of spectra

Within this thesis, we will always use synchrotron radiation as the input field. A synchrotron pulse is very short (bunch length of 44 psec at PETRA III [46]) compared to the characteristic time scale of the transition $\gamma^{-1} = 141\,\mathrm{ns}$. Hence, the

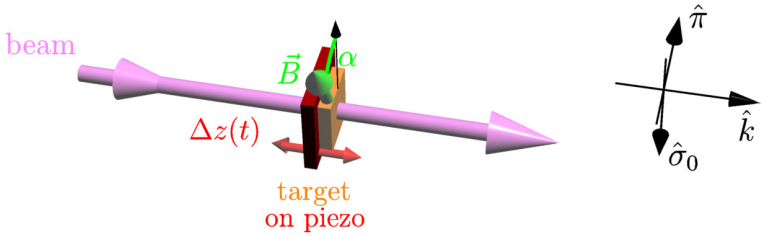

Figure 2.2: The basic setup of nuclear forward scattering. A sample (orange) is excited by appropriated x-ray light (pink), e.g. synchrotron radiation. The incoming light is assumed to be linearly polarized along the $\hat{\sigma}_0$-axis. The forward scattered light is detected with e.g. avalanche photodiodes (not shown). This detection typically is time resolved or by including an analyzer foil frequency resolved as well. The angle of magnetization α (green) is relative to the direction perpendicular to the incoming beam polarization. The sample can be mounted on a piezo electric element (red) to move it on the order of wavelength.

incoming field in time and frequency space can be described by a Dirac δ-function

$$E_{\text{in}}(t) = E_0\delta(t), \tag{2.4}$$

$$\hat{E}_{\text{in}}(\omega) = E_0, \tag{2.5}$$

where we used that the Fourier transform of $\delta(t)$ is 1 and omitted the factor of $\sqrt{2\pi}$ for simplicity. Throughout this chapter, if f is a function in time space, $\hat{f}$ describes the Fourier transform of f in frequency space. The constant E_0 defines the strength of the field.

In frequency space, the outgoing field $\hat{E}(\omega)$ is simply the product of the incoming field and a response function $\hat{R}(\omega)$ that describes the response of the sample to the incoming field

$$\hat{E}(\omega) = \hat{R}(\omega)\hat{E}_{\text{in}}(\omega). \tag{2.6}$$

Accordingly, due to the convolution theorem, in time space the outgoing field can be described by a convolution

$$E(t) = R(t) * E_{\text{in}}(t). \tag{2.7}$$

The measured spectra are then given by $I(t) = |E(t)|^2$ and $\hat{I}(\omega) = |\hat{E}(\omega)|^2$. Hence, the problem is solved if the response functions are known.

2.2.2 Response functions

Single line. For simplicity, we will first consider the case of a single line absorber, i.e. without hyperfine splitting. As we will see later (see Eqs. (2.12) and (2.13)), it is simple to include hyperfine splitting afterwards. We are mainly interested in the nuclear response, so we will neglect electronic contributions that lead to a small amount of absorption [65].

In frequency space, the response function of a single line absorber with transition frequency ω_0 and transition width γ is given by [118, 119]

$$\hat{R}(\omega) = \exp\left(\frac{-ib}{\omega - \omega_0 + \frac{i\gamma}{2}}\right), \tag{2.8}$$

where $b = \rho f_R \sigma_0 d\gamma/2$ is a material constant proportional to the thickness d, with ρ the sample density, z the sample thickness, σ_0 the absorption cross section at resonance and f_R the Lamb-Mössbauer factor. The response function in time space can be calculated via a Fourier transform

$$R(t) = \frac{1}{\sqrt{2\pi}} \int_{-\infty}^{\infty} \exp\left(\frac{-ib}{\omega - \omega_0 + \frac{i\gamma}{2}}\right) \exp(-i\omega t)\mathrm{d}\omega. \tag{2.9}$$

This integral cannot be solved straightforwardly, but with contour integration (see [119, 120]). Finally, the result reads

$$\begin{aligned} R(t) =& \delta(t) - \sqrt{\frac{b}{t}} J_1\left(2\sqrt{bt}\right) e^{-i\omega_0 t} e^{-\frac{\gamma}{2}t} \theta(t), & (2.10)\\ =& \delta(t) + R^S(t), & (2.11) \end{aligned}$$

with the Bessel function of first kind J_1. The prompt pulse, i.e. no interaction with sample, is represented by $\delta(t)$. The remaining part is the actual scattering response of the sample to the incident field, which will be denoted by $R^S(t)$. It can be divided into three different parts:

- $e^{-\frac{\gamma}{2}t}$ is the exponential decay,
- $e^{-i\omega_0 t}$ describes the free time evolution, a fast oscillation at the x-ray's carrier frequency that is not resolvable in experiments,
- $\sqrt{\frac{b}{t}} J_1\left(2\sqrt{bt}\right)$ represents thickness effects caused by the propagation through the sample. It has a minimum at $t = 58.74/b$ [121] called the dynamical beat, with b typically of order one

Several lines. The lines in Eq. (2.8) are centered around ω_0 and have a width of a few γ. If hyperfine splitting is taken into account, the transition frequency is slightly shifted from ω_0 to $\omega_0 + \Delta_{\mathrm{hyp}}$, where Δ_{hyp} is the according hyperfine shift. Because of the narrow absorption lines (a few γ) compared to their separation ($> 10\gamma$), we can neglect any interaction in frequency space and simply add up the lines weighted with the respective Clebsch-Gordan-coefficients c_μ [57]

$$\hat{R}^{\mathrm{hyp}}(\omega) = \sum_j c_\mu^j \exp\left(\frac{-ib}{\omega - (\omega_0 + \Delta_{\mathrm{hyp}}^j) + \frac{i\gamma}{2}}\right) = \sum_j c_\mu^j \exp\left(\frac{-ib}{\Delta - \Delta_{\mathrm{hyp}}^j + \frac{i\gamma}{2}}\right), \tag{2.12}$$

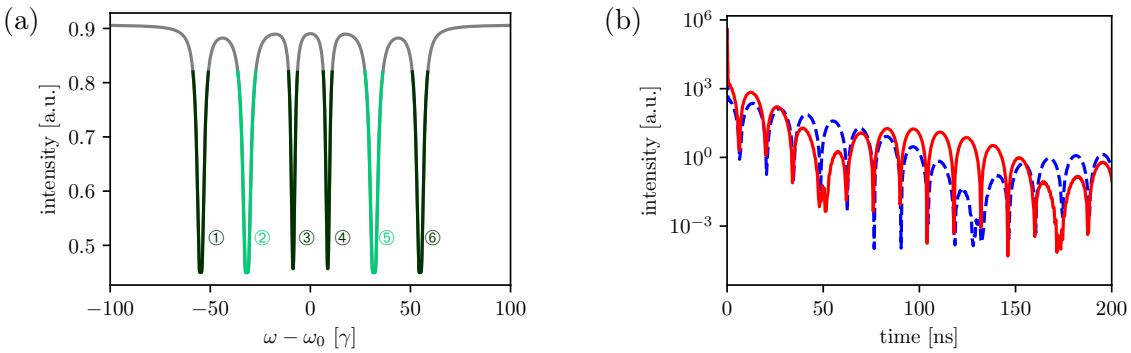

Figure 2.3: (a) The intensity is plotted against the detuning according to Eq. (2.12). The parameters in this equation are chosen to be $d = 2\,\mu$m and angle of magnetization $\alpha = \pi/4$ so that all allowed lines are driven. The colors indicate the polarization as in Fig. 2.1b. (b) A typical time spectrum is shown according to Eq. (2.13). Besides the decreasing intensity with oscillations due to quantum beats, the thickness d dependent dynamical beats can be seen. The blue (dashed) line is for a sample thickness of $d = 2\,\mu$m, the red (solid) one for $d = 5\,\mu$m. As expected, the dynamical beat is determined by $b \propto d$. The magnetic angle is chosen to be $\alpha = \pi/2$ so that only the two linear lines are driven for simplicity. The prompt pulse is indicated by the huge intensities close to 0 ns.

where j indicates the transition and Δ the detuning as defined above. An example spectrum, where all six allowed lines are driven, is shown in Fig. 2.3a. The absorption dips of the different transitions can clearly be seen.

Using linearity of the Fourier transform, in time space the contributions of the different lines can also simply be added up with shifted frequencies and according Clebsch-Gordan coefficients [57]

$$\begin{aligned} R^{\text{hyp}}(t) =& \sum_j c_\mu^j \left[\delta(t) - \sqrt{\frac{b}{t}} J_1(2\sqrt{bt}) e^{-i(\omega_0 + \Delta^j_{\text{hyp}})t} e^{-\frac{\gamma}{2}t} \theta(t) \right] \\ =& \delta(t) - \sqrt{\frac{b}{t}} J_1(2\sqrt{bt}) e^{-i\omega_0 t} e^{-\frac{\gamma}{2}t} \theta(t) \sum_j c_\mu^j e^{-i\Delta^j_{\text{hyp}} t} \\ =& \delta(t) - \underbrace{\sqrt{\frac{b}{t}} J_1(2\sqrt{bt}) e^{-i\omega_0 t} e^{-\frac{\gamma}{2}t} \theta(t)}_{R^{\text{no hyp}}(t)} \underbrace{2 \sum_k c_\mu^k \cos(\Delta^k_{\text{hyp}} t)}_{\text{quantum beats}}, \end{aligned} \tag{2.13}$$

where in the last line we used that driven lines always occur in pairs, that are indexed with k, with detunings $\pm\Delta^k_{\text{hyp}}$ as can be seen from Table 2.1. This sum over the pairs causes oscillations with frequency Δ^k_{hyp}, which are called quantum beats. The prefactor of this oscillation term is the response function without hyperfine splitting $R^{\text{no hyp}}(t)$ as in Eq. (2.10).

Two example time spectra with only the pair of linear lines driven for simplicity are shown in Fig. 2.3b. The exponential decay can be seen in the trend. The

minima of the envelope are caused by the dynamical beat and the thickness dependency is clearly visible. In addition, the quantum beats due to the slightly different frequencies of the two linear lines show up as the oscillating structure with minima separated by about 14 ns.

With polarization dependence. To take into account the different polarizations (see Table 2.1) of the allowed lines, the Jones matrix formalism will be used. The electric field is represented by a vector with the electric field components in $\hat{\sigma}_0$- and $\hat{\pi}$-direction as defined in Fig. 2.1b, where the $\hat{\pi}$-axis always points along the magnetic field and the $\hat{\sigma}_0$-axis is perpendicular to that. The representation with a two-dimensional vector is possible because all polarization dependencies only lie in the plane perpendicular to the beam propagation direction. The linearly (circularly) polarized transitions can only interact with components in $\hat{\pi}(\hat{\sigma}_0)$-direction. Hence, the polarization dependent outgoing field in frequency space is given by [57, 122]

$$\hat{\vec{E}}(\omega) = \begin{pmatrix} \hat{R}_{\mathrm{circ}}(\omega) & 0 \\ 0 & \hat{R}_{\mathrm{lin}}(\omega) \end{pmatrix} \hat{\vec{E}}_{\mathrm{in}}(\omega), \tag{2.14}$$

where $\vec{R}_{\mathrm{circ}}(\omega)$ ($\vec{R}_{\mathrm{lin}}(\omega)$) is the response function summed up over all circular (linear) polarizations. Again, a Fourier transform can be used to give the result in time space.

Thin target approximation. For $t < 4/b$, i. e. short times or thin samples, we can Taylor expand the Bessel functions

$$\frac{J_1(2\sqrt{bt})}{\sqrt{bt}} \approx 1 - \frac{bt}{2} + \frac{b^2t^2}{12} + \mathcal{O}\left(b^3t^3\right). \tag{2.15}$$

Comparing to the Taylor expansion of the exponential function,

$$e^{-bt/2} \approx 1 - \frac{bt}{2} + \frac{b^2t^2}{8}, \tag{2.16}$$

we can approximate

$$\frac{J_1(2\sqrt{bt})}{\sqrt{bt}} \approx e^{-bt/2}. \tag{2.17}$$

With this approximation Eq. (2.10) becomes

$$R(t) \approx \delta(t) - be^{-i\omega_0 t}e^{-\left(\frac{\gamma}{2}+\frac{b}{2}\right)t}\theta(t). \tag{2.18}$$

This approximation is sometimes used to analytically calculate the output signal because it simplifies the expressions significantly.

2.2.3 Combining several samples

After describing the interaction of one sample with a synchrotron pulse, the calculation will now be extended to several samples in a row. To calculate the electric field behind the j-th sample, the output field after the $(j-1)$-th sample can be used as input field in Eq. (2.4) so that

$$\hat{E}_j(\omega) = \hat{R}_j(\omega)\hat{E}_{j-1}(\omega). \tag{2.19}$$

Hence, the response function of N samples in a row is given by

$$\hat{R}(\omega) = \prod_{j=1}^{N} \hat{R}_j(\omega). \tag{2.20}$$

In time space, convolutions have to be used instead of the products.

Let us consider the special case of two samples in time domain. The combined response is given by

$$\begin{aligned} R(t) =& R_1(t) * R_2(t) \\ =& \left[\delta(t) + R_1^S(t)\right] * \left[\delta(t) + R_2^S(t)\right] \\ =& \delta(t) + R_1^S(t) + R_2^S(t) + R_1^S(t) * R_2^S(t), \end{aligned} \tag{2.21}$$

where we used $R_i(t) = \delta(t) + R_i^S(t)$ (see Eq. (2.11)) in the second line and $f(t) * \delta(t) = f(t)$ for an arbitrary function $f(t)$ in the last line. The four different scattering paths are represented by the four different terms:

- $\delta(t)$ is the prompt pulse where no scattering with any sample occurs,
- $R_1^S(t)$ represents the paths where scattering only takes place in first sample and not in the second sample,
- $R_2^S(t)$ describes the other single sample interaction with only the second sample,
- $R_1^S(t) * R_2^S(t)$ expresses the interference path in which scattering occurs in both samples.

In general, this last convolution is hard to compute analytically. Numerical calculation approaches often use the fact that it is a simple multiplication in frequency space and a discrete Fourier transform can be used to go from time space to frequency space and vice versa.

2.3 Moving sample

Moving a sample on sub-Ångstrom level induces a controlled phase shift in the response function, which enables to control the interference of the prompt pulse and the sample response by the phase $e^{ikx(t)}$ as shown in Fig. 2.4. The main work on the theoretical description was done in [119].

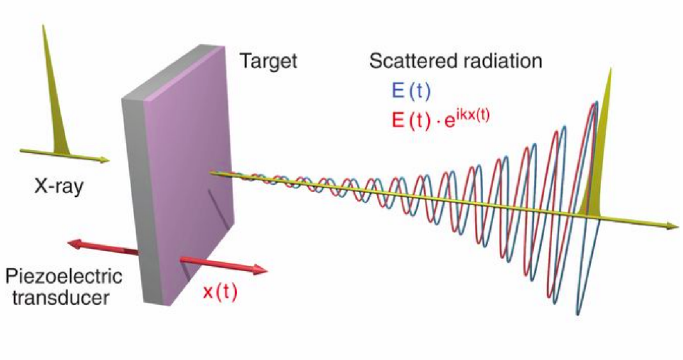

Figure 2.4: Influence of a moving sample (pink) on the interaction with the prompt pulse (yellow). The displacement, which is realized by a piezoelectric element (gray), adds an additional phase $e^{ikx(t)}$ (red) to the electric field in the static case (blue). Taken from [65].

2.3.1 Computational strategy

We already know what the response functions look like in case of a static sample, which would be the appropriate description in the rest frame of the target. Hence, the main idea is to include the motion by a transformation between the laboratory and rest frame of the target [65, supplement].

Because the sample motion $x(t)$ is not fast enough so that relativistic effects could play a role, the incident field $E_{\text{in}}(t) = \delta(t)$ in the laboratory frame can be represented in the rest frame of the sample by

$$\tilde{E}_{\text{in}}(t) = E_{\text{in}}(t)e^{-ikx(t)} = \delta(t)e^{-ikx(0)}, \tag{2.22}$$

where k is the wave number. In the second step we used that $\delta(t)$ only has contributions at $t = 0$. In the lab frame, we can use Eqs. (2.4) and (2.11) to find

$$\begin{aligned}\tilde{E}(t) =& R(t) * \tilde{E}_{\text{in}}(t) \\ =& \left[\delta(t) + R^S(t)\right] * \left[\delta(t)e^{-ikx(0)}\right] \\ =& \left[\delta(t) + R^S(t)\right] e^{-ikx(0)}.\end{aligned} \tag{2.23}$$

Similar to Eq. (2.22), the back transformation can be performed

$$\begin{aligned}E(t) =& \tilde{E}(t)e^{ikx(t)} \\ =& \left[\delta(t) + R^S(t)\right] e^{-ikx(0)}e^{ikx(t)} \\ =& \delta(t) + R^S(t)e^{ik(x(t)-x(0))},\end{aligned} \tag{2.24}$$

where in the last step we again used that the δ-function only has a contribution at $t = 0$ so that the exponentials cancel each other. Only the relative displacement of the sample is relevant so that we can set $x(0) = 0$ and find

$$E(t) = \delta(t) + R^S(t)e^{ikx(t)}. \tag{2.25}$$

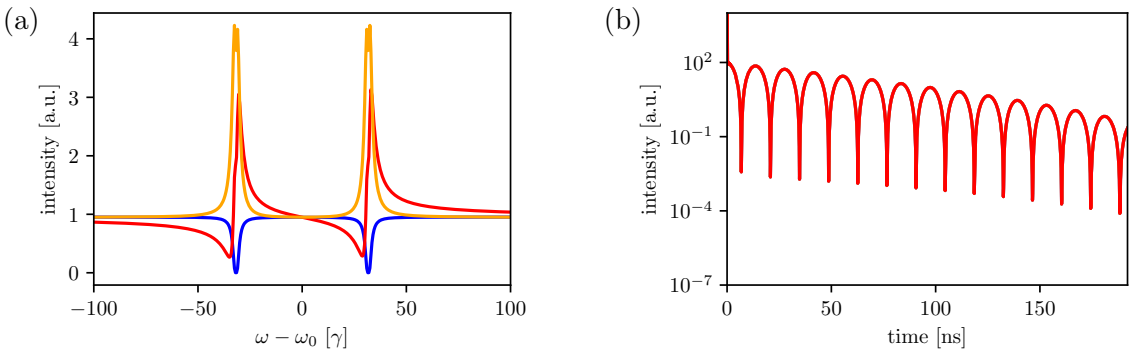

Figure 2.5: Frequency (a) and time spectra (b) are shown for different displacements: static (blue), $x_0 = \lambda/4$ (red) and $x_0 = \lambda/2$ (orange). The sample thickness is $d = 1\,\mu$m and $\alpha = \pi/2$. The frequency spectra show different line shapes, absorption dips for static case, Fano line shapes for $x_0 = \lambda/4$ and intensity enhancement for $x_0 = \lambda/2$, while the time spectra are identical.

The motion induces a phase shift $e^{ikx(t)}$ to the scattering part of the response function. This phase can also be understood intuitively: First, it is clear that there cannot be a phase shift in the prompt part of the response function because this part does not interact with the sample at all. Second, any plane wave propagates through space by picking up a phase e^{ikx}. Hence, shifting the source point of the wave, the x-coordinate has to be changed accordingly.

Except in case of $t = 0$, the phase will be cancelled out in the measured time spectra so that the intensities in time space look the same for the different motions as displayed in Fig. 2.5b. However, this is not the case in frequency space because there the prompt pulse is distributed uniformly over all frequencies. Thus, the motion-induced phase controls the interference between prompt pulse and light emitted by the sample in frequency space (see Fig. 2.5a).

In experimental settings, there is a bandwidth of different frequencies in the synchrotron pulse because of its shortness. It is possible to limit the bandwidth of this pulse on meV level so that the variation in k is small compared to the absolute value (about 6 orders of magnitude) [120]. Hence, the variations can be neglected and k be assumed to be the same for all six transitions.

Controlling the sample motion $x(t)$ on sub-Ångstrom-level results in phases between 0 and 2π.

2.3.2 Instantaneous jump

With the framework for moving sample at hand, we want to illustrate the effect at the simple example of an instantaneous jump at $t = 0$

$$x(t) = x_0\theta(t). \tag{2.26}$$

Plugging Eqs. (2.10) and (2.26) into Eq. (2.25) gives

$$E(x_0,t) = \delta(t) - e^{-ikx_0\theta(t)}\sqrt{\frac{b}{t}}J_1(2\sqrt{bt})e^{-i\omega_0 t}e^{-\frac{\gamma}{2}t}\theta(t). \tag{2.27}$$

The electric field in frequency domain can be calculated via a Fourier transform

$$\begin{aligned}\hat{E}(\omega) =& \int_{-\infty}^{\infty} E(x_0,t)e^{i\omega t}\mathrm{d}t \\ =& 1 - \int_{-\infty}^{\infty} e^{-ikx_0\theta(t)}\sqrt{\frac{b}{t}}J_1(2\sqrt{bt})e^{-i\omega_0 t}e^{-\frac{\gamma}{2}t}\mathrm{d}t \\ =& 1 - e^{-ikx_0}\int_{0}^{\infty}\sqrt{\frac{b}{t}}J_1(2\sqrt{bt})e^{-i\omega_0 t}e^{-\frac{\gamma}{2}t}\mathrm{d}t,\end{aligned} \tag{2.28}$$

where in the last step we used that $e^{-ikx_0\theta(t)} = e^{-ikx_0}$ for $t > 0$. The variation at $t = 0$ can be ignored because its measure is zero so that it does not contribute to the integral. The remaining integral expression is $R^S(t)$. Hence, by using Eqs. (2.9) and (2.11) we find

$$\hat{E}(\omega) = 1 + e^{ikx_0}\left(\frac{-ib}{\Delta + i\frac{\gamma}{2}} - 1\right). \tag{2.29}$$

The first part gives the spectral baseline from the incident pulse, the second term the phase controlled sample interference with the uniform prompt pulse. From this expression, we can see that for different phases all kinds of Fano-lines are possible for different x_0. Spectra for different x_0 are shown in Fig. 2.5. While the frequency spectra differ significantly, the time spectra are all the same.

Choosing $x_0 = \lambda/2$ as in [65] gives a phase of $e^{ik\lambda/2} = -1$ and thus

$$\hat{E}(\omega) = 2 - \frac{-ib}{\Delta + i\frac{\gamma}{2}}. \tag{2.30}$$

The frequency dependent part, that is responsible for absorption dips, has the opposite sign now so that absorption dips turn into intensity enhancement [65] at those frequencies (see Fig. 2.5).

2.3.3 Arbitrary motions

In experiments, a step function as discussed above usually is not possible. Instead, the motion would have a certain rise time (see figs. 2.6a and 2.7b). Luckily, those risetimes do not change the spectra much (see Fig. 2.6b). The more realistic motion causes a Doppler shift because of finite velocities on the rising edge, which is responsible for the asymmetry in the spectra [65, supplement].

Arbitrary motions can be evaluated in a similar fashion: Transforming into the rest frame of target, evaluating the response there and transforming back into the laboratory frame. The problem is that for arbitrary motions the integral in the Fourier transformation may not be solvable analytically. However, the integral is not a problem for simulations because a discrete Fourier transforms can be used.

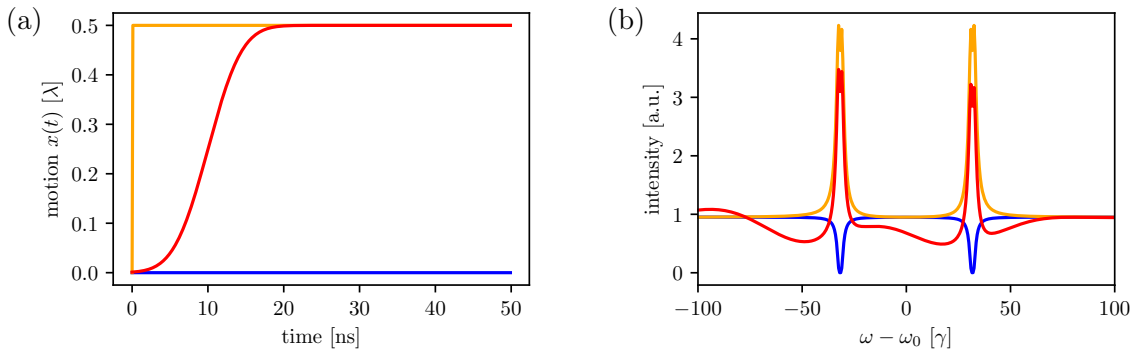

Figure 2.6: Three different motions and their corresponding frequency spectra are shown: static case (blue), the discussed step function (orange) and a more realistic function with a certain rise time (red). The non-instantaneous motion causes a Doppler shift during the rise, which is responsible for the asymmetry in the spectra [65, supplement].

2.4 Experimental setup

In this section, the experimental setup for nuclear forward scattering with a moving sample will be explained. The goal is to measure, time and frequency spectra as well as 2D spectra, in which both information is combined, and to characterize the piezo motion.

2.4.1 Setup and detection system

Setup. The experimental setup is shown in Fig. 2.7a. The sample is mounted on a piezoelectric element (piezo) so that it can be moved in a controlled way on the level of the wavelength. Which of the six sample transitions are driven, is selected by aligning the external field. In forward scattering direction a single-line analyzer, here a stainless-steel foil, on a Mössbauer drive, that can move the analyzer with different velocities, and avalanche photodiodes (APDs) are placed. As light input, synchrotron radiation is used. The experimental data shown in Chapters 3 to 6 were taken at beamline P01 at DESY [116], which has a pulse separation of 192 ns [46].

Detection. Our detection system with the combination of a Mössbauer drive and APDs allows event-based detection. That means that for every arriving photon, energy and time information can be stored among other quantities. Thus, 2D spectra with frequency and time information can be measured (see Fig. 2.7b). Those 2D spectra contain enough information to extract intensity and phase of the electric field. The first few nanoseconds are excluded by a veto because in this range the detection does not work properly as it still tries to handle the massive counts from the prompt pulse. For more details on the detection scheme see [41].

The signatures of the resonances are clearly visible in the 2D spectra, especially at late times. In Fig. 2.7b, only the two linear lines are driven. Thus, pseudo

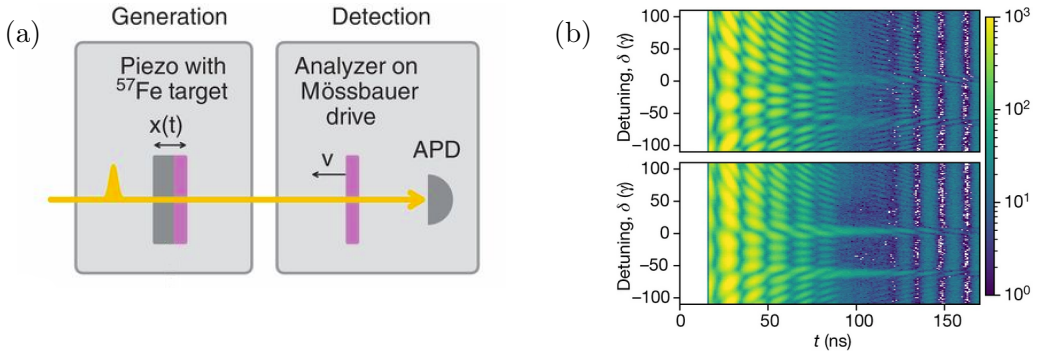

Figure 2.7: (a) The standard experimental setup adapted from [65]. A short (ps) synchrotron pulse (yellow) interacts with the sample (purple). The latter is mounted on a piezoelectric element (piezo, gray) so that it can be moved in a controlled way on sub-Ångstrom level. The detection system consists of avalanche photodiodes (APDs) for time spectra and a single line analyzer on a Mössbauer drive to measure 2D spectra in addition. A magnet (not shown) is used to align the internal magnetic field and hence select the driven lines. (b) Two 2D example spectra taken from [41]. The number of photon counts is shown as a function of the Mössbauer detuning Δ (δ in figure) and time t. White areas indicate no counts.

frequency spectra can be created by the so-called late-time integration. In this method, the 2D spectra are integrated over late times, e.g. after 100 ns, which traces out the modulation with time. At earlier times, there are a lot of structures off the resonances, which would falsify the frequency spectra if integrating over the whole time range. More details on this method can be found in [57, 114].

2.4.2 Moving samples

About 1 μm thick α-iron foils enriched in ^{57}Fe to 95% are placed on a thin polyvinylidene fluoride piezoelectric transducer (DT1-028K/DT1-052K, Measurement Special-

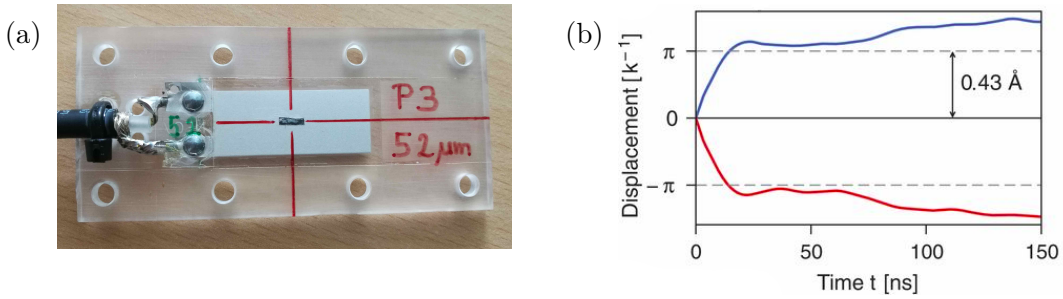

Figure 2.8: (a) A sample consisting of a thin foil enriched with ^{57}Fe (about 1 mm × 3 mm) glued on a piezoelectric element (about 1 cm × 3 cm). A 4 mm-thick acrylic glass plate stabilizes the sample. (b) Two reconstructed example motions of the piezo are shown. The amplitude of 0.43 Å corresponds to $\lambda/2$ and hence a phase shift of $\phi = k\Delta x = \pi$. Taken from [65].

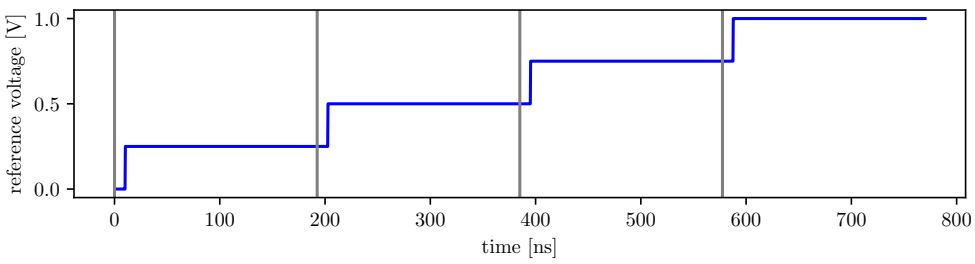

Figure 2.9: An example reference voltage for a motion, that covers a four bunch cycle. Gray lines indicate the arrivals of the x-rays. The rising edges should be within the veto time, in which no data is collected because the APDs still handle the photons from the prompt pulse. The voltage of the reference ramp is a clear identifier of the bunch number in the four bunch sequence.

ities Inc) [123], called piezo in the following. For stability, this altogether is glued onto a 4 mm thick acrylic glass plate. An example can be found in Fig. 2.8a.

The voltage pattern for the piezo is generated by an Agilent arbitrary waveform generator (Keysight 81160A-002 [124]) called agilent. Two example measured motions are shown in Fig. 2.8b. They have a rise time of about 20 ns until they reach a phase jump of about π. For roughly the next 50 ns, they stay relatively constant before slightly drifting away.

Usually we want a motion to last for 4 bunches to directly compare different motion patterns such as piezo contraction, expansion or no motion. In principle, those comparisons could also be done in separate measurements, but if any noise drifts with time, the drifts would distort the results.

To sort the data into the correct 2D spectrum, a reference voltage is collected as well by the detection system for every arriving photon. The reference voltage is a step function with as many steps as bunches covered by the motion. Hence, the voltage of this reference ramp is a unique identifier of the bunch number within the motional sequence. An example reference ramp for 4 bunches is displayed in Fig. 2.9. If possible, the rising edges of the reference voltage should be placed in the veto regime (here at 10 ns), where no data is collected. Otherwise data might be lost because on the rising edge sorting into the correct bunch is difficult.

2.5 Data evaluation

The principal evaluation toolchain for live evaluation during the experiment as well as basic evaluation after the experiment is displayed in Fig. 2.10. It can divided into four main parts: data processing, calibrations, motion reconstruction and output of data..

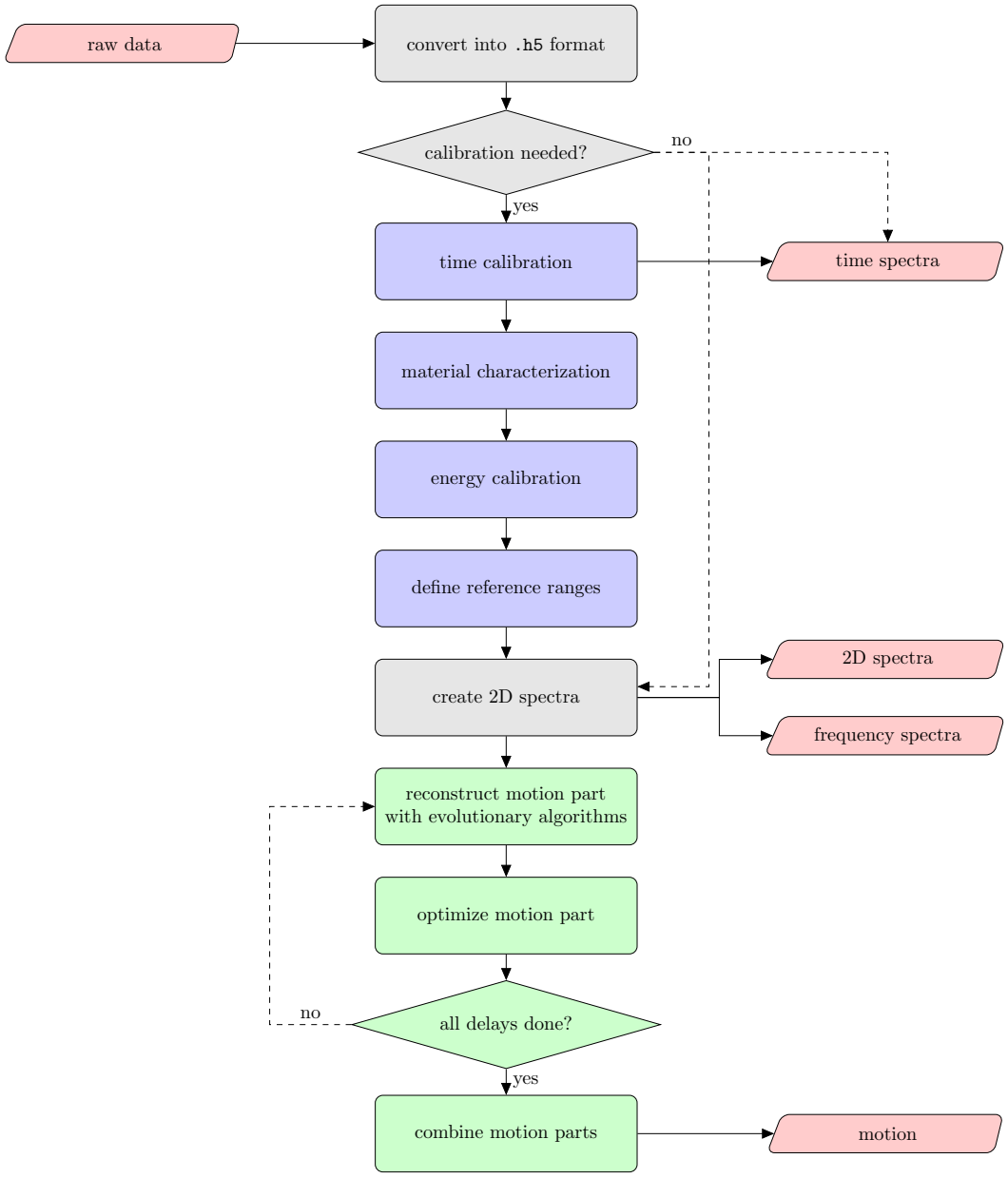

Figure 2.10: The principal toolchain to evaluate the experimental data is shown. Red indicates in and output, gray data processing steps, blue calibration steps and green the motion reconstruction steps. Because with the old method presented in Section 2.5.3 only up to 55 ns of the motion can be reconstructed from one 2D spectrum, but the motion lasting for 192 ns, different delays of the motion need to be measured (see Fig. 2.11). More details on the toolchain can be found in main text.

2.5.1 Data processing

The data processing steps are the gray ones in Fig. 2.10. At first, the raw data from the RoentDek box is converted into a hierarchical data format (`.h5`), for better usability. The new data is still event-based selection. After calibrating time and energy range (see Section 2.5.2), all photon counts can be sorted into the 2D spectra with time and frequency information as shown in Fig. 2.7b.

2.5.2 Calibrations

The calibration consists of several steps indicated by blue boxes in the toolchain (see Fig. 2.10).

Time calibration. The detection system can detect the time delay between the bunch clock, that is a signal triggered to the pulse arrival, and the photon arrival on the detector. The only problem is that there are time shifts because of cable lengths on the order of about 3 ns per meter because the signal travels with the finite speed of light. As not all cable lengths are known and time scale is on ns level, a time calibration is necessary. Without any motion, the time shift is only defined up to a multiple of the bunch clock repetition of 192 ns. For ^{57}-Fe, the time spectrum is well known qualitatively so that we just need to find its starting points and have the time calibration.

Material characterisations. The properties of the samples can be determined by fitting calculated time spectra to the measured ones. Possible material properties, that can be found by fitting are [110]

- thickness of sample (incl. distribution)
- strength of internal magnetic hyperfine field (incl. distribution)
- angle of magnetization α (incl. distribution)
- angle between beam propagation and orientation of magnetic field θ (incl. distribution)
- isomer shift (incl. distribution)
- quadrupole splitting (incl. distribution)

Typically thickness, magnetic angle, angle between magnetic field and foil plane and strength of internal field are fitted for α-iron foils, isomer shift and thickness for stainless steel foils.

The function to be minimized, which is given by the difference between measured and calculated spectrum in Poissonian metric [41, 125], has many local minima so that evolutionary algorithms (see Section 2.5.4) are used to find the rough global minimum. This rough estimate can be optimized by standard fit routines like Nelder-Mead to find the actual global minimum.

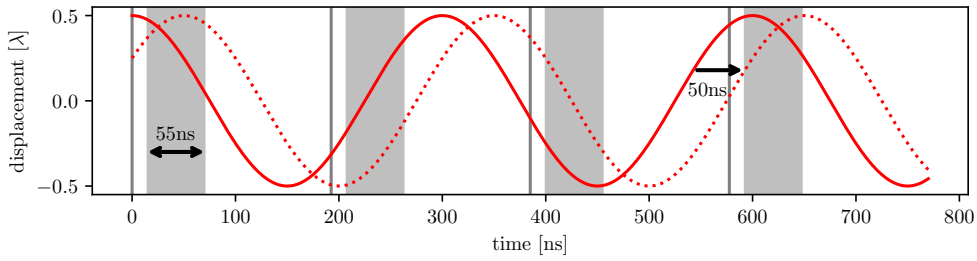

Figure 2.11: Illustration on how different delays can be used to cover the whole motion while the reconstruction time is limited to 55 ns. The solid line shows the motion without delay, while the dotted curve illustrates the same motion delayed by 50 ns. The delay shifts new motion parts into the reconstruction time window (gray areas) starting 15 ns after the pulse arrival (gray lines) and ending at 70 ns. The pulse separation is 192 ns like at DESY.

Energy calibration. Using the fitted material properties, 2D spectra can be calculated and compared to the measured ones. For the calculated ones, the position of the resonances is exactly known so that the frequency axis of the 2D spectra can be calibrated.

Defining reference ranges. As said above, the motion usually covers more than one bunch. To identify to which bunch of the motion a detected photon belongs a reference voltage signal is detected for the voltage limits. An example for four bunch mode, i.e. motion lasting over four bunches, is given in Fig. 2.9. The reference voltage is a unique identifier of each bunch in the four bunch cycle.

Because we want 2D histograms for each motion part separately, appropriate limits have to be defined. The reference ramp has rising edges when switching to the next voltage level. Hence, at those points the bunch identification by the reference ramp is difficult and the data is not sorted into the different bunches properly. The rising edges have no influence if they are set in the veto region.

2.5.3 Reconstruction of motion

The reconstruction of motion represented by the green steps in Fig. 2.10 needs to be done for different delays as discussed below to cover the whole motion.

In general, the actual motion is expected to differ from the applied voltage pattern. In addition, time shifts occur like explained above for the time calibration (Section 2.5.2). Thus, the motion has to be determined by fitting routines. The 2D spectra contain enough information to uniquely reconstruct the motion by comparing the measured spectrum to a calculated one with the function to be fitted.

Fitting the motion point by point has too many free parameters. Hence, we fit bivariate splines [126], that represent the motion. They represent an arbitrary function by $N-1$ piece wise polynomials between N so called support points. In our case, the polynomials are chosen to be cubic. With appropriate boundary values,

those polynomials can be represented by a single number called slope in the following. For more details see [126]. Hence, only the $N-1$ slopes have to be optimized.

To compare spline and experimental data, a Poissonian metric is used [41, 125]. The residual sum calculated with this metric will be called fitness in the following.

In a first step a spline will be fitted to the 2D spectra by using evolutionary algorithms (more details in Section 2.5.4 or [41]). In general, there is no good first guess for the motion so that standard fit routines would only find a local minimum, while evolutionary algorithms are able to find the environment of the global minimum. This step needs considerable computational resources, such that it has be done on the institute's high performance computer.

Second, this result can be used as initial parameters to optimize the result with standard optimization methods (here Nelder-Mead [127]).

Typically, the whole reconstruction can only be trusted in the first 55 ns after the veto. Because of a pulse separation of e.g. 192 ns at DESY [46], one 2D spectrum is not enough to reconstruct the complete motion. An illustration can be found in Fig. 2.11. The motion can only be reconstructed in the shaded areas. Delaying the motion by 50 ns shifts other parts of the motion into the reconstruction time window of the first 55 ns after the veto. Several measurements are needed with the motion being shifted by different delays so that every part of the motion is within the reconstruction time window from 15 ns to 70 ns at least once. Typically, the delay is chosen in steps of 25 ns to have an overlapping regime for consistency checks.

After the reconstruction of the motion parts for different delays, they can be combined into one motion again. First, the motion parts are sorted by their starting points. After the sorting, they are appended step by step. Because earlier times are more trustworthy, whenever there is an overlap between two motion parts, the one with later starting time is used in this region.

The delay spacing is chosen in such a way that there is enough overlap, to exclude some motion parts from combination to optimize the periodicity of the resulting motion. Two example motions are shown in Fig. 2.7b. For more details on the standard reconstruction method see [41], [65, supplement].

2.5.4 Evolutionary algorithms

In some of the above mentioned fitting routines, many local minima exist. Standard fit methods such as the used Nelder-Mead can only find a local minimum, but no global minimum. Depending on the starting parameters of the fitting routine, the global minimum might not be found because the fit converges in the local minimum.

One solution to this problem is given by evolutionary algorithms [128, 129]. The key idea is to implement some randomness into the fitting routine. In every iteration, called generation here, several sets of parameters, the DNAs, are used. Their "fitness", i.e. a measure for deviation from the measured data, is calculated and compared. The fittest create "children", i.e. two DNAs are mixed into a new one, to give a new set of DNAs for the next generation. DNAs who are not fit enough "die out" and are replaced by new random DNAs.

The included randomness ensures that for enough generations and a big enough population, i.e. number of DNAs in each generation, the area in which the global minimum lies can be found. Within this area standard fit routines can be used to find the local minimum in this area to actually get the global minimum.

2.5.5 Output of data

At different steps of the toolchain, different outputs are possible. After the time calibration, time spectra can be created. If the energy is calibrated and reference ranges are defined in addition, 2D spectra can be output from which also pseudo frequency spectra can be calculated [57, 114]. Finally, after the motion reconstruction, the full motion is given and can be used for further evaluation steps or setting experimental parameters accordingly.

Part I

Temporal phase interferometry

Chapter 3

Heterodyne phase reconstruction

Conventional light detectors, such as e.g. avalanche photo diodes (APDs), can only count photons [83]. Thus, there is no direct way to measure the phase of the complex electric field. However, some effects are only visible in the phase and Fourier transforms of the electric field are impossible if the phase relation is not measurable. This is known as the phase problem and is a difficulty not only at x-ray energies [84, 85]. Since the first attempt to overcome this problem by Gabor in 1948 [86], the key idea is to measure interference patterns from which the phase can be reconstructed. The common approach of spatial interferometers, such as the Mach-Zehnder-interferometer, is difficult to realize in the x-ray regime since the two path lengths have to be stabilized on sub-Ångstrom level.

In this chapter, we will focus on a method using a Mössbauer drive as an interferometer and phase retarder. First, a phase reconstruction method initially introduced by Callens et al. [78] will be explained in Section 3.1. The key idea is that the oscillation created by the interference between sample and analyzer has a phase directly related to the sample's phase. Afterwards, we move on to further improvement of the method developed in the scope of this thesis. We start with a closer look into the regions near the quantum beats in Section 3.2. In these regions, the interference oscillation goes to zero and thus does not give a proper phase relation anymore. Next, in Section 3.3 corrections terms neglected in the initial simplistic treatment by Callens et al. [78] are introduced to overcome the problems at quantum beats. In Section 3.4, the extended method is included in our standard data evaluation chain (see Fig. 2.10), which was already used at the beamtime in May 2021. Finally, Section 3.5 discusses the general usability of the developed heterodyne phase detection.

3.1 Simplistic heterodyne phase reconstruction scheme

There are different possibilities to access the phase problem, e.g. via 2D spectra [41, 65]. Here, the idea of Callens et al. [78] is presented. The principal setup is shown in Fig. 3.1. The sample, that is to be measured, and a single line absorber on a Mössbauer drive are placed in front of a a set of APDs. For the light input synchrotron radiation is used. As we will see in Eq. (3.5), the sample and analyzer on Mössbauer drive are commutative in the evaluated off-resonant regime. For

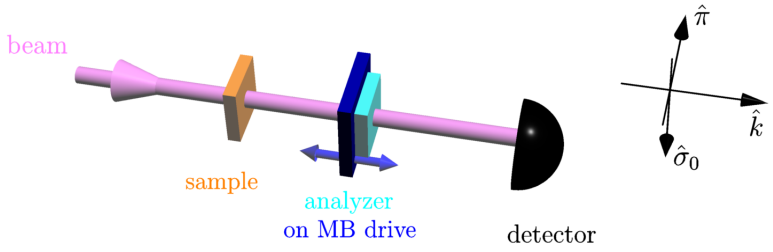

Figure 3.1: An analyzer (cyan) on a Mössbauer drive (blue) is placed downstream of the sample to be analyzed (orange). A detector, typically avalanche photo diodes (APDs), detects the forward scattered light after the interaction with synchrotron radiation. The Mössbauer drive velocity and arrival time of photons are recorded to create 2D spectra.

simplicity, we assume the transition frequency of the single line analyzer to be the same as the one of the sample ω_0, which can be realized in experiments for ^{57} by using a stainless steel foil as the analyzer.

The electric field behind the sample can be described by

$$\vec{E}_s(t) = |E_\sigma(t)|e^{i\phi_\sigma(t)}\vec{e}_\sigma + |E_\pi(t)|e^{i\phi_\pi(t)}\vec{e}_\pi, \tag{3.1}$$

where $\vec{e}_\sigma$ and $\vec{e}_\pi$ indicate two different polarization directions.

Moving the single line absorber with velocity v causes a Doppler shift of

$$\Delta_\mathrm{D} = \omega_0 \frac{v}{c}, \tag{3.2}$$

where ω_0 is the analyzer transition frequency, which is identical to the sample's transition frequency, and c is the speed of light. That causes an additional phase in the electric field scattered by the single line analyzer

$$E^\mathrm{D}_\mathrm{ana}(t) = e^{-i\Delta_\mathrm{D}t}E_\mathrm{ana}(t), \tag{3.3}$$

where $E_\mathrm{ana}(t)$ is the electric field after the analyzer sample without Mössbauer drive. The single line absorber has no polarization dependency. However, if the incoming beam has a polarization, the single line absorber preserves it. Let us assume that the incoming beam is polarized along the $\vec{e}_\sigma$. In that case, the electric field behind the analyzer mounted on the Mössbauer drive with polarization dependency is given by

$$\vec{E}^\mathrm{D}_\mathrm{ana}(t) = e^{-i\Delta t}E_\mathrm{ana}(t)\vec{e}_\sigma. \tag{3.4}$$

As we have seen in Section 2.2.3, in general calculating the combined time spectrum of two samples is difficult. The key idea of Callens et al. [78] is to only consider the regime outside of the sample's resonant frequency regime (see Fig. 2.3a). Far away from resonances, we can assume that there is no coupling between the sample and the analyzer. Hence, coupling terms between the two electric fields can be neglected and the two fields can simply be added up

$$\vec{E}_\mathrm{comb}(\Delta_\mathrm{D}, t) = \vec{E}^\mathrm{D}_\mathrm{ana}(t) + \vec{E}_\mathrm{s}(t). \tag{3.5}$$

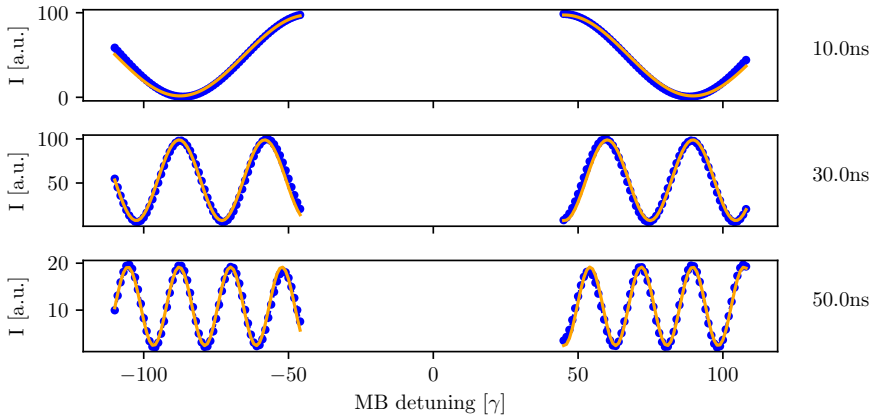

Figure 3.2: Simulated data intensities as function of Mössbauer detuning Δ_D (blue) and fits of fit function $f_{t_0}(\Delta_\mathrm{D})$ in Eq. (3.8) (orange) for different times t_0 (label at right). The oscillation is clearly visible and fit and data agree with each other. In the empty central region from -45γ to 45γ, the resonances are expected which is why this region is excluded from the fit and thus not shown. The resulting amplitude and phase of the complex field are shown in Fig. 3.3.

From this equation it can also be seen that the order of sample and analyzer does not matter. The measured intensity is given by

$$I(\Delta_\mathrm{D}, t) = |\vec{E}^\mathrm{D}_\mathrm{ana}(t) + E_\mathrm{s}(t)|^2 \tag{3.6}$$

$$= \underbrace{|E_\mathrm{ana}(t)|^2 + |\vec{E}_\mathrm{s}(t)|^2}_{\text{baseline}} + \underbrace{2|E_\mathrm{ana}(t)||E_\sigma(t)|}_{\text{amplitude}} \underbrace{\cos\left[\phi_\sigma(t) + \Delta_\mathrm{D} t\right]}_{\text{oscillation}}, \tag{3.7}$$

where we used $|E_\mathrm{ana}(t)| = |E^\mathrm{D}_\mathrm{ana}(t)|$ and $|\vec{E}_\mathrm{s}(t)| = |E_\mathrm{s}(t)|$. Note that the highly oscillating terms $e^{i\omega_0 t}$ in $E_\mathrm{ana}(t)$ and $E_\mathrm{s}(t)$ (see Eqs. (2.10) and (2.13)) cancel each other, such that this phase is not included in $\phi_\sigma(t)$. For a fixed time $t = t_0$, this equation is just an oscillation as function of Δ_D with amplitude $2|E_\mathrm{ana}(t_0)||E_\sigma(t_0)|$ and "oscillation frequency" t_0 on top of a baseline $|E_\mathrm{ana}(t_0)|^2 + |\vec{E}_\mathrm{s}(t_0)|^2$. Hence, for a given 2D spectrum, i.e. intensity as function of time t and Mössbauer detuning Δ_D, a function

$$f_{t_0}(\Delta_\mathrm{D}) = A + B\cos\left(C + \Delta_\mathrm{D} t_0\right) \tag{3.8}$$

can be fitted to slices at different times t_0. Throughout this thesis, those oscillation fits are performed with the Levenberg-Marquardt (least square) algorithm [130]. Examples of those fits are shown in Fig. 3.2 for a $1\,\mu$m thick sample with only the two linear lines driven. The oscillation due to the cosine term in Eq. (3.6) is clearly visible. In addition, the "oscillation frequency", which is equivalent to the time at which the data is taken, increases with time as expected. We can see that the fits of Eq. (3.8) (orange) resemble the measured data (blue) well. The slight "oscillation frequency" deviation for early times, i.e. at 10 ns, is not yet understood. Note that only a region of about -45γ to 45γ needs to be excluded from the analysis in case

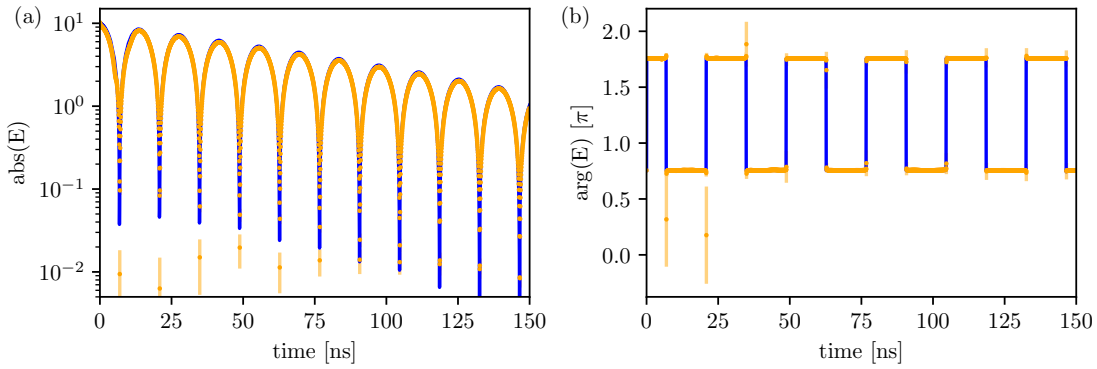

Figure 3.3: The reconstructed (orange dots) field amplitude (a) and phase (b) are compared to the calculated ones (blue line) for a 1 μm thick sample with only the two linear lines driven. Some corresponding fits of Eq. (3.8) can be found in Fig. 3.2. The errorbars indicate the standard deviations from the fitting routines.

of only the two linear lines being driven in contrast to the region of about -100γ to 100γ excluded by Callens et al. in [78].

With measuring the intensity of the analyzer $I_{\mathrm{ana}}(t_0)$, we can reconstruct the amplitude of the complete electric field of the sample $|E_{\mathrm{s}}(t_0)|$, its amplitude in beam polarization direction $|E_\sigma(t_0)|$ and the phase in beam polarization direction $\phi_\sigma(t_0)$ at time t_0 as follows

$$|E_{\mathrm{s}}(t_0)| = \sqrt{A/I_{\mathrm{ana}}(t_0)}, \tag{3.9}$$

$$|E_\sigma(t_0)| = B/\left(2\sqrt{I_{\mathrm{ana}}(t_0)}\right), \tag{3.10}$$

$$\phi_\sigma(t_0) = C. \tag{3.11}$$

Doing so for multiple times t_0 gives the corresponding measurands as function of time. All needed quantities for the value extraction in Eqs. (3.9) to (3.11) can in principle be measured. Only the rough frequency spectrum must be known to exclude near-resonance regimes. However, the spectrum can directly be extracted from the 2D histogram via late time integration [57, 114]. Hence, no model assumptions despite the no coupling approximation have to be made to extract amplitude and phase of the electric field behind the sample.

An example for a reconstructed complex field from simulated data is shown in Fig. 3.3. The reconstructed amplitude and phase agree with the calculated ones within the errors. Furthermore, errors are biggest at the quantum beat minima. The large errors are due to the quantum beat problem to be discussed in Section 3.2.

If the sample has no polarization dependency, the described method directly gives the amplitude and phase of the sample as a function of time. If there is a polarization dependence, for complete information the above steps have to be repeated for the other polarization direction by rotating the polarization of the incoming beam or usually more feasible in experiment by rotating the sample. However, depending on

the requirements, oftentimes it is enough to know only amplitude and phase of one polarization direction.

3.2 The quantum beat problem

We will now start with improvements, which were performed within the scope of this thesis, of the heterodyne phase reconstruction (HPR) scheme by Callens et al. [78] resulting in an extended heterodyne phase reconstruction (xHPR) scheme (see Section 3.3). As a first step, the behaviour close to quantum beat minima is analyzed because the neglected coupling terms have the strongest effect at low intensities.

HPR relies on the oscillations from the interference term (see Eq. (3.6)). However, close to quantum beats, this oscillation approaches zero as the cosine terms in Eq. (2.13) causes the field amplitude $E_\mathrm{s}(t)$ to become minimal. Therefore, especially at those times, the formerly neglected coupling terms needs to be taken into account because they are not dominated anymore by the oscillation.

Using a δ-pulse as input field (see Eq. (2.4)), the combined electric field behind the two samples is given by

$$E_\mathrm{comb}(t) = R_\mathrm{comb}(t) * \delta(t) = R_\mathrm{comb}(t), \tag{3.12}$$

where

$$\begin{aligned} R_\mathrm{comb}(t) =& R_\mathrm{ana}(t) * R_\mathrm{s}(t) && (3.13)\\ =& \delta(t) - R^S_\mathrm{ana}(t) - R^S_\mathrm{s}(t) + R^S_\mathrm{ana}(t) * R^S_\mathrm{s}(t), && (3.14) \end{aligned}$$

is the combined response function of the two samples (see Eq. (2.21)) with the response functions of the single foils defined in Eq. (2.11) as

$$\begin{aligned} R_\mathrm{ana}(t) =& \delta(t) - R^S_\mathrm{ana}(t), && (3.15)\\ R_\mathrm{s}(t) =& \delta(t) - R^S_\mathrm{s}(t). && (3.16) \end{aligned}$$

For times $t > 0$ the $\delta(t)$-functions vanish and we can simply write

$$R_\mathrm{comb}(t) = R_\mathrm{ana}(t) + R_\mathrm{s}(t) + R^S_\mathrm{ana}(t) * R^S_\mathrm{s}(t). \tag{3.17}$$

Thus, the combined spectrum is calculated to be

$$\begin{aligned} I_{\mathrm{comb}}(t) =& |E_{\mathrm{comb}}(t)|^2 \\ =& |R_{\mathrm{ana}}(t) + R_{\mathrm{s}}(t)|^2 + |R^S_{\mathrm{ana}}(t) * R^S_{\mathrm{s}}(t)|^2 \\ &+ 2\Re\big\{[R_{\mathrm{ana}}(t) + R_{\mathrm{s}}(t)] \cdot \big[R^S_{\mathrm{ana}}(t) * R^S_{\mathrm{s}}(t)\big]\big\} \\ =& \underbrace{\underbrace{|R_{\mathrm{ana}}(t)|^2 + |R_{\mathrm{s}}(t)|^2}_{\text{background}} + \underbrace{|R_{\mathrm{ana}}(t)| \cdot |R_{\mathrm{s}}(t)| \cos[\phi(t) + \Delta_D t]}_{\text{oscillation}}}_{\text{Callens et al.}} \\ &+ \underbrace{\underbrace{|\,R^S_{\mathrm{ana}}(t) * R^S_{\mathrm{s}}(t)\,|^2}_{\text{interference}} + \underbrace{2\Re\big\{[R_{\mathrm{ana}}(t) + R_{\mathrm{s}}(t)]^* \cdot \big[R^S_{\mathrm{ana}}(t) * R^S_{\mathrm{s}}(t)\big]\big\}}_{\text{mixture with interference term}}}_{\text{correction terms}}. \end{aligned} \tag{3.18}$$

The first terms are the well-known terms of HPR in Eq. (3.6) by Callens et al. [78]. The second terms are corrections, that will partially be included into the fit model in Section 3.3.

The correction terms become most important close to the quantum beats because there, the oscillation that is used by Callens et al. [78] to extract complex phase information becomes zero. The effect is most prominent if only the two linear transitions are driven ($\alpha = \pi/2$) because there is only one cosine term in Eq. (2.13), such that at every intensity minimum the oscillation reaches zero. For all six lines driven only at common multiples of the hyperfine splitting detunings ($\Delta_{\mathrm{hyp},1} = 53.6\gamma$, $\Delta_{\mathrm{hyp},2} = 31.1\gamma$ and $\Delta_{\mathrm{hyp},3} = 8.6\gamma$) the minima get close to zero.

Furthermore, in experiments the limited counting statistics due to limited measurement times increases the effect in comparison to simulation data. An example for low visibility of the oscillation in experimental data can be found in Fig. 4.4b.

3.3 Extended heterodyne phase detection

We now want to evaluate the correction terms in Eq. (3.18) and partially include them into the simple fit model in Eq. (3.8) for extended heterodyne phase reconstruction (xHPR). Furthermore, we will see that the inclusion of correction terms in the fit model allows us to also include the region between the resonances (see Fig. 3.4), which increases the used data from one measurement and thus gives better statistics.

In principle, for better statistics the detuning range could just be chosen as big as possible. However, in experiments a bigger range would limit the frequency resolution in most cases. A reduced frequency resolution is not wanted for two reasons. First, the "oscillation frequency" increases with time (see Fig. 3.2). Thus for later times, a limited frequency resolution would be problematic. In experiments (see [41, 65]), we have a frequency resolution of about 0.5γ in the 2D spectra, so that at $t = 141\,\mathrm{ns}$, i.e. at t equal to the lifetime, there are only about two data points per oscillation period, which makes the fitting already hard. Second, usually

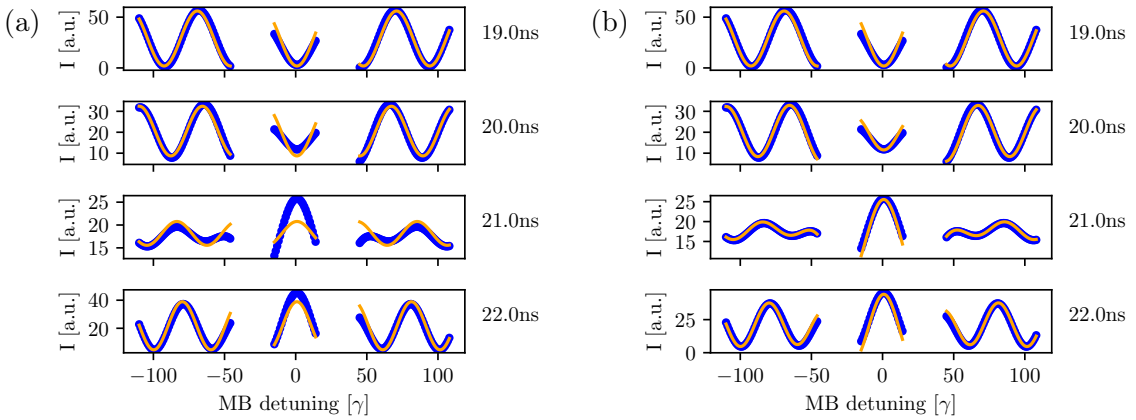

Figure 3.4: Example oscillation fits without (HPR) in (a) and with (xHPR) in (b) the extension presented in Eq. (3.45). Especially in the center, the extended model fit performs much better. Near 21 ns there is a quantum beat minimum, so that the extension in xHPR becomes most important here out of all shown times. Regions around resonances between -45γ and -15γ as well as 15γ and 45γ are excluded from the fits.

the spectra are not only measured for phase reconstruction. Other analyses such as late time integration for frequency spectra [57, 114] would suffer from a limited frequency resolution.

Thus, increasing the detuning range by using larger detunings is limited, but we could try to additionally use detuning ranges within the spectral region. Naively, one could imagine that it is sufficient that the used Mössbauer detuning range is far away from the resonances to not have coupling effects, but that the analyzed detuning range can even lie in between resonances. However, as shown in Fig. 3.4a especially close to quantum beats the combined field of sample and analyzer cannot simply be calculated as the sum of the individual fields if including regions between the resonances. The amplitude of the oscillation in the center differs significantly from the one in the off-resonant regime. The effect is strongest close to quantum beats, e.g. at 21 ns. The reason for the deviations is that the oscillation term approaches zero so that it does not dominate over the formerly neglected coupling terms any more (see Section 3.2). In Fig. 3.4a, in contrast to the other times, at 21 ns the fitted oscillation is clearly dominated by another structure that will be discussed in more detail in this section. The further from the quantum beat the more dominant the oscillation is over the additional structure so that neglecting coupling terms becomes valid again.

For thin foils, it is possible to extend the approach by Callens et al. in [78] to detunings within the region of the frequency spectrum, but far away from any resonant line by the inclusion of correction terms. Especially, if only the two linear lines are driven, an additional region of -15γ to 15γ (see Fig. 3.4b) can be used for the analysis.

3.3.1 Evaluating the interference term convolution

In all correction terms in Eq. (3.18), the interference term $R^S_{\text{ana}}(t) * R^S_{\text{sample}}(t)$ occurs. In a first step, we will evaluate this convolution.

To simplify the expressions, we assume only two lines to be driven with a detuning of $\pm\Delta_{\text{hyp}}$. Because the contributions from different pairs of driven lines are additive, the result for only linear lines driven can simply be extended to all lines being driven. The responses of sample and analyzer are given by Eqs. (2.10) and (2.13)

$$R^S_s(t) = \sqrt{\frac{b_\text{s}}{t}} J_1\left(2\sqrt{b_\text{s} t}\right) e^{-i\omega_r t} e^{-\gamma_\text{s} t/2} \left[e^{-i\Delta_{hyp} t} + e^{i\Delta_{hyp} t}\right] \tag{3.19}$$

$$= R^{\text{no hyp}}_\text{s}(t) 2\cos\left(\Delta_\text{hyp} t\right), \tag{3.20}$$

$$R^S_{\text{ana}}(t) = \sqrt{\frac{b_\text{ana}}{t}} J_1\left(2\sqrt{b_\text{ana} t}\right) e^{-i\omega_r t} e^{-\gamma_\text{ana} t/2}, \tag{3.21}$$

such that the interference term is given by

$$R^S_{\text{ana}}(t) * R^S_s(t) = e^{-i\omega_r t} e^{-\gamma_s t/2} \int_0^\infty \sqrt{\frac{b_\text{ana}}{\tau}} J_1\left(2\sqrt{b_\text{ana}\tau}\right) e^{-(\gamma_\text{ana}-\gamma_s)\tau/2} e^{-i\Delta_\text{D}\tau} \sqrt{\frac{b_\text{s}}{t-\tau}} J_1\left(2\sqrt{b_\text{s}(t-\tau)}\right) 2\cos\left[\Delta_{hyp}(t-\tau)\right] \mathrm{d}\tau. \tag{3.22}$$

Thin target approximation. For thin samples or short times the Bessel functions of first kind J_1 can be Taylor expanded and approximated (see Eq. (2.17))

$$\sqrt{\frac{b}{t}} J_1\left(2\sqrt{bt}\right) \approx b e^{-bt/2}. \tag{3.23}$$

Inserting this approximation into Eq. (3.22) we find

$$R^S_{\text{ana}}(t) * R^S_s(t) = 2e^{-i\omega_r t} e^{-(\gamma_s + b_s)t/2} b_{ana} b_s \int_0^\infty e^{-(\gamma_\text{ana}-\gamma_s+b_\text{ana}-b_s)\tau/2} e^{-i\Delta_\text{D}\tau} \cos\left[\Delta_\text{hyp}(t-\tau)\right] \mathrm{d}\tau. \tag{3.24}$$

The validity range of this approximation gives a natural reconstruction time limit in case of xHPR.

Quantum beat approximation. In Fig. 3.4, it can be seen that the correction becomes most important around the quantum beats, e.g. at 21 ns, while being less important in between. Close to quantum beats, we can approximate

$$\cos\left(\Delta_\text{hyp} t\right) \approx 0 \Leftrightarrow \Delta_\text{hyp} t \approx \pm\pi/2 + n \cdot 2\pi, \quad n \in \mathbb{Z}. \tag{3.25}$$

The sign is given by $\text{sign}\left[\sin\left(\Delta_\text{hyp} t\right)\right]$. With this approximation, it is

$$\cos\left(\Delta_\text{hyp}(t-\tau)\right) \approx \sin\left(\Delta_\text{hyp}\tau\right) \tag{3.26}$$

and we find

$$R^S_{\text{ana}}(t) * R^S_s(t) = \pm e^{-i\omega_r t} e^{-(\gamma_s + b_s)t/2} b_{\text{ana}} b_s \int_0^\infty e^{-(\gamma_{\text{ana}} - \gamma_s + b_{\text{ana}} - b_s)\tau/2} e^{-i\Delta_{\text{D}}\tau} 2\sin(\Delta_{\text{hyp}}\tau)\mathrm{d}\tau. \quad (3.27)$$

Before we start to evaluate this integral, we introduce an effective line width

$$\gamma_{\text{eff}} = \frac{1}{2}\left[\gamma_{\text{ana}} - \gamma_{\text{s}} + (b_{\text{ana}} - b_{\text{s}})\right]. \quad (3.28)$$

The integral can simply be calculated to be

$$2\int_0^t e^{-(\gamma_{\text{eff}} + i\Delta_{\text{D}})\tau} \sin(\omega_{\text{hyp}} t)\,\mathrm{d}\tau = -i\frac{e^{-\left(\gamma_{\text{eff}} + i\Delta + i\omega_{\text{hyp}}\right)t} - 1}{\gamma_{\text{eff}} + i(\Delta + \Delta_{\text{hyp}})} + i\frac{e^{-\left(\gamma_{\text{eff}} + i\Delta - i\Delta_{\text{hyp}}\right)t} - 1}{\gamma_{\text{eff}} + i(\Delta - \Delta_{\text{hyp}})}. \quad (3.29)$$

With the quantum beat approximation $\Delta_{\text{hyp}} t \approx \pm\pi/2 + n \cdot 2\pi$ in Eq. (3.25), this expression simplifies to

$$\begin{aligned} &-i\frac{e^{-\left(\gamma_{\text{eff}} + i\Delta_{\text{D}} + i\Delta_{\text{hyp}}\right)t} - 1}{\gamma_{\text{eff}} + i(\Delta_{\text{D}} + \Delta_{\text{hyp}})} + i\frac{e^{-\left(\gamma_{\text{eff}} + i\Delta - i\Delta_{\text{hyp}}\right)t} - 1}{\gamma_{\text{eff}} + i(\Delta_{\text{D}} - \Delta_{\text{hyp}})} \\ &\qquad = -\frac{\pm e^{-(\gamma_{\text{eff}} + i\Delta_{\text{D}})t} - i}{\gamma_{\text{eff}} + i(\Delta_{\text{D}} + \Delta_{\text{hyp}})} + \frac{\mp e^{-(\gamma_{\text{eff}} + i\Delta_{\text{D}})t} - i}{\gamma_{\text{eff}} + i(\Delta_{\text{D}} - \Delta_{\text{hyp}})}. \end{aligned} \quad (3.30)$$

Plugging this result back into Eq. (3.27) it is

$$\begin{aligned} R_{\text{ana}}(t) * R_{\text{s}}(t) &= \pm\, e^{-(i\omega_r + \gamma_s)t} b_{\text{ana}} b_{\text{s}} \left(\frac{-e^{-(\gamma_{\text{eff}} + i\Delta_{\text{D}})t} \pm i}{\gamma_{\text{eff}} + i(\Delta + \Delta_{\text{hyp}})} + \frac{-e^{-(\gamma_{\text{eff}} + i\Delta_{\text{D}} -)t} \mp i}{\gamma_{\text{eff}} + i(\Delta - \Delta_{\text{hyp}})} \right) \\ &= \frac{-R^S_{\text{ana}}(t) \pm i R^{\text{no hyp}}_{\text{s}}(t)}{\gamma_{\text{eff}} + i\,(\Delta_{\text{D}} + \Delta_{\text{hyp}})} + \frac{-R^S_{\text{ana}}(t) \mp i R^{\text{no hyp}}_{\text{s}}(t)}{\gamma_{\text{eff}} + i\,(\Delta_{\text{D}} - \Delta_{\text{hyp}})}. \end{aligned} \quad (3.31)$$

Thus, we get two similar terms only varying in the relative sign between $R^{\text{no hyp}}_s(t)$ and $R^S_{\text{ana}}(t)$ centered around Doppler detunings of $\Delta_D = \pm\Delta_{\text{hyp}}$, respectively.

Off-resonance approximation. To simplify even further, we have a closer look onto γ_{eff}. Typical values are $\gamma_{\text{ana}} - \gamma_{\text{s}} < \gamma_{\text{s}}$ and $b_{\text{ana}} - b_{\text{s}} < \gamma_{\text{s}}$. Hence, γ_{eff} is on the order of a few γ_{s}. Off the resonances, i.e. $|\Delta_{\text{D}} \pm \omega_{\text{hyp}}| \gg \gamma_s$, we can approximate

$$\gamma_{\text{eff}} \ll |\Delta_{\text{D}} \pm \omega_{\text{hyp}}| \quad (3.32)$$

and neglect γ_{eff}. This approximation simplifies Eq. (3.31) to be

$$R^S_{\text{ana}}(t) * R^S_{\text{s}}(t) = \frac{\pm R^{\text{no hyp}}_{\text{s}}(t) + i R^S_{\text{ana}}(t)}{\Delta_{\text{D}} + \Delta_{\text{hyp}}} + \frac{\mp R^{\text{no hyp}}_{\text{s}}(t) + i R^S_{\text{ana}}(t)}{\Delta_{\text{D}} - \Delta_{\text{hyp}}}. \quad (3.33)$$

For negative Mössbauer detunings Δ_{D}, the left term dominates and vice versa. The nominators only differ in the sign of the response function of the sample without hyperfine splitting. All detuning frequency dependency is in the denominator.

Several lines. If more pairs of lines should be taken into account, we can use the additivity of different hyperfine splitting lines (see Eq. (2.13)). For j pairs of driven lines, the sample response in Eq. (3.20) is given by

$$R_{\mathrm{s}}^{S}(t) = R_{\mathrm{s}}^{\text{no hyp}} \sum_{j} \cos\left(\Delta_{\mathrm{hyp},j} t\right) \tag{3.34}$$

and hence the interference term in Eq. (3.33) becomes

$$R_{\mathrm{ana}}^{S}(t) * R_{\mathrm{s}}^{S}(t) = \sum_{j} \frac{\pm R_{\mathrm{s}}^{\text{no hyp}}(t) + i R_{\mathrm{ana}}^{S}(t)}{\Delta_{\mathrm{D}} + \Delta_{\mathrm{hyp},j}} + \frac{\mp R_{\mathrm{s}}^{\text{no hyp}}(t) + i R_{\mathrm{ana}}^{S}(t)}{\Delta_{\mathrm{D}} - \Delta_{\mathrm{hyp},j}}, \tag{3.35}$$

where we used the distributivity of convolutions.

However, as we have to be far enough away from the resonances, this extension is most valuable for only the linear lines being driven. Hence, we will continue with this simpler situation.

3.3.2 Calculating the different correction terms

After calculating the interference term in Eq. (3.33), we can now go back to Eq. (3.18) and calculate the two different correction terms.

First correction term. The first one is given by

$$\begin{aligned}
\left|R_{\mathrm{ana}}^{S}(t) * R_{\mathrm{s}}^{S}(t)\right|^2 =& \left| \frac{\pm R_{\mathrm{s}}^{\text{no hyp}}(t) + i R_{\mathrm{ana}}^{S}(t)}{\Delta_{\mathrm{D}} + \Delta_{\mathrm{hyp}}} + \frac{\mp R_{\mathrm{s}}^{\text{no hyp}}(t) + i R_{\mathrm{ana}}^{S}(t)}{\Delta_{\mathrm{D}} - \Delta_{\mathrm{hyp}}} \right|^2 \\
=& \frac{|\pm R_{\mathrm{s}}^{\text{no hyp}}(t) + i R_{\mathrm{ana}}^{S}(t)|^2}{\left(\Delta_{\mathrm{MB}} + \Delta_{\mathrm{hyp}}\right)^2} + \frac{|\mp R_{\mathrm{s}}^{\text{no hyp}}(t) + i R_{\mathrm{ana}}^{S}(t)|^2}{\left(\Delta_{\mathrm{MB}} - \Delta_{\mathrm{hyp}}\right)^2} \\
&+ \frac{2\Re\left\{\left[\pm R_{\mathrm{s}}^{\text{no hyp}}(t) + i R_{\mathrm{ana}}^{S}(t)\right]\left[\mp R_{\mathrm{s}}^{\text{no hyp}}(t) + i R_{\mathrm{ana}}^{S}(t)\right]^*\right\}}{\Delta_{\mathrm{MB}}^2 - \Delta_{\mathrm{hyp}}^2}.
\end{aligned} \tag{3.36}$$

The numerators in the first two terms are given by

$$\begin{aligned}
\left|\pm R_{\mathrm{s}}^{\text{no hyp}}(t) + i R_{\mathrm{ana}}(t)\right|^2 =& \left|R_{\mathrm{s}}^{\text{no hyp}}(t)\right|^2 + |R_{\mathrm{ana}}(t)|^2 \\
&\pm 2|R_{\mathrm{s}}(t)||R_{\mathrm{ana}}(t)| \sin\left(\phi_{\mathrm{s}}^{\text{no hyp}} - \phi_{\mathrm{ana}}\right),
\end{aligned} \tag{3.37}$$

where we used used

$$\begin{aligned}
|\pm a + ib|^2 =& \left(\pm\Re(a) - \Im(b)\right)^2 + \left(\pm\Im(a) + \Re(b)\right)^2 \\
=& |a|^2 + |b|^2 \pm 2|a||b| \sin(\phi_b - \phi_a)
\end{aligned} \tag{3.38}$$

for arbitrary $a, b \in \mathbb{C}$. The numerator of the second term is given by

$$2\Re\left\{\left[\pm R_{\mathrm{s}}^{\text{no hyp}}(t) + i R_{\mathrm{ana}}^{S}(t)\right]\left[\mp R_{\mathrm{s}}^{\text{no hyp}}(t) + i R_{\mathrm{ana}}^{S}(t)\right]^*\right\} = 2|R_{\mathrm{ana}}^{S}(t)|^2 - 2|R_{\mathrm{s}}^{\text{no hyp}}(t)|^2, \tag{3.39}$$

where we used

$$\Re\left[(\pm a + ib)\,(\mp a + ib)^*\right] = |b|^2 - |a|^2 \tag{3.40}$$

for arbitrary $a, b \in \mathbb{C}$. Hence, the first correction term in Eq. (3.36) can be simplified to be

$$\begin{aligned}\left|R^S_{\text{ana}}(t) * R^S_{\text{s}}(t)\right|^2 =& |R^{\text{no hyp}}_{\text{s}}(t)|^2 \left[\frac{1}{(\Delta_{\text{D}} + \Delta_{\text{hyp}})^2} + \frac{1}{(\Delta_{\text{D}} - \Delta_{\text{hyp}})^2} + \frac{2}{\Delta_{\text{D}}^2 + \Delta_{\text{hyp}}^2}\right] \\ &+ |R^S_{\text{ana}}(t)|^2 \left[\frac{1}{(\Delta_{\text{D}} + \Delta_{\text{hyp}})^2} + \frac{1}{(\Delta_{\text{D}} - \Delta_{\text{hyp}})^2} - \frac{2}{\Delta_{\text{D}}^2 + \Delta_{\text{hyp}}^2}\right] \\ &\pm 2|R^{(}_{\text{s}}t)||R_{\text{ana}}(t)| \sin\left(\phi^{\text{no hyp}}_{\text{s}} - \phi_{\text{ana}}\right) \\ &\cdot \left[\frac{1}{(\Delta_{\text{D}} + \Delta_{\text{hyp}})^2} + \frac{1}{(\Delta_{\text{D}} - \Delta_{\text{hyp}})^2}\right].\end{aligned} \tag{3.41}$$

This expression looks similar to the original model in Eq. (3.8), but with a frequency dependency on the Mössbauer detuning Δ_{D}.

Second correction term. The second term in Eq. (3.18) can be calculated to be

$$\begin{aligned}&2\Re\left[(R_{\text{ana}}(t) + R_s(t))^* \cdot \left(R^S_{\text{ana}}(t) * R^S_s(t)\right)\right] \\ &\quad\approx \Re\left[R^S_{\text{ana}}(t)^* \cdot \left(R^S_{\text{ana}}(t) * R^S_s(t)\right)\right] \\ &\quad\overset{(3.33)}{=} \Re\left[R^S_{\text{ana}}(t)^* \left(\frac{\pm R^{\text{no hyp}}_{\text{s}}(t) + iR^S_{\text{ana}}(t)}{\Delta_{\text{D}} + \Delta_{\text{hyp}}} + \frac{\mp R^{\text{no hyp}}_{\text{s}}(t) + iR^S_{\text{ana}}(t)}{\Delta_{\text{D}} - \Delta_{\text{hyp}}}\right)\right] \\ &\quad= \pm\Re\left[R^S_{\text{ana}}(t)^* R^{\text{no hyp}}_{\text{s}}(t)\right]\left(\frac{1}{\Delta_{\text{D}} + \Delta_{\text{hyp}}} - \frac{1}{\Delta_{\text{D}} - \Delta_{\text{hyp}}}\right) \\ &\quad\pm |R^S_{\text{ana}}(t)||R^{\text{no hyp}}_{\text{s}}(t)| \cos(\phi_{\text{ana}} - \phi_{\text{s}})\left(\frac{1}{\Delta_{\text{D}} + \Delta_{\text{hyp}}} - \frac{1}{\Delta_{\text{D}} - \Delta_{\text{hyp}}}\right),\end{aligned} \tag{3.42}$$

where in the second line we used that close to the quantum beats it is $R_{\text{s}}(t) \approx 0$, in the second last line $\Re\left(i|a|^2\right) = 0$ for arbitrary $a \in \mathbb{C}$ and in the last line

$$\Re\left(a^* b\right) = \Re(a)\Re(b) + \Im(a)\Im(b) = |a||b| \cos(\phi_a - \phi_b) \tag{3.43}$$

for arbitrary $a, b \in \mathbb{C}$.

3.3.3 The extended fit model

After the evaluation of the two correction terms, in Eqs. (3.41) and (3.42), the full model in Eq. (3.18), simplifies to

$$
\begin{aligned}
I_{\mathrm{comb}}(\Delta_{\mathrm{D}}, t) = |R_{\mathrm{ana}}(t)|^2 & \left[\underbrace{1}_{\text{Callens}} + \underbrace{\frac{1}{(\Delta_{\mathrm{D}} + \Delta_{\mathrm{hyp}})^2} + \frac{1}{(\Delta_{\mathrm{D}} - \Delta_{\mathrm{hyp}})^2} - \frac{2}{\Delta_{\mathrm{D}}^2 + \Delta_{\mathrm{hyp}}^2}}_{\text{2nd order correction}} \right] \\
& + |R_{\mathrm{s}}^{\text{no hyp}}(t)|^2 \left[\underbrace{\cos(\Delta_{\mathrm{hyp}} t)^2}_{\text{Callens}} + \underbrace{\frac{1}{(\Delta_{\mathrm{D}} + \Delta_{\mathrm{hyp}})^2} + \frac{1}{(\Delta_{\mathrm{D}} - \Delta_{\mathrm{hyp}})^2} + \frac{2}{\Delta_{\mathrm{D}}^2 + \Delta_{\mathrm{hyp}}^2}}_{\text{2nd order correction}} \right] \\
& \pm |R_{\mathrm{ana}}^{S}(t)||R_{\mathrm{s}}^{\text{no hyp}}(t)| \cos(\phi_{\mathrm{ana}} - \phi_{\mathrm{s}}) \left[\underbrace{2\cos(\Delta_{\mathrm{hyp}} t)}_{\text{Callens}} \pm \underbrace{\frac{1}{\Delta_{\mathrm{D}} - \Delta_{\mathrm{hyp}}} - \frac{1}{\Delta_{\mathrm{D}} + \Delta_{\mathrm{hyp}}}}_{\text{1st order correction}} \right] \\
& \pm 2|R_{\mathrm{s}}^{(}t)||R_{\mathrm{ana}}(t)| \sin\left(\phi_{\mathrm{s}}^{\text{no hyp}} - \phi_{\mathrm{ana}}\right) \left[\underbrace{\frac{1}{(\Delta_{\mathrm{D}} + \Delta_{\mathrm{hyp}})^2} + \frac{1}{(\Delta_{\mathrm{D}} - \Delta_{\mathrm{hyp}})^2}}_{\text{2nd order correction}} \right] .
\end{aligned}
\tag{3.44}
$$

The sign of the correction terms can be determined by sign $[\sin(\Delta_{\mathrm{hyp}} t)]$. In addition to the simple model by Callens et al. [78]. (HPR), we get several correction terms if including coupling terms close to quantum beats but still off resonances. Most correction terms are of 2nd order. In a first extension of the fit model, we will only consider 1st order extensions. Thus, the extended fit model is given by

$$
f_{t_0}^{\mathrm{ext}}(t) = A + B\cos\left[C + \Delta_{\mathrm{D}} t_0\right] \cdot \left[2\cos(\Delta_{\mathrm{hyp}} t) \underbrace{+ D\left(\frac{1}{\Delta_{\mathrm{D}} + \Delta_{\mathrm{hyp}}} - \frac{1}{\Delta_{\mathrm{D}} - \Delta_{\mathrm{hyp}}} \right)}_{\text{extension}} \right] ,
\tag{3.45}
$$

where the sign of the 1st order correction term is included into the additional fit parameter D. That is introduced to take into account that the correction is most dominant close to quantum beats and can be set to zero far away from quantum beat minima. In addition, D depends on the interference and coupling between sample and analyzer, which can be distorted by noise. This given model is still a rather simple fit model called xHPR. As with the fit function in Eq. (3.8) the interesting properties can be extracted by Eqs. (3.9) to (3.11) despite the fact, that Eq. (3.10) gives the amplitude without hyperfine splitting because the hyperfine splitting is

added into the fit function $f_{t_0}^{\text{ext}}(t)$ by $2\cos(\Delta_{\text{hyp}}t)$. A comparison of the oscillation fits with and without the correction term in the extended regime is shown in Fig. 3.4. It can clearly be seen that for low oscillation amplitudes, i.e. at the minima of the quantum beats around 21 ns, and in the center of the Mössbauer detuning range the correction becomes most important. Even though the fit model only takes correction terms up to first order into account to keep the model simple, it resembles the data reasonably well.

The fit model of xHPR could be extended even further by taking into account the second order correction terms as well. However, that would complicate the fit model much more than the first order corrections terms. Because already xHPR gives much better results than HPR and we did not find regimes, where second order terms would be necessary, we decided to stay with the simpler first order extension and leave the inclusion of second order correction terms as an open project.

3.4 Usage in data evaluation

The usage of xHPR and HPR in the toolchain for data analysis is shown in Fig. 3.5. A detailed explanation of the new features is given in this section. During our beamtime in May 2021, the extended toolchain has successfully been used.

3.4.1 Complex field amplitudes

Benefits. HPR and its extension xHPR can reconstruct the phase of the complex field behind a sample from a 2D spectrum. In combination with the intensity, complex field amplitudes of light scattered from a sample in forward direction can be extracted.

Thus after the creation of 2D spectra, besides 2D spectra itself and frequency spectra calculated via late time integration, with the extended toolchain complex field amplitudes are accessible. A reconstructed example complex field is compared to the one calculated with `pynuss` from material properties in Fig. 3.6. At all times, the calculated and reconstructed results agree within the errorbars. Large errorbars can be found for late times and at quantum beat minima due to limited statistics and Mössbauer detuning resolution.

If the input electric field is known and simple enough so that a deconvolution is possible, e.g. short synchrotron pulses represented by δ-functions, the complex scattering field directly gives access to the sample's complex response function.

In addition, it enables the reconstruction of the whole class of phase-related observables, e.g. small motions in Chapter 4.

Implementation. The implementation of using xHPR in the data evaluation is summarized in Algorithm 1.

First, the resonances need to be cut out from the 2D spectrum so that they are not used in the fitting routines. For only linear lines driven the regions of $[-45\gamma, -15\gamma]$,

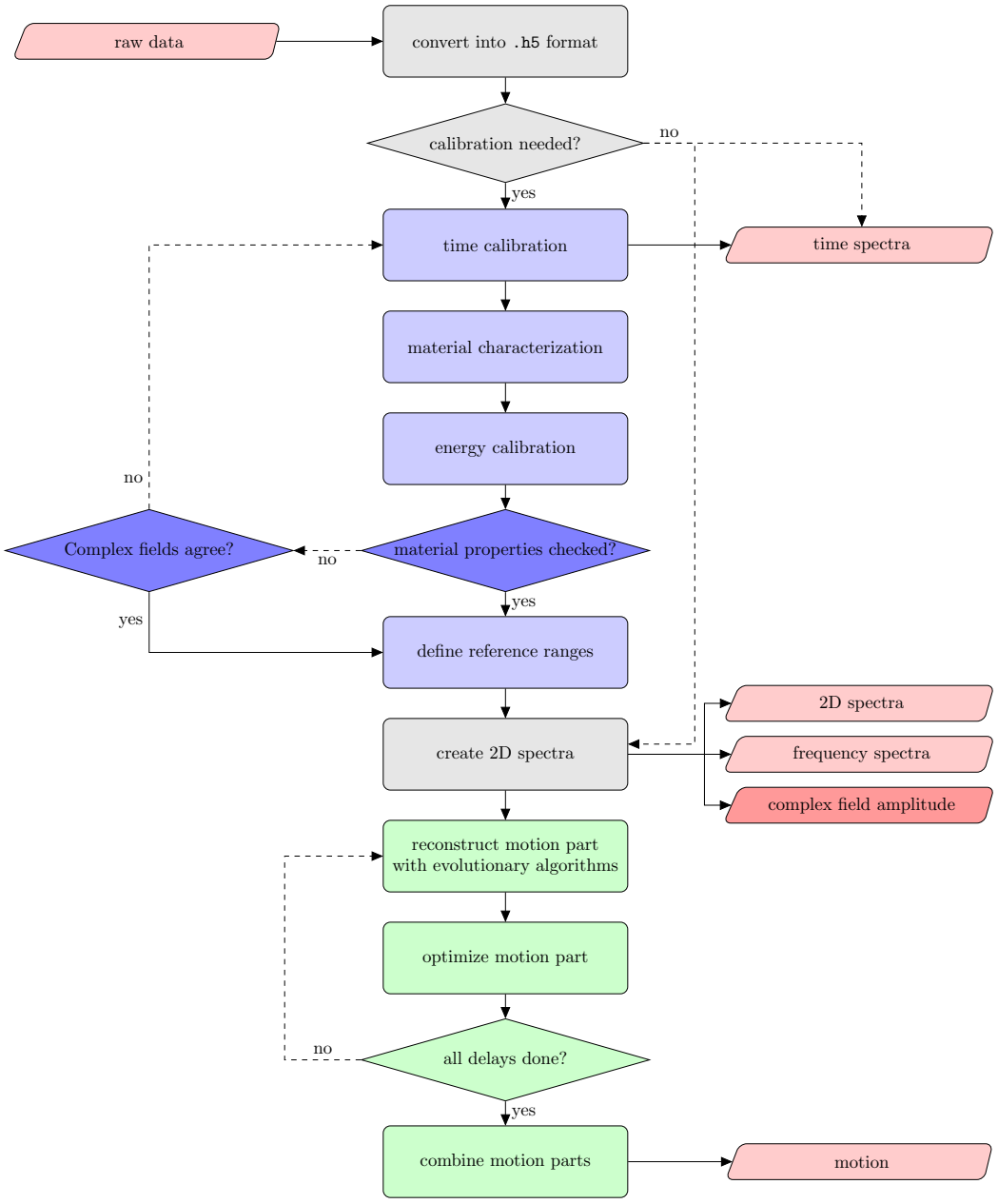

Figure 3.5: The light colors correspond to the standard tool chain as shown in Fig. 2.10, the strong colors to the newly inserted blocks. From the 2D spectra with use of xHPR, also the complex electric field amplitude can be reconstructed. The complex field amplitudes provide a crosscheck for the material characterizations if the amplitude and phase calculated with `pynuss` from material properties and ones reconstructed from 2D with the scheme presented in this chapter agree.

```
1  Function FitFunction(I, Delta, IRef, t):
       Input: I: intensities at t as function of Mössbauer detuning
              Delta: Mössbauer detuning
              IRef: Intensity of analyzer at t
              t: time
       Result: EAbs: amplitude of electric field at t
               EPhi: phase of electric field at t
2      fitFunction_HPR = A + B*cos(C + Delta t)
3      fitFunction_xHPR = A + B*cos(C + Delta t)*(2*cos(DeltaHyp t) +
        D*( 1/(Delta + DeltaHyp) - 1/(Delta - DeltaHyp) ) )
4      AOpti, COpti = fit fitFunction to I
5      EAbs = AOpti / (2*sqrt(IRef))
6      EPhi = COpti
7      return EAbs, phiOpti
8  Function ExtractComplexField(2Dspec, refSpec, tCutOff, resonances):
       Input: 2Dspec: 2D spectrum of combined response
              refSpec: time spectrum of analyzer only
              tCutOff: time until which complex field is extracted
              resonances: list of the resonant ranges that are to be excluded
       Result: E: complex electric field as function of time
9      cut out resonances from 2Dspectrum
10     A = []
11     phi = []
12     for t=1 to t=tCutOff do
13         I, Δ = slice of 2Dspectrum at t
14         A_t, phi_t= FitFunction (I, Δ, refI, t)
15         A.append(A_t)
16         phi.append(phi_t)
17     E = A*exp(i*phi)
18     return E
```

Algorithm 1: Pseudo code algorithm of usage of HPR and xHPR in data evaluation to extract complex fields. It can be performed after the creation of 2D spectra in the toolchain (see Fig. 3.5). The fit function has to be chosen according to the used scheme. Only the σ-component of the electric field is considered, because the intensity of the complete field is usually measured in time spectra already.

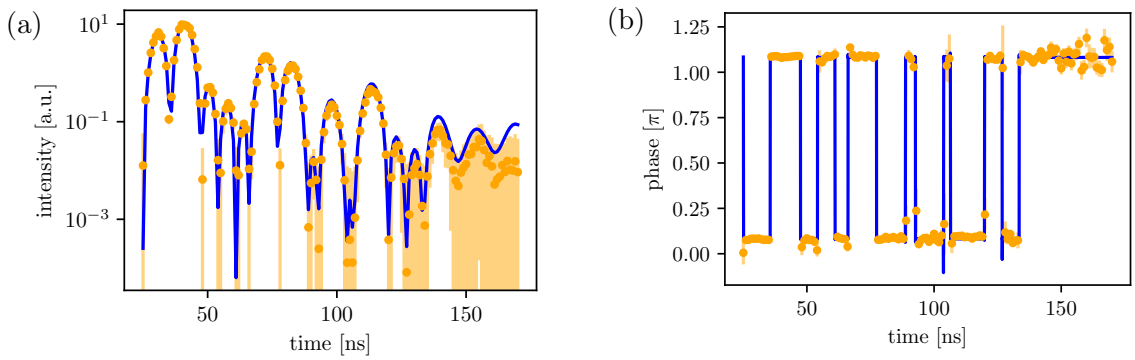

Figure 3.6: The reconstructed (orange dots) field amplitude (a) and phase (b) are compared to the calculated ones (blue line). In this example, all six lines are driven so that the resonant regime between -65γ and 65γ is excluded from the fits and HPR is used. A cutoff time of 170 ns is set to also show some noisy data at late times. Results for later times and at the quantum beat minima are noisy due to lower counting statistics. The calculated values are interpolated and evaluated at the measured times. Standard deviations from fitting routines are indicated by errorbars.

$[15\gamma, 45\gamma]$ (xHPR) and $[-45\gamma, 45\gamma]$ (HPR) need to be excluded. In the case of all six lines driven, the outer most resonances lie at $\pm 53.6\gamma$ so that a region of $[-65\gamma, 65\gamma]$ needs to be cut out before the analysis. Unfortunately, the lines are to close to use any regions between the resonances so that xHPR does not improve the result and the simpler HPR can be used.

Next, for every time step, we can slice the 2D spectrum to get the intensity as function of Mössbauer detuning Δ_D. To this intensity the fit function of HPR (see Eq. (3.8)) or xHPR (see Eq. (3.45)) is fitted. The phase can be extracted with Eq. (3.11), the amplitude with Eq. (3.10). If the analyzer time spectrum is not known, an alternative approach for the sample's amplitude would be to integrate the 2D spectrum along the detuning axis or measure time spectra directly.

Performing those fits for every time step until a cutoff time t_cutoff gives the complex field amplitudes as function of time. A cutoff time has to be set because due to lower statistics for later times, results are noisy at late times. Depending on the demanded accuracy of the results, this cutoff can be earlier for nearly noisy-free results or later with only rough estimates at late times.

3.4.2 Cross check of material properties and energy calibration

In the toolchain (see Fig. 3.5), the material properties are received by fitting calculated time spectra to the measured time spectra. For more details see Section 2.5.2. In this fitting, the comparison is on the level of intensities. Being able to reconstruct the phase of the complex electric field allows us to also perform comparisons on the level of complex field amplitudes. Using complex field amplitudes is a qualitatively

different comparison than on the level of intensities because it also includes phase information. By comparing to calculated complex field, it provides a cross check for the calculated material properties.

In the future, the material characterization process might be improved by also fitting on the level of complex field amplitudes to use the phase information in addition.

Furthermore, the method itself gives a crosscheck for the energy calibration. If the calibration is not good enough, the fitted "oscillation frequencies" in Eqs. (3.8) and (3.45) do not match the measured data.

3.5 General usability of HPR and xHPR

The presented scheme of HPR in Section 3.5 is a solid tool to reconstruct complex electric field phases. It neither has a wavelengths dependency nor does it use nuclear forwards scattering properties. The only requirement is to record a detuning region without resonances in the 2D spectrum, so that coupling terms can be neglected. Thus, it can be used in a much wider field than nuclear resonant scattering.

However, the neglection of coupling terms at times with minimal intensity discussed in Section 3.2 is problematic whenever those situations occur, e.g. due to hyperfine splitting. The worst situation is given in the case where a beating between two frequencies appears. Here, it is advantageous to have more than two frequencies so that not all beatings result in minima at the same time (see Section 4.2.2).

The other possibility to deal with times with minimal intensity is to use xHPR. In Section 3.3, we showed that the additional correction terms lead to much better fits close to quantum beat minima than the HPR fits. In addition, a bigger detuning region can be used.

In contrary to HPR, the calculation of the correction terms in xHPR is based on nuclear forward scattering and thin foils in particular because of the applied approximations. However, the principles of this calculation can be used in other situations as well as long as certain conditions, that are discussed in the following, are fulfilled.

The quantum beat problem occurs for every beating with a small frequency difference compared to the absolute value of the frequencies, e.g. due to hyperfine splitting. Besides, the decay time has to be large enough so that several quantum beat cycles are detectable. In such settings, the quantum beat approximation in Eq. (3.25) is valid. If no such minima occur, the simpler HPR can be used.

Depending on the envelope, i.e. the Bessel function of first kind J_1 in case of nuclear forward scattering, a similarly simple approximation of the envelope by an exponential function like in the thin target approximation (see Eq. (3.23)) might be possible. If this simplification is not possible, the convolution probably does not give as simple expressions as in xHPR if solvable at all.

The third crucial approximation in the derivation of the xHPR fit model is the off-resonant approximation. If sample and analyzer are from the same material so

that there spectral properties are roughly the same, and if the lines are sufficiently narrow, this approximation is valid.

Summarizing, if the above criteria are met by the setup, xHPR can be used independently of x-ray energies or nuclear forward scattering.

Chapter 4

Heterodyne reconstruction of sub-Ångstrom motions

The measurement of small motions is essential in many different fields, such as high-precision technology [91], gravitational waves [27], quantum limits [92], optomechanics [93] or coherent control in x-ray quantum optics [41]. Here, we are mainly interested in the latter application.

As explained in Section 2.5.3, our standard method for motion reconstruction [41, 65] has to be run on a high performance computer to reconstruct the motion in the limited time of the live evaluation during the beamtime. The live reconstruction is necessary so that the starting point of the motion can be adjusted to achieve the desired jump amplitude of e.g. $\lambda/2$ in [41, 65] or to optimize the motion. The sample motion cannot be calculated just from the the applied voltage without the piezo motion because the response of the system is not known and non-trivial.

In addition, several measurements of 2D spectra at different delays, i.e. shifts of the motion into the measurable time window from 15 ns to 70 ns, are needed to reconstruct the full motion (see Section 2.5.3).

Thus, especially if more than one motion has to be reconstructed, the current techniques are very time and resource consuming. To scale up the number of samples or iteration cycles for motion optimization like in [110], computationally and experimentally more efficient reconstruction schemes are needed.

In this chapter we present a new technique to reconstruct motions on the sub-Ångstrom level by using extended heterodyne phase reconstruction (xHPR, see Chapter 3) for phase reconstruction. The principal idea is to compare the phase of the complex field with and without motion to identify the motion-induced phase as in [79]. First, the scheme is illustrated with simulated data in Section 4.1. Next, in Section 4.2, the usability with experimental data as well as the influence of the quantum beat problem on different experimental settings is evaluated. In Section 4.3, the optimization procedure introduced in Section 2.5.3 is discussed. After showing two different reconstructed motions in Section 4.4, the new scheme is compared to existing motion reconstructing techniques in Section 4.5. Finally, Section 4.6 explains how the new technique can be used in the existing data evaluation, which was already successfully done during the beamtime in May 2021, and under what conditions it can be used.

4.1 Illustration of working principle and first results

With a look back at Eq. (2.25), we see that for times $t > 0$, the motion-induced phase $\phi_{\text{motion}}(t)$ is given as the phase difference between the field with motion and the static case

$$\phi_{\text{motion ind}}(t) = \phi_{\text{motion}}(t) - \phi_{\text{static}}(t). \tag{4.1}$$

Using Eq. (4.1) and $\phi_{\text{motion ind}}(t) = kx(t)$, with the wave number k, the motion is given by

$$x(t) = \frac{\lambda}{2\pi} \left(\phi_{\text{motion}}(t) - \phi_{\text{static}}(t)\right). \tag{4.2}$$

The respective phases can be extracted with HPR or xHPR as presented in Chapter 3. In the case with motion, HPR has to be used because the convolution in xHPR can not be evaluated for arbitrary motions. Because of the phase reconstruction technique, the evaluation scheme is called heterodyne motion reconstruction (HMR).

Alternatively, the phase in the static case can be calculated from the material properties via `pynuss`. The latter approach reduces the noise of the static case as a reference because it does not depend on noisy, experimental data. In addition, it decreases the quantum beat problem (see Section 4.2.2). In this case, however, the whole calculation relies on material model assumptions and the material characterizations. Hence, depending on the situation, sometimes reconstructing the phase in the static case is better, sometimes calculating it from material properties. Usually, the choice of how the phase in static case is determined does not make a substantial difference to the reconstructed motion as demonstrated in Figs. 4.1, A.1 and A.2.

An example of the reconstruction of a motion from simulated data with HMR is shown in Fig. 4.1a for the static phase being reconstructed with xHPR and calculated from material properties. It can easily be seen, that the motions with static phase being reconstructed with xHPR and calculated from material properties agree within the errors, which are the standard variations of the fitting routine. Like in Chapter 3, Levenberg-Marquardt (least square) algorithm [130] is used. In addition, both agree with the motion used to create the simulated data. At the quantum beat minima (at about 7 ns, 21 ns, 36 ns, 50 ns, ...) significant deviations from the motion occur, especially for the reconstructed static phase. Those deviations are due to the quantum beat problem discussed in Section 3.2 and will be investigated in more detail in Section 4.2.2. For the motion with calculated static phase, the effect is not as strong because the quantum beat problem only effects the reconstructed phases.

4.2 Reconstruction from experimental data

After introducing HMR for simulated data, we now want to use it on experimental data. We will analyze two example motions. Motion “ramp2019” was measured in 2019 with only the two linear lines driven, while for the characterization of motion “magic2021” in 2021 all six lines were used. The evaluation is divided into three steps:

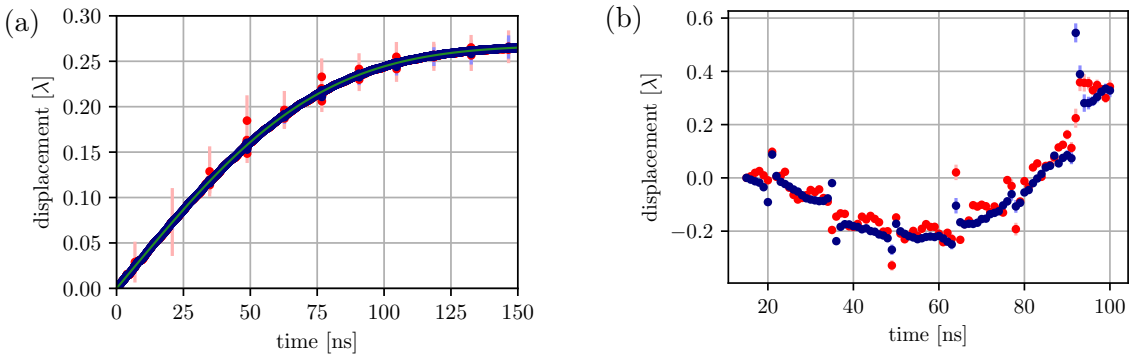

Figure 4.1: HMR reconstructed example motions from simulated (a) and experimental (b) data are shown. The motion in (b) is part of the motion "ramp2019". The static phase is either reconstructed with xHPR (red) or calculated from material properties (blue). For simulated data, also the actual motion is indicated (green). In both pictures, the angle of magnetization is $\alpha = \pi/2$, i.e. only the two linear lines are driven. The periodic discrepancies (at about 7 ns, 21 ns, 36 ns, 50 ns, ...) between actual and reconstructed motion in (a), especially for the reconstructed static phase, and deviations from the trend in (b) are due to quantum beats and will be discussed in more detail in Section 4.2.2. Errorbars indicate the standard deviation from the fitting routine (here the Levenberg-Marquardt (least square) algorithm [130]). The resonant regime between -45γ and 45γ is excluded from the analysis

the actual reconstruction (Section 4.2.1), an automatic exclusion of nonphysical points (Section 4.2.2) and a comparison of the different motion parts for different delays (Section 4.2.3).

4.2.1 Reconstruction step

In Fig. 4.1b, a reconstructed example motion using experimental data is shown. In the red motion, the static phase is reconstructed with xHPR, in the blue one it is calculated from material properties. The motions agree within the errorbars. However, the errors are only the standard deviations from the fitting routines. The statistical noise of the experimental data is not taken into account in the errorbars. Hence, they are underestimated.

The periodic deviations, especially in Fig. 4.1b at about 21 ns, 36 ns, 50 ns,... are due to minima of quantum beats and will be analyzed more closely in Section 4.2.2. What we can already note here is that the static phase calculated from material properties does not reduce the divergence at quantum beat minima as much as for simulated data (see Fig. 4.1a). In fact, they are on a similar level for reconstructed and calculated static phase, which might be due to an imperfect sample characterization or noise in the measured spectra.

In comparison to simulated data, experimental data limits the time range in which the motion can be reconstructed. As already explained in Section 3.4.1 lower count-

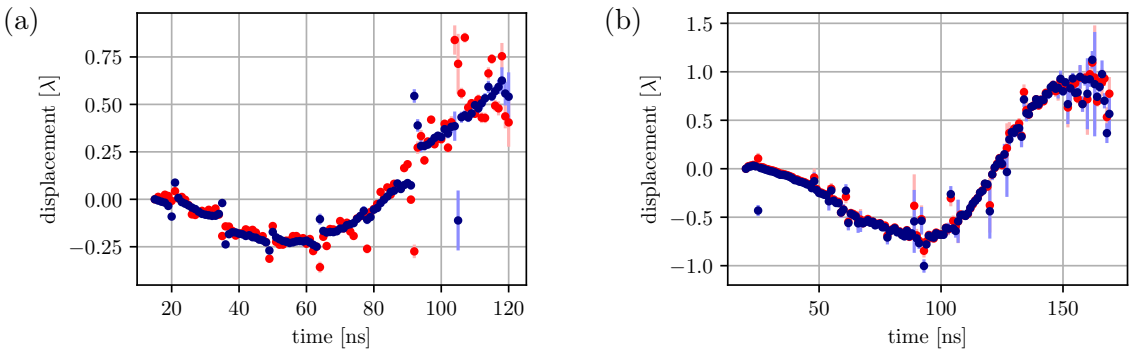

Figure 4.2: Reconstructed example motions to illustrate the different reconstruction times. In (a) only the two linear lines are driven ($\alpha = \pi/2$), while in (b) all six lines take part in the scattering ($\alpha = \pi/4$). The motion parts are from "ramp2019" (a) and "magic2021" (b), respectively. The data becomes significantly more noisy after 100 ns and 150 ns in (a) and (b), respectively. The colors indicate whether the static phase is reconstructed with xHPR (red) or calculated from material properties (blue).

ing statistics at later times lead to a noisy phase a those times. Depending on the demands, the cutoff time has to be chosen. For relatively noise free reconstructed motions, shorter reconstruction ranges should be chosen while for rough estimates of the motion bigger time ranges are accessible. The bigger the time range, the less delays are needed to characterize the full motion.

In the analysis, we recognized that the setup where only the two linear lines are driven has a shorter time range, in which the fit results have a rather constant quality, than the one where all six lines are driven. Typically, in the case with only the two linear lines being driven, reconstruction is possible until 100 ns, while for all six lines taking part in scattering it is possible to extract the motion until 150 ns. The times are demonstrated in Fig. 4.2, where example motions for 20 ns later than the above named standard cutoff times are displayed. It can clearly be seen that the motions get more noisy after 100 ns and 150 ns, respectively. Thus, whenever possible, the motion reconstruction should be carried out with all six lines driven.

HMR reconstruction times can be much larger than the one typically possible with the standard technique using evolutionary algorithms (about 55 ns, see [41, 65], Section 2.5.3). The longer reconstruction times allow a larger delay spacing and thus reduce the measurement time needed for reconstructing a motion.

The differences in the divergence at quantum beat minima for only the two linear lines or all six lines being driven will be analyzed in Section 4.2.2.

4.2.2 Automatic exclusion of nonphysical data points

We now want to focus on the divergences at quantum beat minima. As discussed in Section 3.2, at the quantum beat minima the oscillations are very small and dominated by other effects. Unfortunately, the extension introduced in Section 3.3

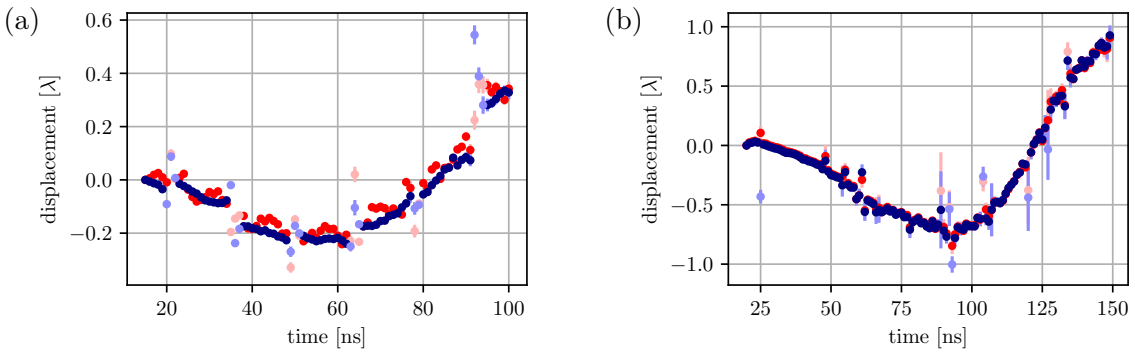

Figure 4.3: Reconstructed example motions to illustrate the quantum beat problem. In (a), only the two linear lines are driven, while in (b), all six lines take part in the scattering due to the chosen magnetic configuration. Again, the motion parts are from "ramp2019" and "magic2021", respectively. In the case of linear lines, every quantum beat minimum (at about 21 ns, 36 ns, 50 ns,...) the intensity goes to zero so that reconstruction at those times becomes difficult. In case of all lines being driven, only some quantum beats drop to zero as can be seen from Eq. (4.4). The divergence at the quantum beats can clearly be seen in (a). Hence, those times are automatically excluded in the automatic selection. In (b) the reconstruction is much smoother due to the intensity not dropping to zero (see main text). The shaded colors indicate the excluded data points from the automatic exclusion. The static phase is reconstructed with xHPR (red) or calculated from material properties (blue).

is only valid for the static case. Including a motion, makes the general analytical evaluation of the convolutions in Eq. (3.18) much more difficult. To our knowledge, it is not possible to evaluate the convolution for arbitrary motions.

As also already discussed in Section 3.2 the effect is worst, when only the linear lines are driven. In this case, the quantum beat minima approach zero at every oscillation because they are created by the single cosine term

$$\text{quantum beat term} = \cos\left(\Delta_{\text{hyp}} t\right), \tag{4.3}$$

in comparison to the case where all six lines are driven (see Eqs. (2.10) and (2.12))

$$\text{quantum beat term} = c_1 \cos(\Delta_{\text{hyp},1} t) + c_2 \cos(\Delta_{\text{hyp},2} t) + c_3 \cos(\Delta_{\text{hyp},3} t), \tag{4.4}$$

which is only zero for common multiples of the three frequencies $\Delta_{\text{hyp},1} = 53.6\gamma$, $\Delta_{\text{hyp},2} = 31.1\gamma$ and $\Delta_{\text{hyp},3} = 8.6\gamma$. The first roughly common minimum is at about 78 ns. However, the three lines do not reach their minimum at the very same time so that the effect is not as strong as the quantum beat minima in the case with only two lines driven.

As a comparison, example motions for only linear and all six lines being driven are shown in Fig. 4.3. For only linear lines in (a) the periodic discrepancies at quantum beat minima (at about 21 ns, 36 ns, 50 ns,...) are clearly visible. Those deviations are significantly above the noise floor and probably occur due to low contrast in

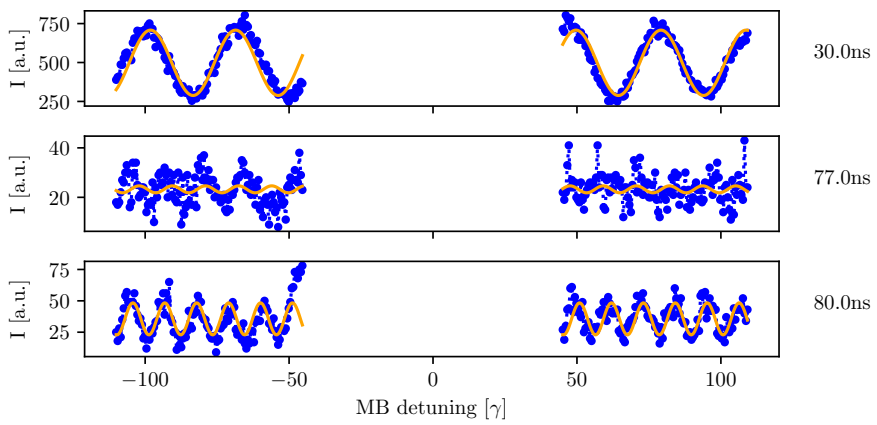

Figure 4.4: Experimentally measured intensity as function of Mössbauer detuning at three different times and its fits used in HPR (see Chapter 3). In the upper (center) plot, an example with high (low) contrast is shown. Because of the low contrast at a quantum beat minimum (77 ns), the fit results and thus the displacement at this time are not trustworthy. To demonstrate that the contrast is not due to the time, also the data and fit for 80 ns are shown in the bottom plot. The corresponding motion is the one with reconstructed static phase in Fig. 4.1b.

the intensity versus Mössbauer detuning plots at those times. An example for low (center) and high (top) contrast is shown in Fig. 4.4. While for high contrast the fit resembles the data, it fails for low contrast. In the lower plot, the data and fit for a later time are shown to demonstrate that the low contrast is an effect of the quantum beat minimum at 77 ns and not the late time. If the hyperfine splitting is known, which usually is the case, the positions of the quantum beats are well-known and can be excluded from the motions automatically. The excluded values are indicated by the shaded colors in Fig. 4.3. For all six lines being driven, we expect the unwanted effect to be less significant as explained above, which is indeed the case as can be seen from Fig. 4.3b.

Besides the longer reconstruction times, the smaller influence of quantum beat minima is an argument to characterize motions in a setting with all six lines driven whenever possible.

During the investigation of HMR, we realized that even off the quantum beat minima and not at late times, points exist that differ more than 0.3λ from their neighbours. Until now we have not found a third mechanism besides quantum beat minima and long times, that could explain those deviations. The piezo is not fast enough to jump on this level back and forth within two nanoseconds because of its inertia with respect to voltage changes. Thus, those data points are nonphysical and will also be excluded from the motion.

In Fig. 4.3, automatically excluded data points are shown in shaded colors. The remaining motion seems to be much smoother than before the automatic selection.

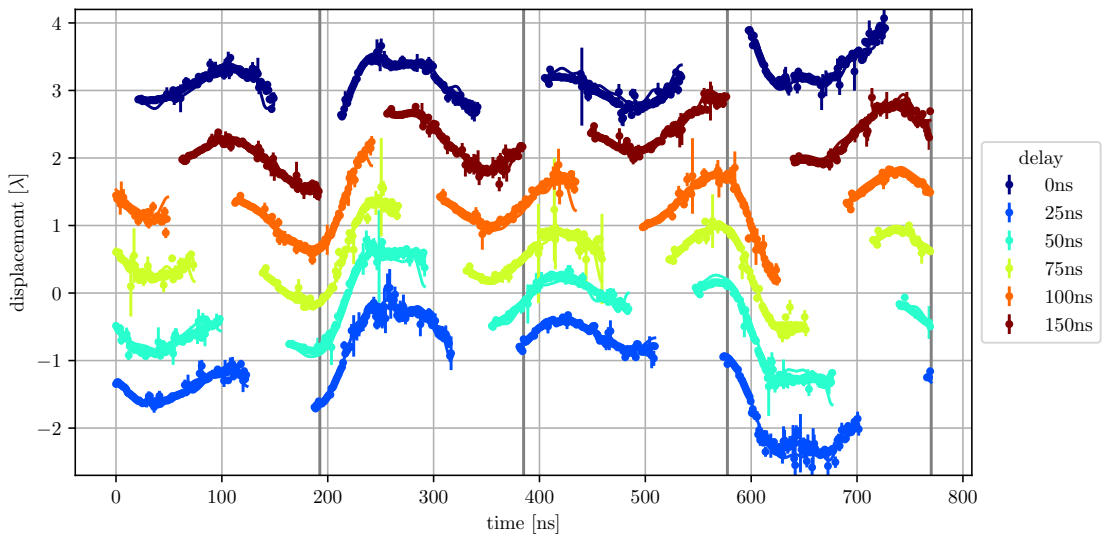

Figure 4.5: All reconstructed motion parts for "magic2021" (all six lines driven). The colors in the legend correspond to the different delays, that cover different regions of the motion and are used to "scan" the whole motion as illustrated in Fig. 2.11. Displacement offsets of the motion parts are arbitrary as discussed in Section 2.3.1 (more detail in main text). The motions parts agree within the errors. Excluded values are not shown for clarity. The gray vertical lines indicate the arrival of a synchrotron pulse for a delay of 0 ns.

4.2.3 Comparison of motion parts

After preparing the different motion parts, we can view them together to control whether they are consistent with each other. An example for all lines being driven ("magic2021") is shown in Fig. 4.5. A similar figure for only the linear lines taking part in the scattering ("ramp2019") is shown in Fig. A.3. The relative shifts between the motions parts are arbitrary as we can always set the starting point to a displacement of zero (see Section 2.3.1). Only, when the motion parts are combined into one motion, they have to be taken care of, such that a continuous motion is created. Here, they are set so that every motion part is clearly visible. In the overlapping regions, motions reconstructed from data measured with different delays agree with each other within the errors. In addition, less delays would still be sufficient due to the longer reconstruction times compared to the evolutionary algorithm results as already discussed in Section 4.2.1.

Sometimes, the automatic selection cannot exclude all nonphysical values because we decided for rather high threshold values to be significantly above the noise level and not accidently exclude values that are not nonphysical. In this step, also data points that do not fit into the motion trend can be excluded manually. However, if fitted splines (see Section 4.3) are used, single points slightly deviating from the motion trend do not have an influence on the whole motion.

The results after those three reconstruction steps will be referred to as pure HMR results in the following.

4.3 Optimization

In the old standard motion reconstruction scheme using evolutionary algorithms as explained in Section 2.5.3, the results of the evolutionary algorithms are used as an initial guess for a standard fit procedure to optimize the result with respect to the fitness. The evolutionary algorithm roughly gives the global minimum of the fitting measure. Standard fit routines can be used to find the local minimum in the neighbourhood of the rough global minimum.

The new HMR scheme in principle gives the global minimum. However due to the discussed problems at quantum beat minima and at late times that lead to exclusions of data points, it can be desirable to optimize the pure HMR data as well.

As explained in Section 2.5.3, fitting all data points has to many degrees of freedom. Hence, the pure HMR results will be represented by a fitted spline. For a successful optimization, the choice of the number of support points is crucial. A comparison between the pure HMR data and splines with different numbers of support points can be found in Fig. 4.6 for all motion parts of motion "magic2021" measured with all six lines driven. A similar plot for motion "ramp2019" measured with only the two linear lines driven is given in Fig. A.4.

For most motion parts the optimized splines with different numbers of support points agree with each other and already $N = 8$ support points are enough to closely reproduce the pure HMR data. However, for some panels (e.g. ref 1 and ref 3 for 0 ns) more support points ($N \geq 16$) are needed to reproduce the motion properly. Until now, we have not found systematics or even a reason for the significant deviations in the necessary number of support points. For a fast optimization a small number of support points N should be used because the Nelder-Mead algorithm scales linearly with the number of fitting parameters [131]. The N for which the error-weighted residual sum as compared to the pure data is lowest, i.e. best agreement between optimized spline and pure data, is displayed in the respective upper right corner.

For a fast live evaluation a small number of support points N should be chosen due to the linear scaling of N. A comparison to the pure HMR data like in Fig. 4.6 can reveal the motion parts for which the chosen N is not high enough. In those cases, higher N can be tested until agreement between optimized spline and pure HMR data is sufficient. In the detailed data evaluation after the experiment, when run time is not a crucial factor anymore, higher and various numbers of support points N can be tested for the best result.

The optimization depends on a meaningful fitting measure. Here, the measure is given by the Poissonian residuals [41, 125] of a calculated 2D spectrum with the motion to be fitted and the measured 2D spectrum. This measure is called fitness and is minimized in the chosen fitting routines. It sometimes favors nonphysical solutions as shown in Fig. 4.7. The red point is clearly nonphysical because the piezo cannot do such rapid displacements as discussed in Section 4.2.2. Nonetheless, including it results in a better fitness (937807) as without (938525). The difference is small (0.08%) compared to the changes during the fitting routines (above 1000%)

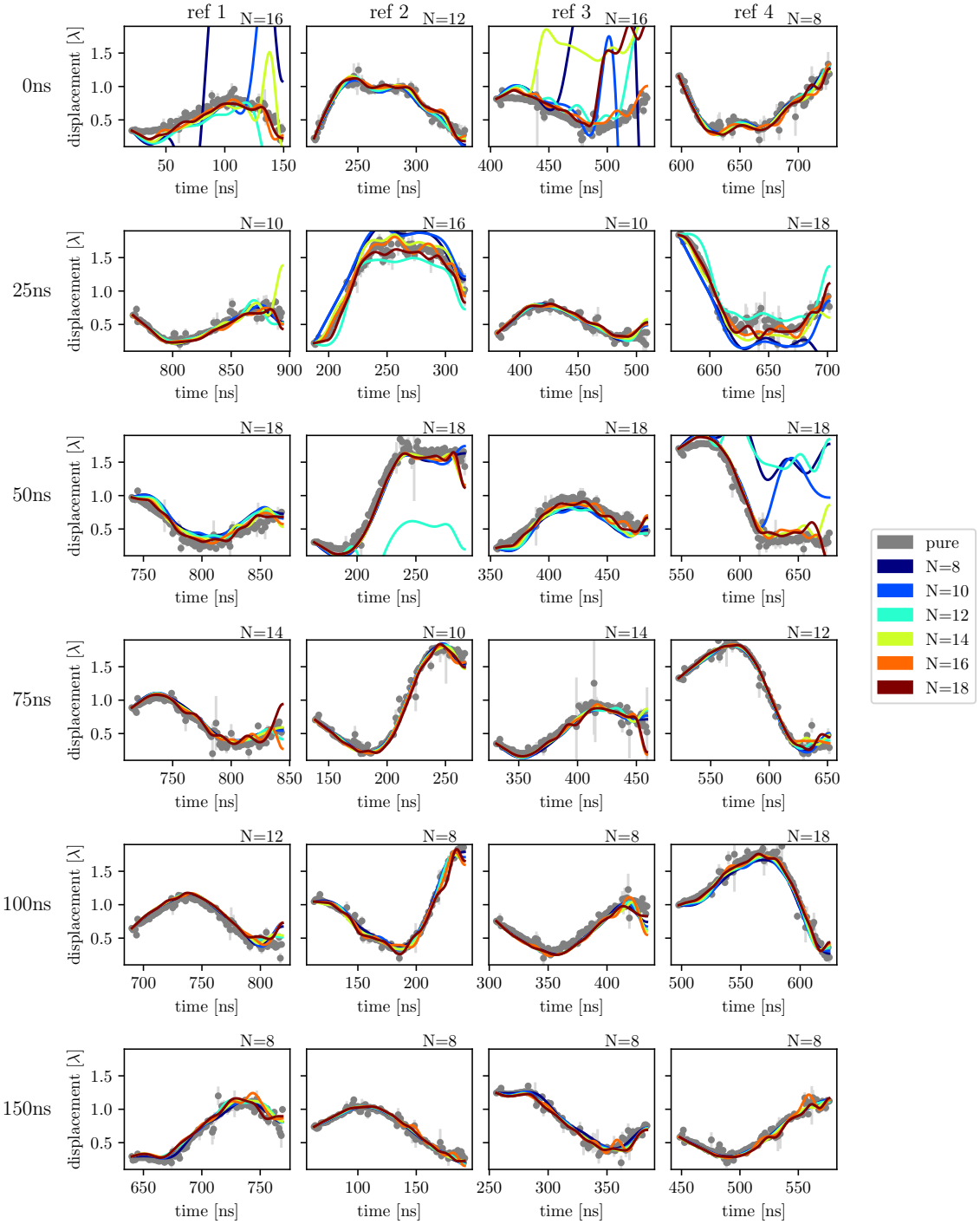

Figure 4.6: The pure HMR data (gray dots) as well as the optimized splines for several numbers of support points N (solid lines) are shown for the different motion parts of motion "magic2021". The N that fits the pure data best is printed in the respective right upper corner. For most panels, the optimized splines for different numbers of support points look rather similar. However, there are some parts (e.g. ref 1 and ref 3 for 0 ns) for which only a high number of support points ($N \geq 16$) represents the motion part properly.

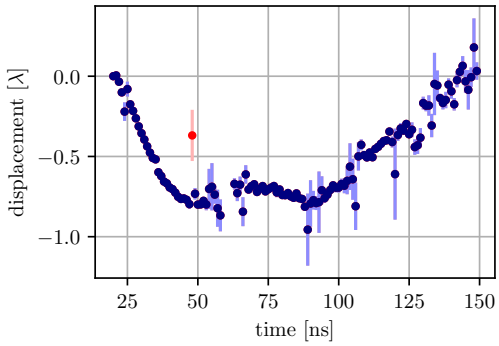

Figure 4.7: Example of fitness preferring nonphysical result. The red data point is clearly nonphysical as it is far off its neighbours and the piezo cannot do such rapid movements as discussed in Section 4.2.2. However, the fitness calculated with that point (937807) is better than the one without that point (938525). The difference is probably due to overfitting as explained in the main text. The example is part of "magic2021" and measured with all six lines driven.

and is probably due to too many free parameters. In the example, the displacement at every time step is a free parameters and influences the evaluation of the fitness. Without noise, the fitness should be best for the actual motion. However, including noise can lead to overfitting by using too many parameters because the noise is fitted as well. The overfitting can also happen if too many support points are used for the spline that is to be optimized.

From their construction, the pure HMR results should already be close to the optimum so that such small effects of physically wrong fitness variations occur. Thus, the optimized results should always be checked for physical meaningfulness and agreement with the pure HMR results. They might improve the results, but the improvements are by far not as big as for the evolutionary algorithms because the to be optimized results are already close to the optimum. The optimization is not necessary in live evaluation if time is crucial. However, they can improve the results in the actual evaluation after the experiment if analyzed carefully.

4.4 Resulting motions

In the last step all the motion parts can be combined together with the combination procedure described in Section 2.5.3.

An example motion measured with only linear lines driven ("ramp2019") is shown in Fig. 4.8. In addition, the slope differences between every pair of motions is displayed. Slopes provide a better comparison than displacements because the displacement differences depend on the absolute shift between the two motions that does not matter. The reason is that the displacement at the motion start can always be set to zero (see Section 2.3.1). The corresponding applied voltage at the piezo

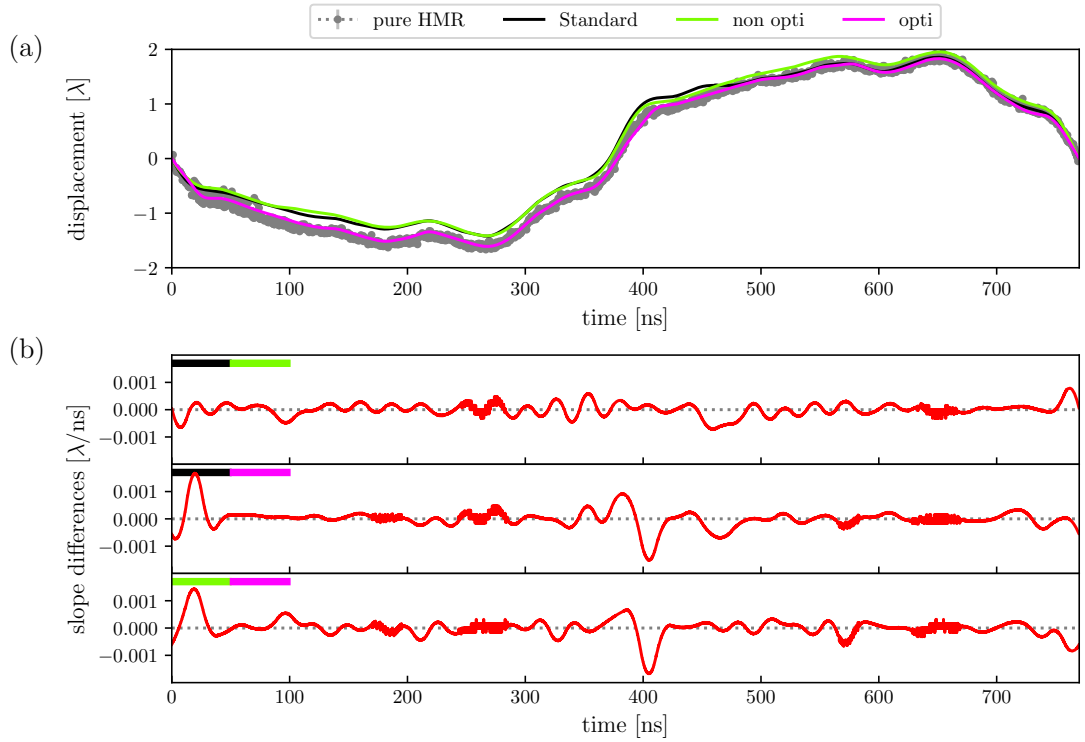

Figure 4.8: A few reconstructed motion versions for "ramp2019" are shown in (a). The motion parts are the results of evolutionary algorithms with optimization (black) as well as optimized (pink) and non-optimized (green) HMR results reconstructed with use of xHPR. For comparison the pure HMR data is shown as well (gray). The number of spline support points is chosen to be $N = 8$. In (b) pairwise comparison of the slopes can be found with the two colors corresponding to the two compared motion versions. The applied voltage at the piezo can be found in Fig. 4.10a.

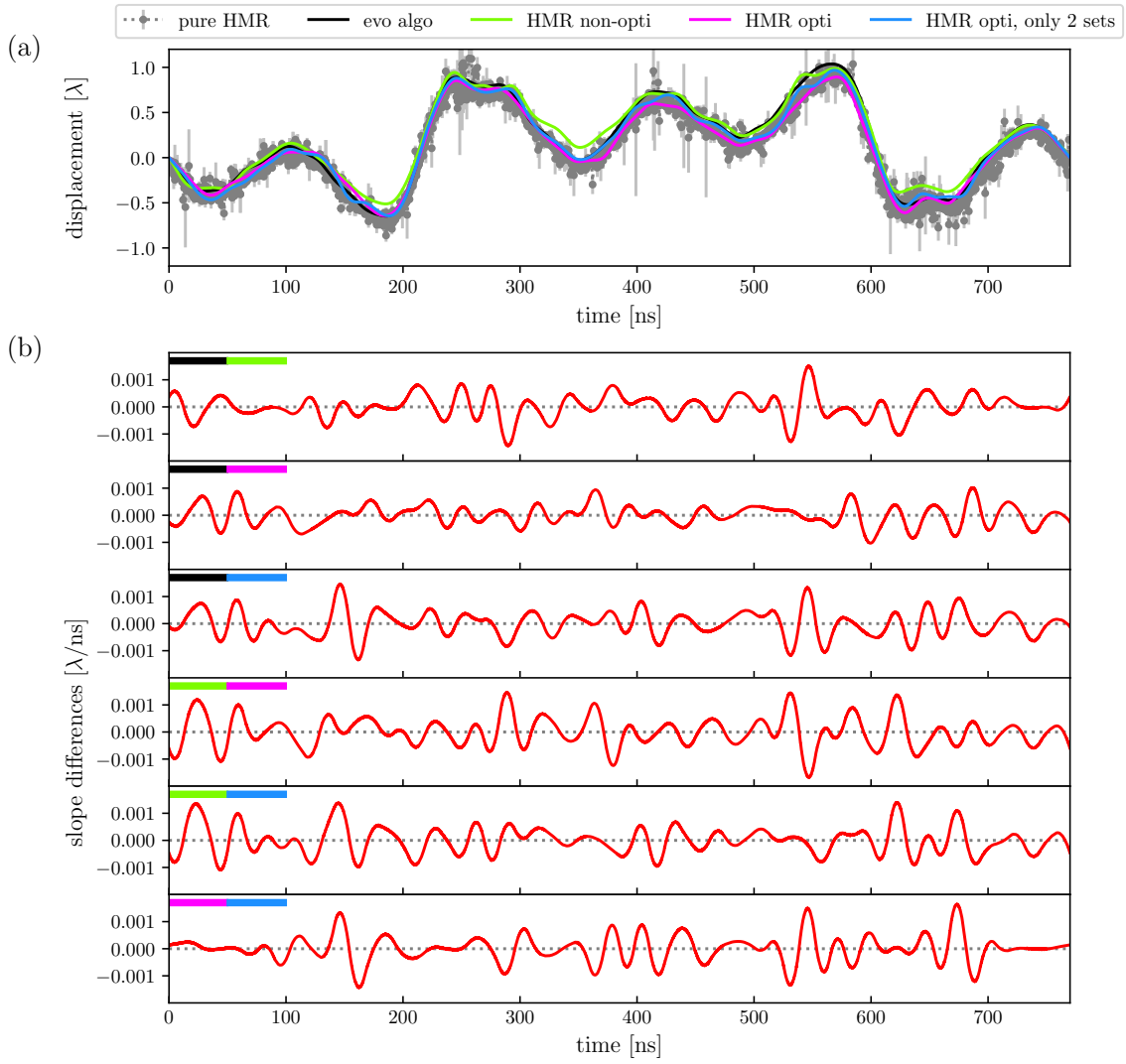

Figure 4.9: A few reconstructed motion versions for "magic2021" in (a). The motion parts are the results of evolutionary algorithms with optimization (black), optimized (pink) and non-optimized (green) HMR results reconstructed with use of xHPR as well as the reconstruction from only two delays (0 ns and 100 ns) of the optimized HMR results. For comparison the pure HMR data is shown as well (gray). The number of spline support points in HMR is chosen to be $N = 16$. A pairwise comparison of the slopes is shown in (b) with the colors indicating the compared motion versions. The applied voltage at the piezo can be found in Fig. 4.10b.

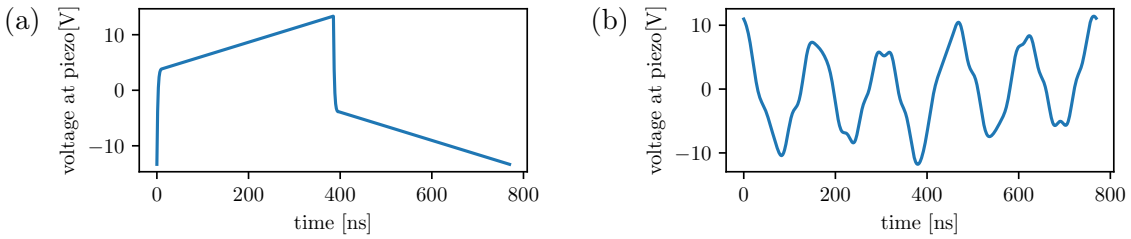

Figure 4.10: The applied voltages at the piezo corresponding to the reconstructed motions "ramp2019" in Fig. 4.8 and "magic2020" in Fig. 4.9, respectively.

can be found in Fig. 4.10a. The reconstructed motions with the different methods are very similar.

The main differences are close to 0 ns and 400 ns, where the steepest parts are. This result is expectable because absolute the slope differences are compared.

Differences between optimized and non-optimized HMR results are mainly caused at early times from about 0 ns to about 30 ns. The amount of difference is similar to the periodicity error of the pure HMR results, that can be seen from the discrepancy at early times. Thus, the discrepancies between optimized and non-optimized HMR results might be related to this periodicity error. At other times, they are approximately parallel.

The non-optimized HMR and optimized evolutionary algorithm results are nearly identical despite the time region at about 480 ns and at early times. On average, they have the lowest discrepancies. The same holds for the comparison between optimized HMR and optimized evolutionary algorithms results.

The optimized HMR results seems to agree best with the pure HMR data. However, the periodicity error in the pure HMR data shows that this data alone cannot represent the motion because we know that the motion is periodic.

In Fig. 4.9, an example motion measured with all six lines driven ("magic2021") is given with the corresponding applied voltage at the piezo in Fig. 4.10b. The bigger errorbars of the pure HMR data in Fig. 4.9 compared to Fig. 4.8 mainly result from large errorbars at later times (see Fig. 4.5). The reconstructed motions with the different methods are very similar and also the deviations are on a similar level. Like for "ramp2019", the motions have significant absolute shifts in some parts. Nonetheless, on the relevant time scale of a bunch cycle, i.e. 192 ns, the shifts are rather constant so that the influence is expected to be low. However, the shifts might be relevant when calculating the response function of the system to applied voltages.

In addition, it can be seen that in principle only two datasets would be enough for a reasonable reconstruction in case of all six lines driven with the long reconstruction time of 150 ns. The result with only two delays does not vary significantly more in the slope comparison than the other pairs. However, four measurements would be desirable to have enough overlap to reduce the periodicity error as explained in Section 2.5.3.

4.5 Comparison to other techniques

Besides the discussed method in this chapter, there are other methods e.g. using temporal phase interferometry too [79], direct fitting of motion [41, 65] or motion-induced Doppler-shifts [108]. In this section, we will compare the newly proposed method to those existing ones.

4.5.1 Evolutionary algorithms

First we want to compare HMR to the standard method in our tool chain [41], [65, supplement] shortly explained in Section 2.5.3. The main difference is that in the old standard scheme using evolutionary algorithms, the whole motion part, that is represented by a spline, is fitted in a single fit. In HMR, at every single time step of a motion part one (static phase calculated) or two fits (static phase reconstructed) are performed to receive the displacement at this time point. Because of the different representation, the evolutionary algorithm method does not have to deal with the quantum beat problem as the splines do not resolve those divergences on a few ns level.

While the evolutionary algorithms need about 30 minutes on the institute's high performance computer per motion part, HMR only takes about a second on a local computer. Thus, already shortly after the measurement a rough estimate for this motion part is available. The fast availability of results allows for quick adjustments of the experimental setup if needed. Furthermore, optimizing the result is not necessary, which saves additional time.

Another advantage of the new scheme is that it does not need any assumptions about the samples if the static phase is reconstructed with xHPR as well and no optimization is done. For the optimization, the measured spectra are compared to calculated ones. Whenever, a spectrum needs to be calculated model assumptions for the material, e.g. infinite sample approximation or whether a magnetic field distribution has to be fitted or not, and material characterization need to be used.

The longer reconstructions times of about 100 ns as compared to the standard approach with only about 55 ns in the case where only the two linear lines are driven is a clear advantage because it can reduce the measurement time significantly. For all lines driven, the effect might be even bigger with reconstruction times up to 150 ns, but reconstruction times of the old evolutionary algorithm method have not yet been analyzed in this configuration. The long reconstruction times would be essential for the usage of several moving targets or the "magic-waveform" scheme to achieve arbitrary piezo motions [110]. For both several motions need to be reconstructed. Until now, characterization measurements need to be done for every sample solemnly because there is not yet a scheme that can reconstruct the motion of two samples measured at the same time. In the "magic-waveform" approach the response function of the experimental system to the voltage pattern is determined from the first measured motion. From the response function, the needed voltage pattern for a desired motion can be calculated. Finally, this second motion needs

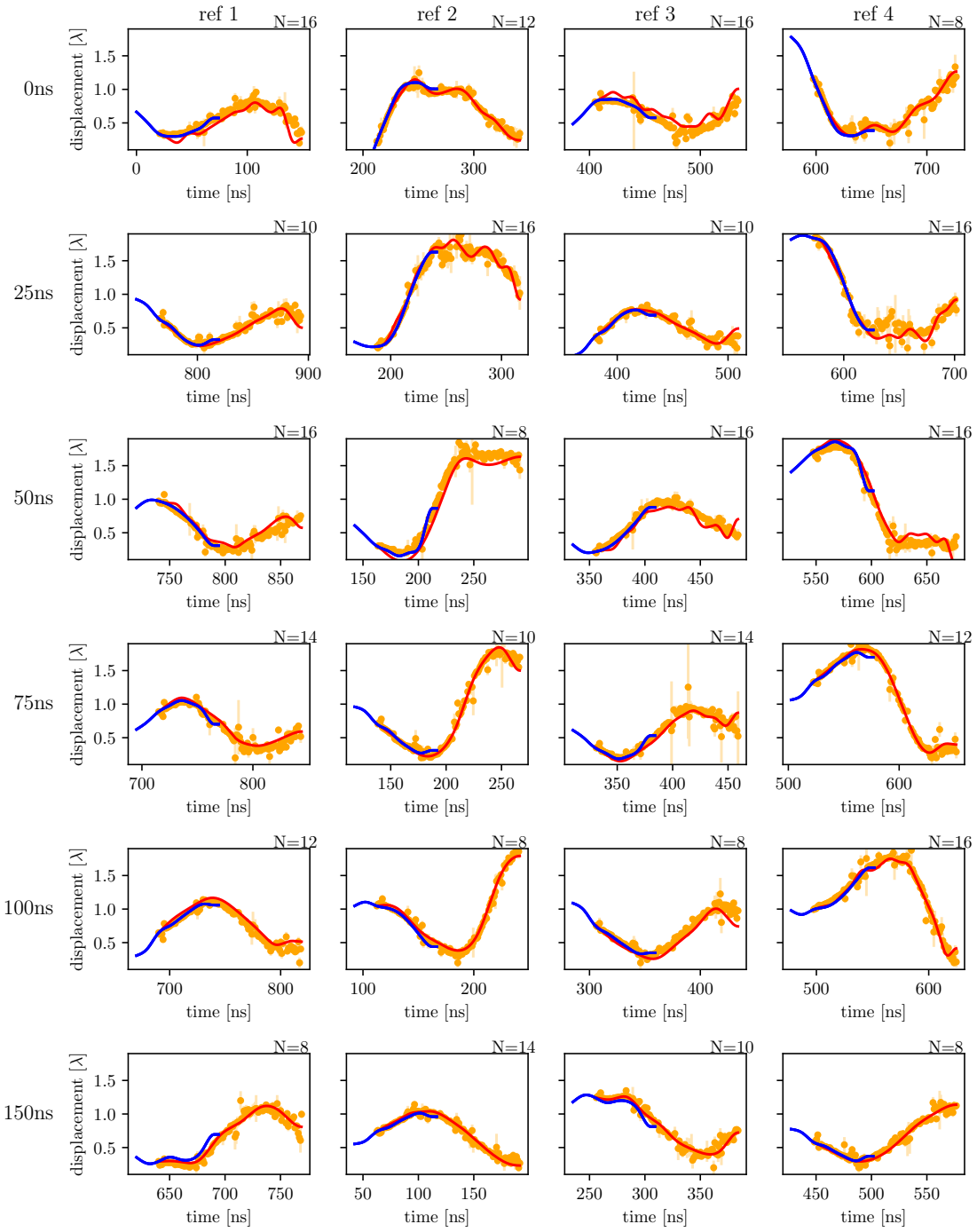

Figure 4.11: The pure HRM data from Section 4.2 (orange), the optimized spline (red) and the optimized result from evolutionary algorithms (blue) are shown for the different 2D spectra from which they are extracted. The plotted optimized spline with support number N as indicated in the right upper corner is the one with lowest deviation from pure HMR data. For a comparison of different support number see Fig. 4.6). Note that here, the evolutionary algorithms also fit in the veto region, hence starting 0 ns after the pulse arrival and ending at 70 ns.

to be characterized as well because it does not match the desired motion perfectly. Using this approach iteratively, would increase the needed motion even further.

In addition, the idea itself of HMR is advantageous over the method with evolutionary algorithms. While HMR fits the easily derived oscillation terms in Eqs. (3.8) and (3.45), the evolutionary algorithm fits are rather a black box. In the latter, the theoretically calculated 2D spectrum with the motion, that is fitted, is compared to the measured 2D spectrum with a Poissonian metric. This method gives much less insight than HMR.

Due to all the advantages, especially the time saving, for the live evaluation during the experiment, we will use HMR in the future. But for the actual offline evaluation of experimental data after the experiment, where time is not such a critical resource, the evolutionary algorithm scheme will be kept for cross-checking. A comparison of the motion parts reconstructed with HMR and evolutionary algorithms is shown in Fig. 4.11. Note that the evolutionary algorithms start 0 ns after the pulse arrival and end at 70 ns because they also fit in the veto region. Despite the single histograms giving the motion in slightly different time regions, the results of the two methods agree with each other. A similar figure for only the linear lines driven can be found in Fig. A.5.

4.5.2 Temporal phase interferometry near x-ray resonances

Another technique to retrieve the motion is the "Time-Resolved sub-Ångstrom Metrology by Temporal Phase Interferometry near x-ray Resonances of Nuclei" by Goerttler et al. [79]. The scales of the extracted motions are similar to ours. In this paper also a single line analyzer mounted on a Mössbauer drive is used to determine the phase of the sample's electric field. The principal idea is similar to HPR [78] only that instead of fits for every time step a Fourier transform is used.

Assuming no coupling, the combined electric field can be expressed by a background and an oscillation term (see Eq. (3.6)). The background can be subtracted by measuring the single responses of sample and analyzer. The remaining oscillation term is given by

$$\text{oscillation term} = e^{i[\phi(t)+\Delta t]}A(t) + e^{-i[\phi(t)+\Delta t]}A(t), \tag{4.5}$$

with the phase to be determined $\phi(t)$, the detuning Δ between sample and analyzer and a real amplitude $A(t)$ depending on the materials. Now, the phase is not determined by fitting a cosine function like in HPR, but with a Fourier transform.At high enough detuning $\Delta \gtrsim 3\gamma$, where γ is again the linewidth of the transition, the two terms are sufficiently separated in Fourier space. Only the positive oscillation term is transformed back to time space, efficiently truncating the oscillation term to

$$\text{oscillation term}' = e^{i[\phi(t)+\Delta t]}A(t), \tag{4.6}$$

which gives the phase $\phi(t)+\Delta t$ by reading out the argument of this complex function. Because Δ is known, argument directly gives the phase $\phi(t)$.

Similar to xHPR, the method can be used to determine the phase in case with and without motion. The difference between those two phases is the motion-induced phase and the motion is given by Eq. (4.2) again.

Despite the method to extract the phase information, the second main difference between the two approaches is the used detuning range. While HPR performs the analysis out of the region where the spectrum is expected (outside of $\pm 90\gamma$), Goerttler et al. stay close to the resonance (from $\Delta = \pm 3\gamma$ up to $\Delta = \pm 6\gamma$). As we have seen in the derivation of xHPR in Section 3.3, the region outside all resonances and between resonances behaves qualitatively different. However, the first order correction term in Eq. (3.44) can be considered constant in the used small regions from about $\pm 3\gamma$ to about $\pm 6\gamma$.

With their scheme, Goerttler et al. achieve reasonable results for the reconstructed motions. Unfortunately, the reconstruction times in this scheme also seem to be limited to about 35 ns. Nonetheless, a big advantage of that scheme is that it can use more of the measured data so that statistics are better. In addition, using a Fourier transform instead of a cosine fit automatically reduces the effects of quantum beat minima.

4.5.3 Quantum-beat analysis

A slightly different approach is used in the quantum-beat analysis by Schindelmann et al. [108]. The motion scales used there are again similar to our scales. Here, the motion is not extracted via the induced phase but the induced detuning with respect to a reference sample, which is placed behind the moving sample on a Mössbauer drive. Hence, the motion is not reconstructed via the displacement, but the velocities. Without motion, the Mössbauer detuning between the two samples causes quantum beats due to the slightly different frequencies. The beating frequency is determined by the relative detuning and thus the motion-induced detuning, that is directly proportional to the samples velocity v_{motion}, can be determined as the difference between beating frequency Δ_{beat} and Mössbauer detuning Δ_{D}

$$\frac{\omega_0}{c} v_{\mathrm{motion}} = \Delta_{\mathrm{motion}} = \Delta_{\mathrm{beat}} - \Delta_{\mathrm{D}}, \tag{4.7}$$

where ω_0 is the transition frequency and c the speed of light. Different Mössbauer detunings Δ_D can be used if the motion is not well-defined by a single time spectrum.

Schindelmann et al. successfully used that technique for motion reconstruction in case of two single line absorbers, where the beating frequency is clearly visible. However, it probably is challenging to do this analysis in the presence of magnetic hyperfine splitting due to more lines, that give additional beatings. The huge advantage of this technique is that it uses only time spectra, which can be measured much faster than 2D spectra.

4.6 Usage in data evaluation chain

The above new scheme to reconstruct the piezo motion was already used in the live evaluation during the last beamtime as well as in the offline evaluation after the experiment. The used extension of the tool chain is shown in Fig. 4.12. For discussion of the blue and red boxes regarding the reconstruction of the complex field amplitude see Section 3.4.

HMR can be used as an alternative to the evolutionary algorithm approach for reconstruction of motions. A comparison of the different motion parts reconstructed with the two methods can be found in Fig. 4.11. In the live evaluation during a beamtime, the new scheme is favourable because it is faster. For the actual data evaluation after the experiment both methods can be used to give a cross check. However, as HMR can deal with less delays, if both methods should be used, appropriate delays need to be chosen in the experiment.

4.6.1 Implementation of HMR

If possible, the measurements of the 2D spectra with motion should be performed with all six lines driven for the various reasons discussed above.

First, for the reconstruction step it has to be decided whether the static phase should be reconstructed with xHPR/HPR or calculated from material properties. Appropriate measurements, i.e 2D spectrum without motion or time spectrum of sample only, respectively, have to be available. Both methods have advantages and disadvantages as discussed in Section 4.2.1. In addition, the cutoff time has to be chosen. Here, a tradeoff between noise free data and long reconstruction times has to be made.

Next, the automatic exclusion can be done. Especially if only the two linear lines are driven, data close to quantum beat minima should be excluded because they diverge significantly as shown in Fig. 4.3. Additional nonphysical data points can be excluded as well in this step.

In the last step of pure HMR data processing, different motion parts can be viewed together so that agreement in the overlapping regions can be checked. Remaining nonphysical data points can also be excluded.

After the generation of pure HMR data, it can be decided whether this data should be optimized with the standard optimization procedure used for evolutionary algorithms. As discussed in Section 4.3 the optimization is not always necessary, especially not in the live evaluation during the beamtime where the time might not be sufficient. However, it can improve the results.

Finally, the motion parts for different delays can be combined into one motion as described in Section 2.5.3.

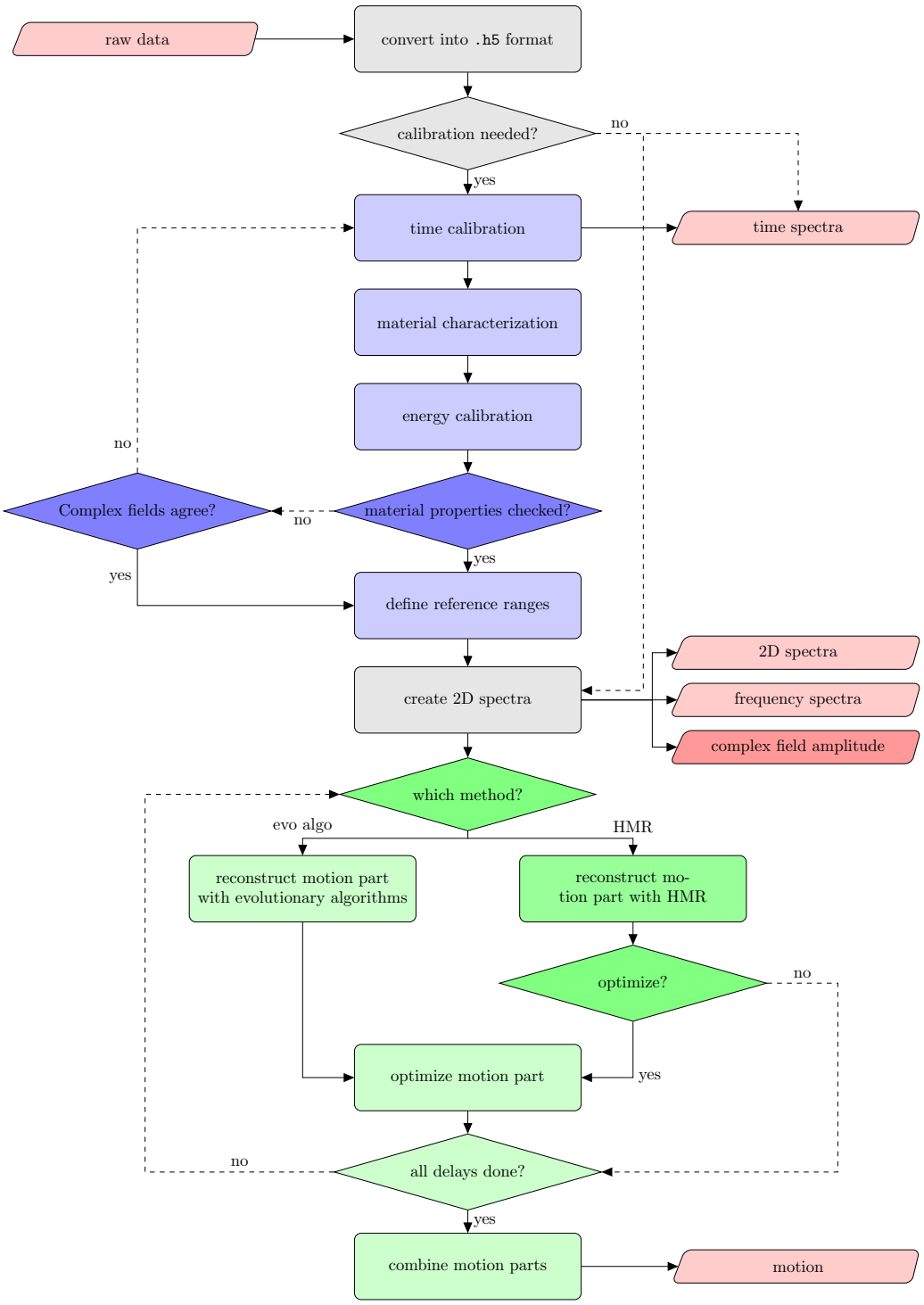

Figure 4.12: The complete extended tool chain as used for the live and detailed post-experiment data evaluation of the beamtime in May 2021. The light colors correspond to the standard tool chain as shown in Fig. 2.10, the strong colors to the newly inserted blocks with the new blue and red parts explained in Section 3.4. The new motion reconstruction scheme (strong green parts) can be used as an alternative to the standard technique using evolutionary algorithms. For details see Section 4.6 in the main text.

4.6.2 General usability

The presented HMR scheme for motion reconstruction can be used whenever the motion induces a phase and HPR is usable. This is the case if two electric fields interfere with each other, but coupling can be ignored at least in parts of the frequency spectrum. In addition, 2D spectra have to be measurable. Thus HMR like HPR is not limited to the field of nuclear forward scattering.

A limit is given for the slope of the motion. For every time step, a phase ϕ and another phase $\phi + 2\pi$ are indistinguishable. In our current setting we know, that phase changes greater than 2π within one time step cannot occur. This knowledge gives us well-defined phase changes with respect to the neighbours and hence a well-defined motion. However, if phase changes bigger than 2π are physically possible within a time step, the motion is not well-defined anymore. Those large phase jumps can happen by either more rapid changes or larger time steps. In those cases the motion has to be roughly known on the order of multiples of 2π.

Part II

Polarization interferometry measurements

Chapter 5

Temporal pulse shaping

In quantum optics at visible frequencies, a wide range of different pulse shapes in the temporal and spectral domain is available. At x-ray frequencies, pulse shaping is much more difficult because the standard techniques from the optical regime cannot simply be transferred. One of the main difficulties is that the refractive index of any material is close to unity. However, spectral pulse shaping was achieved e.g. in [65], temporal pulse shaping e.g. in [42, 44, 99, 107, 108, 109].

In this chapter, we focus on a different method using a polarization interferometer [95], which allows fast and adaptive pulse shaping. It consists of two samples with angles of magnetization $\alpha = \pm\pi/4$ with respect to the incoming polarization placed inside a polarimeter. This setting can be interpreted as an interferometer, whose arms are created by two orthogonal polarization channels. Placing one sample on a piezo electric element to move it on the order of wavelength allows to control the interference between the two samples. Selecting only one output polarization with the analyzer of the polarimeter allows to translate the interference into output intensity. Thus the piezo motion can be used for pulse shaping. In principal double pulses or even whole pulse trains with fixed phase relation can be created. Double pulses are essential for e.g. Ramsey spectroscopy.

This chapter starts (see Section 5.1) with the theoretical background of how a polarization interferometer works and and how it can be used for switching. This basic work was performed outside the scope of this thesis [94, 95]. Next, in Section 5.2 the basics of the experiment on temporal pulse shaping, which was prepared, performed and evaluated in the scope of this thesis, are explained. Finally, the actual results of the experiment are presented in Section 5.3 and discussed in Section 5.4.

5.1 Theory behind fast adaptive x-ray optics

The work presented in this section was done before this thesis in [94, 95]. It is summarized here because it lays the foundation for the performed experiment.

5.1.1 Mechanically-induced refractive index enhancement

Light with wavelength ω propagating through a material with refractive index [14]

$$n(\omega) = 1 - \delta(\omega) + i\beta(\omega) \tag{5.1}$$

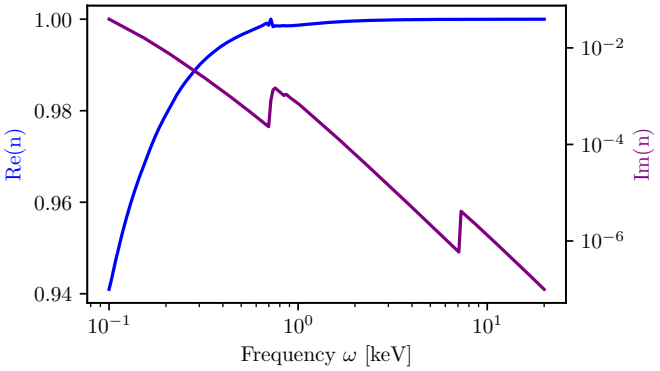

Figure 5.1: The refractive index of iron for different frequencies. The real (imaginary) part of the refractive index determines the phase (absorption) of light propagating through an iron sample. Data created with python package `xraylib` [132].

and thickness d acquires an additional phase and is absorbed. The propagation is represented by multiplying the incident field with the following term

$$e^{in(\omega)kd} = e^{ikd}e^{-i\delta(\omega)kd}e^{-\beta(\omega)kd}, \tag{5.2}$$

where k is the corresponding wave number. The first part is the phase from vacuum propagation, the second term the phase that can be manipulated with material properties and the last one is the absorption term.

In the optical regime, this second phase term is used e.g. for building waveplates. However, at x-ray energies δ is very small as shown in Fig. 5.1 resulting in small phase shifts from which it is difficult to build optical elements. Nonetheless, different approaches e.g. using diamond phase plates [133] were found to overcome this problem.

Here, we want to explain a different scheme. The motion-induced phase introduced in Section 2.3 can be used for mechanically-induced refractive index enhancement [94, 95]. The motion adds an additional phase to the one in Eq. (5.2)

$$e^{in(\omega)kd}e^{ik\Delta x} = e^{ikd}e^{-i(\delta(\omega)kd-k\Delta x)}e^{-\beta(\omega)kd}, \tag{5.3}$$

where Δx is the displacement. Due to the small δ, the motion-induced phase can be much larger and dominates the second term. Thus, effectively with a controlled motion, the real part of the refractive index can be enhanced by adding the motion-induced term $\Delta x/d$

$$n'(\omega) = 1 - \left[\delta(\omega) + \frac{\Delta x}{d}\right] + i\beta(\omega). \tag{5.4}$$

This modified refractive index can be used for building optical devices at x-ray energies as proposed in [94, 95].

5.1.2 Polarization manipulation in general

The key idea to use mechanically-induced refractive index enhancement for optical elements is to imprint the modified phase on only one polarization component. This phase manipulation can be done by choosing an appropriate angle of magnetization α. Using Eq. (2.14), this angle is included by rotation matrices $\mathbf{R}_\alpha$ [122]

$$\hat{\vec{E}}(\omega) = \mathbf{R}_\alpha \begin{pmatrix} \hat{R}_{\mathrm{circ}}(\omega) & 0 \\ 0 & \hat{R}_{\mathrm{lin}}(\omega) \end{pmatrix} \mathbf{R}_\alpha^{-1} \hat{\vec{E}}_{\mathrm{in}}(\omega). \tag{5.5}$$

Also including the motion-induced phase ϕ gives

$$\hat{\vec{E}}(\omega, \phi) = \mathbf{R}_\alpha \begin{pmatrix} \hat{R}_{\mathrm{circ}}(\omega, \phi) & 0 \\ 0 & \hat{R}_{\mathrm{lin}}(\omega, \phi) \end{pmatrix} \mathbf{R}_\alpha^{-1} \hat{\vec{E}}_{\mathrm{in}}(\omega), \tag{5.6}$$

where

$$\hat{R}_{\mathrm{lin/circ}}(\omega, \phi) = 1 + \hat{R}^S_{\mathrm{lin/circ}}(\omega) e^{i\phi} \tag{5.7}$$

is the response function including motion in analogy to Eq. (2.25).

With a phase of $\phi = \pi/2$ the motion-induced refractive index enhancement can be used to convert linear into circular polarization and vice versa, while $\phi = \pi$ allows to rotate linear polarizations. In the following, we will concentrate on the latter application. The phase shifts can be applied on the piezo timescale, which is about 10 ns to 20 ns.

5.1.3 Polarization interferometer

Using mechanically-induced refractive index enhancement to rotate incoming polarized light in combination with a polarimeter enables a polarization interferometer at x-ray energies..

The principal setup is shown in Fig. 5.2. The polarimeter is mounted in crossed setting. That means that polarizer and analyzer are perpendicular to each other so that no light can pass the setup if the polarimeter is empty. To also not let any light pass through the setup in the case of static samples being inserted in the polarimeter, a second sample perpendicular to the first one is needed as will be shown in the following.

With Eq. (5.6), the Jones matrix of a nuclear sample is given by

$$\begin{aligned} \mathbf{M}_\pm(\omega, \phi) =& \mathbf{R}_{\pm\pi/4} \begin{pmatrix} \hat{R}_{\mathrm{circ}}(\omega, \phi) & 0 \\ 0 & \hat{R}_{\mathrm{lin}}(\omega, \phi) \end{pmatrix} \mathbf{R}_{\mp\pi/4} \\ =& \frac{1}{2} \begin{pmatrix} \hat{R}_{\mathrm{circ}}(\omega, \phi) + \hat{R}_{\mathrm{lin}}(\omega, \phi) & \pm \left[\hat{R}_{\mathrm{circ}}(\omega, \phi) - \hat{R}_{\mathrm{lin}}(\omega, \phi) \right] \\ \pm \left[\hat{R}_{\mathrm{circ}}(\omega, \phi) - \hat{R}_{\mathrm{lin}}(\omega, \phi) \right] & \hat{R}_{\mathrm{circ}}(\omega, \phi) + \hat{R}_{\mathrm{lin}}(\omega, \phi) \end{pmatrix}. \end{aligned} \tag{5.8}$$

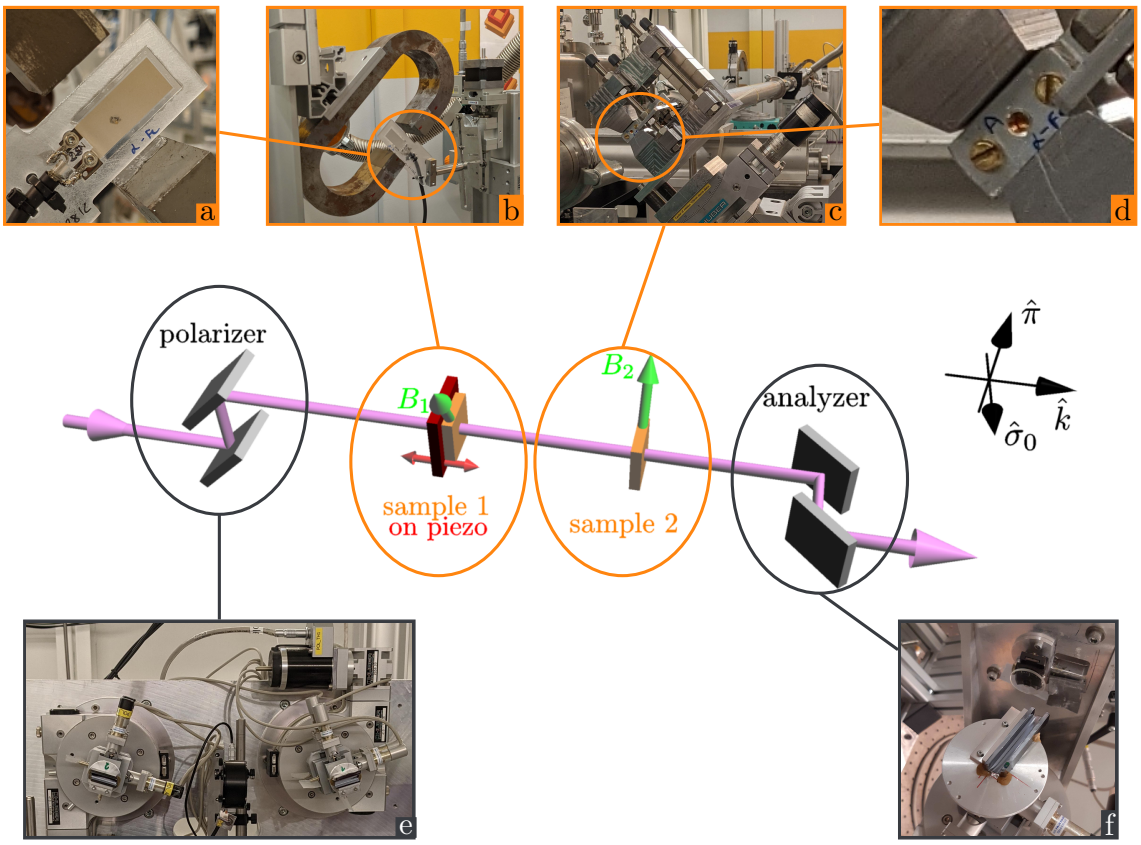

Figure 5.2: The setup for temporal pulse shaping consists of a polarizer-analyzer setup in crossed setting (gray) [134] and two samples (orange) with angles of magnetization $\alpha_{1/2} = \pm\pi/4$. One of the two samples is mounted on a piezoelectric element (red) so that it can be moved on the order of wavelength. The experimental components can be seen in the inlets: (a) shows the sample (silver) glued onto the piezo (beige). For stability, the piezo is fixed on an acrylic glass plate. The magnet that aligns the magnetic field and hence sets the angle of magnetization for the moving sample (sample 1) and static sample (sample 2) are displayed in (b) and (c), respectively. (d) is a close up of the sample foil in (c). It can be seen through the small hole in the center. The polarizer and analyzer are shown in (e) and (f), respectively. Photos by Jörg Evers and myself.

If we assume the incoming light to be polarized along $\hat{\sigma}_0$, the electric field behind the first sample according to Eq. (5.6) is given by

$$\begin{aligned}\hat{\vec{E}}_1(\omega, \phi = 0) =& \mathbf{M}_+(\omega, \phi = 0) \begin{pmatrix} 1 \\ 0 \end{pmatrix} \\ =& \frac{1}{2} \begin{pmatrix} \hat{R}_{\text{circ}}(\omega, 0) + \hat{R}_{\text{lin}}(\omega, 0) \\ \hat{R}_{\text{circ}}(\omega, 0) - \hat{R}_{\text{lin}}(\omega, 0) \end{pmatrix}. \end{aligned} \tag{5.9}$$

There is still some scattering from incoming $\hat{\sigma}_0$-component into the perpendicular $\hat{\pi}$-component so that light would be able to pass the polarimeter in crossed setting. In this case, the effect of polarization rotation would be more difficult to detect. Fortunately, the scattering into perpendicular component vanishes due to destructive interference if including a second sample. The combined field after both samples is given by

$$\begin{aligned}\hat{\vec{E}}_2(\omega, \phi = 0) =& \mathbf{M}_-(\omega, 0)\mathbf{M}_+(\omega, 0) \begin{pmatrix} 1 \\ 0 \end{pmatrix} \\ =& \begin{pmatrix} \hat{R}_{\text{lin}}(\omega, 0)\hat{R}_{\text{circ}}(\omega, 0) \\ 0 \end{pmatrix}. \end{aligned} \tag{5.10}$$

Taking motion-induced phases into account the electric field behind the second sample is given by

$$\hat{\vec{E}}_2(\omega, \phi) = \begin{pmatrix} 2\hat{R}_{\text{lin}}(\omega, \phi) + 2\hat{R}_{\text{circ}}(\omega, \phi) - 2\hat{R}_{\text{lin}}(\omega, \phi)\hat{R}_{\text{circ}}(\omega, \phi) \\ -2\left[\hat{R}_{\text{circ}}(\omega, \phi) - \hat{R}_{\text{lin}}(\omega, \phi)\right] \end{pmatrix}. \tag{5.11}$$

It can be shown, that the intensity in the perpendicular component, i.e. the $\hat{\pi}$-component, is given by

$$I_{\hat{\pi}}(\omega) = I_{\text{in}} \sin^2(\phi/2) \left| R_{\text{circ}}(\omega) - R_{\text{lin}}(\omega) \right|^2. \tag{5.12}$$

Hence, the strongest signal in the $\hat{\pi}$-component is achieved with $\phi = \pi$.

A few example spectra and their corresponding motions are given in Fig. 5.3. In Fig. 5.3a, the influence of different motion starting times can be seen. In the static case no light can pass the setup. For both motions, the count rate rises significantly at the time where the motion starts. Also a switching off effect is visible for the red motion when it jumps back to zero displacement. After this backjump, it is significantly suppressed compared to the black motion that stays at a displacement of $\lambda/2$. Fig. 5.3b demonstrates the influence of different rise times. In the spectra significant differences due to different displacements at the respective times can be seen. Once, the different motions have reached their plateaus, the spectra are the same again.

The setup with both samples can also be interpreted as an interferometer where the two arms are realized by the two orthogonal polarization directions as explained in the following.

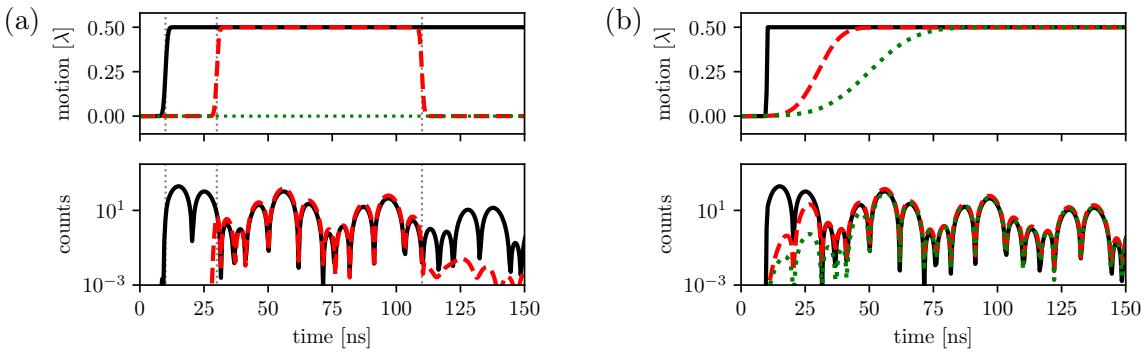

Figure 5.3: Different motions of first sample (top) and their corresponding spectra behind the polarimeter in crossed setting (bottom). In (a) different switch-on times as well as the influence of switching off is shown. (b) illustrates the influence of different rise times.

Without loss of generality, we concentrate on linear transitions ω_{lin}. For simplicity, in this illustrative derivation we will use two approximations. The first one is full absorption at the resonance, so that $R_{\text{lin}}(\omega_{\text{lin}}, \phi = 0) \approx 0$. With Eq. (5.7), this assumption leads to $R^S_{\text{lin}}(\omega_{\text{lin}}) \approx -1$ and thus

$$R_{\text{lin}}(\omega_{\text{lin}}, \phi) \approx 1 - e^{i\phi}. \tag{5.13}$$

The second approximation is that the other resonances are well-separated so that they do not interact with ω_{lin} and it is

$$R_{\text{circ}}(\omega_{\text{lin}}, \phi) \approx 1. \tag{5.14}$$

With this result, also Eq. (5.8) simplifies to

$$M_{\pm}(\omega_{\text{lin}}, \phi) = \frac{1}{2} e^{i\phi} \begin{pmatrix} 2e^{-i\phi} - 1 & \mp 1 \\ \mp 1 & 2e^{-i\phi} - 1 \end{pmatrix}. \tag{5.15}$$

The global phase $e^{i\phi}$ can be neglected in the following. Thus the two samples' Jones matrices are given by

$$M_1(\omega_{\text{lin}}, \phi) = \frac{1}{2} \begin{pmatrix} 2e^{-i\phi} - 1 & -1 \\ -1 & 2e^{-i\phi} - 1 \end{pmatrix}, \tag{5.16}$$

$$M_2(\omega_{\text{lin}}, 0) = \frac{1}{2} \begin{pmatrix} 1 & 1 \\ 1 & 1 \end{pmatrix}, \tag{5.17}$$

where we used that the second sample is static and hence there is no motion-induced phase $\phi = 0$.

Similar considerations can be done for the circular transitions ω_{circ} resulting in

$$M_1(\omega_{\text{circ}}, \phi) = \frac{1}{2} \begin{pmatrix} 2e^{-i\phi} - 1 & 1 \\ 1 & 2e^{-i\phi} - 1 \end{pmatrix}, \tag{5.18}$$

$$M_2(\omega_{\text{circ}}, 0) = \frac{1}{2} \begin{pmatrix} 1 & -1 \\ -1 & 1 \end{pmatrix}. \tag{5.19}$$

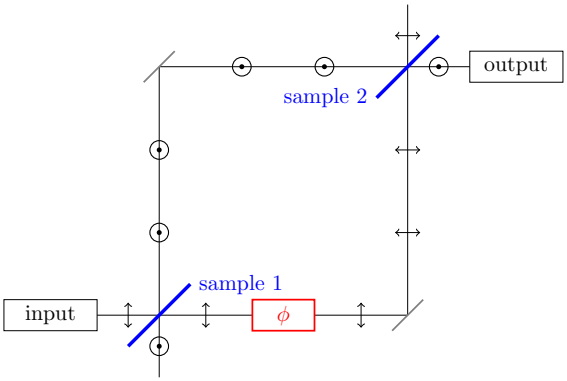

Figure 5.4: A schematic picture of the polarization interferometer with the two polarization paths indicated by the arrows. In reality, the two paths are not separated spatially. The two samples act analog to beam splitters. In addition, the first sample imprints a phase $2 - e^{i\phi}$ if only one input is considered, which can be set by the polarizer. Besides, with the analyzer also only one output is selected.

If we assume, the incident light to be polarized along the $\hat{\sigma}_0$-direction, for linear as well as circular transitions, the first sample acts like a beamsplitter and imprints a phase $2e^{-i\phi}-1$ onto the $\hat{\sigma}_0$-component. The second sample recombines the two paths like a beamsplitter in both cases. For the beamsplitter analogy, we do not consider, that in an optical beam splitter the reflected parts would acquire additional phases. A schematic of the polarization interferometer can be found in Fig. 5.4. Note that in reality, the two paths are not separated spatially. The interference and thus the intensity at the output can be controlled by ϕ as shown in Eq. (5.12).

5.2 The experiment

An experiment to show the switching explained above was performed at beamline P01 at DESY [116] in cooperation with groups around Thomas Pfeifer (MPIK Heidelberg), Ralf Röhlsberger (FSU/HI Jena) and Ingo Uschmann/Gerhard Paulus (FSU/HI Jena).

Preparation, execution and the whole evaluation of the experiment was done in the scope of this thesis. In this section, an overview over the experiment itself is given.

5.2.1 Experimental setup

Hardware. The experimental setup is shown in Fig. 5.2. It contains a polarizer-analyzer setup (inlets e and f) in crossed setting [134]. The moving sample (sample 1) is a mm-sized ^{57}Fe-enriched foil mounted on a piezoelectric element (Measurement Specialities Inc. DT1-028K/DT1-052K) [123] (inlet a). Its magnetic hyperfine field is aligned with a magnet (see inlet (b)) to achieve an angle of magnetization $\alpha = +\pi/4$. The whole component is placed on a rotation stage to adjust the angle with

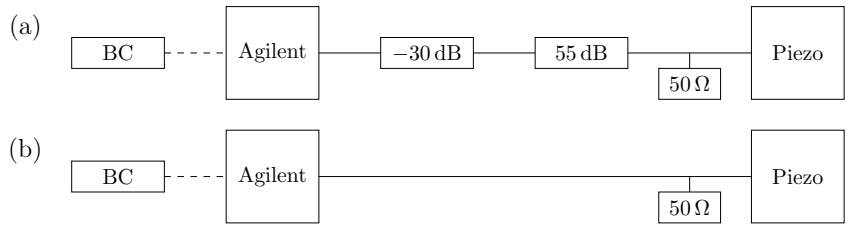

Figure 5.5: The Agilent-piezo circuit with (a) and without (b) the 55 dB amplifier. To not have too high voltages at the amplifier, a 33 dB attenuator is used. The piezo is in parallel with a 50 Ω resistor. To have the voltage be synchronized with the pulse arrival, the agilent is triggered by with the Bunch Clock (BC).

the polarization plane θ_1 as defined in Section 2.1. The static sample is again a mm-sized ^{57}Fe-enriched foil, but fixed between aluminum plates with a kapton foil as can be seen in (c) and (d). The two metal plates have a small hole in the center to let the beam pass as shown in (d). It is mounted within a magnetic field as can be seen in (c). A rotational stage is used to adjust the angle of magnetization $\alpha_2 \approx -\pi/4$ for best destructive interference. Light passing through the setup is collected with avalanche photodiodes (APDs, not shown).

Software and electronics. An event-based detection system from RoentDek is used to store the photon arrival time with respect to the pulse arrival, the current Mössbauer velocity and the current reference range for bunch identification (see Section 2.5.2, [41]).

For the piezo voltage supply an Agilent arbitrary waveform generator (Keysight 81160A-002 [124]), that will be called agilent in the following, is used. It can provide arbitrary voltage patterns with ns resolution. The agilent's output is either damped by −30 dB and amplified with 55 dB afterwards increasing the voltage by a factor of 17.78 (measurements with amplifier) or connected directly to the piezo (measurements without amplifier) to reduce background noise as explained in Chapter 6. The piezo is connected in parallel with a 50 Ω resistor to determine the transmission line between agilent and piezo. Otherwise, there would be oscillations at the cable ends. In addition, the agilent voltage only delivers the chosen voltage at an impedance of 50 Ω. The agilent can be triggered by the bunch clock, that simply gives a signal for every synchrotron pulse arrival. The respective circuits are shown in Fig. 5.5.

5.2.2 Sample characterization

Sample properties can be characterized by fitting the desired properties to a measured time spectrum, i.e. counts as function of time. More details on the general method can be found in Section 2.5.2.

Here, we fit the thickness d, internal magnetic hyperfine field B, angle of magnetization α and the angle between the magnetic field orientation and the beam propagation direction θ. In a first step, evolutionary algorithms (see Section 2.5.4)

name	d	B	α	θ
sample on piezo	$1.8829\,\mu$m	$32.648\,$T	-0.24999π	0.48353π
static sample	$1.9149\,\mu$m	$32.684\,$T	$+0.25195\pi$	0.49809π

Table 5.1: Material properties of ^{57}Fe-samples. d is the thickness, B the internal magnetic hyperfine field, α the angle of magnetization and θ the angle between beam propagation and magnetic field direction. The respective fits are shown in Fig. 5.6.
Note that there is a symmetry in α, such that the sign of α cannot be determined from the single time spectra. From the experimental setup it is known, that the two samples have a relative angle of $\pi/2$. Thus, the relative sign is determined.

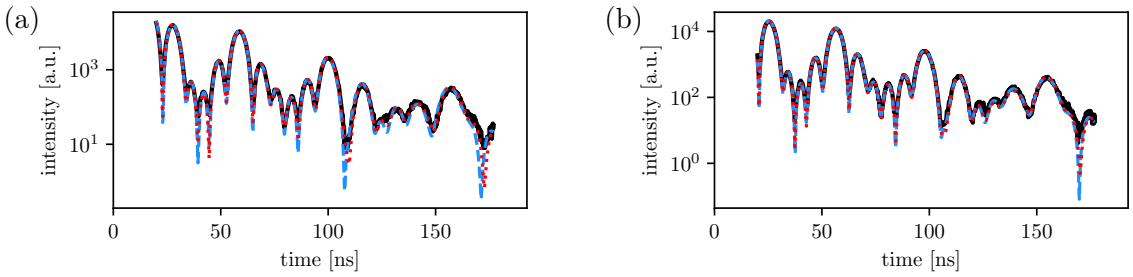

Figure 5.6: The material characterization fits for the sample on piezo (a) and static sample (b). The magnetic field B, α the angle of magnetization within the sample plane and θ the angle between beam and sample plane are fitted to the experimental data (black, solid) with evolutionary algorithms (blue, dashed), which are optimized (red, dotted). Resulting material properties are displayed in Table 5.1.

are used to find the rough global minimum of the comparison function. An optimization of the evolutionary algorithm result with standard fit routines such as Nelder-Mead can be used to find the global minimum.

The material properties of the sample on the piezo and the static sample are displayed in Table 5.1, the corresponding fits to find those properties in Fig. 5.6. The agreement of the fitting results with the measurements can clearly be seen.

5.2.3 Applied voltage patterns

Originally, we planned to apply a "magic waveform" [110].The principal idea is that the ratio between the applied voltage and the resulting motion in frequency space gives the response function of the whole system. Using this received response function, the necessary voltage pattern for special waveforms can be calculated in frequency space and converted into time space by a Fourier transform [110].

Unfortunately, until now the "magic waveform" approach does not work good enough for our purpose here. The problem is that the desired steplike functions (see Section 5.1.3) need many and high frequencies to be represented properly in frequency space. For a truncated frequency space, the function's edges are not sharp

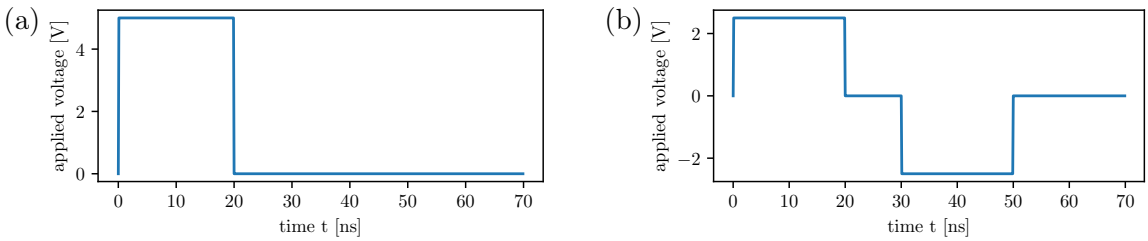

Figure 5.7: The voltage patterns "one20nsJump" (a) and "upDown_20ns_jumps_gap_10ns" (b) applied to the piezo without amplifier. They are started every 40th bunch. For measurements with amplifier if not stated otherwise a peak-to-peak voltage of 1.2 V is used and amplified with 25 dB.

in time space and there are oscillations on the plateau. However, already those oscillations on the zero voltage plateau would disturb the destructive interference. Thus the motion would have no part where there is actually no motion. Not having a static region is a problem, because we want to have results with no motion for comparison to show how well the switching works on the level of single pulses.

Hence, we decided to apply voltage pulses like the ones in Fig. 5.7. There a region with no voltage applied is available. The drawback is that we do not know the exact piezo motion resulting from those voltage patterns because they have not been characterized.

All measurements discussed in this part are collected with a motion that lasts over 40 bunches. That means that in contrast to the motion reconstruction measurements in Chapter 4, where a motion starts every fourth pulse, here a motion is started every 40th pulse. As a result, after the application of the non-zero voltage pulse, which is used for the pulse shaping, as shown in Fig. 5.7a, there are 39 bunches without applied motion, such that the piezo motion can relax. Those long motion sequences also provide access to new investigations such as the relaxation time of the piezo as discussed in Section 6.3.

5.3 Experimental results for pulse shaping

5.3.1 Proof of principle

The clear signature of the experiment is an intensity increase in the perpendicular component ($\hat{\pi}$) after applying a phase shift. This increase can be seen from the $\hat{\pi}$-component with motion in Eq. (5.11) and without motion in Eq. (5.10).

The results of measurements with voltage "one20nsJump" (see Fig. 5.7a) for different delays of the motion, i.e. the voltage pulse starting at different times, are displayed in Fig. 5.8. The signal with motion is about 10 to 60 times stronger than the one without motion in the bunch before. The spectrum in which the instantaneous jump takes place will be called jump in the following, the bunch before that

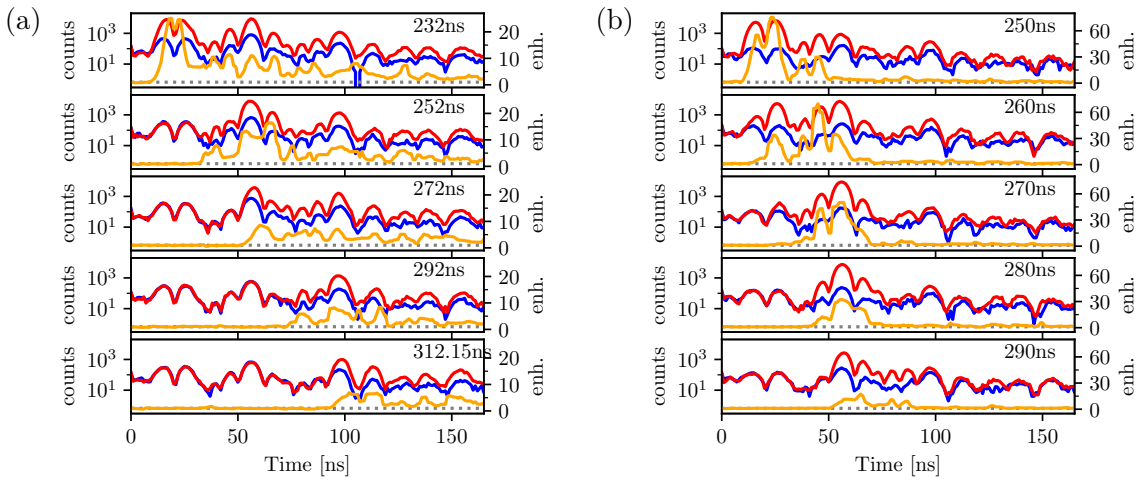

Figure 5.8: A few example time spectra as a proof of principle for the switching result. The spectrum in which motion takes part (red) as well as the one before (blue) are shown for measurement with (a) and without (b) amplifier. In addition, the enhancement, i.e. ratio between spectrum with and without motion is shown (orange). The enhancement is filtered by a median filter of size 5 (more details in main text). The gray dotted line indicates an enhancement of 1. The number in the upper right corner of each panel is the delay, i.e. the time shift of the start of the voltage pulse.

will be referred to as a reference.

We choose the bunch before as a reference instead of a time spectrum measured separately at a different time, where no voltage at all was applied to the piezo, because in future experiments switching light properties should take place from bunch to bunch. As we can see from Fig. 6.3, the separately measured time spectra without any voltage applied and the defined "reference" do not vary qualitatively. From the noise analysis in Chapter 6, we can deduce that the induced motion has decayed sufficiently enough in the 39 bunches until the one before the next voltage pulse is applied. To quantify the difference, the enhancement

$$\text{enhancement} = \frac{\text{jump (spectrum with motion)}}{\text{reference (spectrum without motion)}} \tag{5.20}$$

is defined. The so-defined enhancement slightly follows the curve of the spectrum because of the following reason. Assuming μ = jump without noise/reference without noise to be the actual enhancement and using the signal to noise ration SNR = reference/noise,

the enhancement in Eq. (5.20) is given by

$$\text{enhancement} = \frac{\mu \cdot \text{reference} + \text{noise}}{\text{reference} + \text{noise}} \tag{5.21}$$

$$= \frac{\mu \cdot \text{SNR} + 1}{\text{SNR}} \tag{5.22}$$

$$= \begin{cases} \mu & \text{SNR} \gg 1 \\ 1 & \text{SNR} \ll 1 \end{cases}. \tag{5.23}$$

Thus, the enhancement is only high if the signal is high. We have to keep this in mind for the analysis of the enhancement.

Because small variations on small intensities have a huge effect, the enhancement is smoothed with a median filter of size 5. This filter means that at every time step, the actual value is replaced by the average over five values centered around the particular time.

Without motion, the jump and reference spectra are nearly identical. When the motion starts, the jump spectrum is enhanced by a factor of order of 10. At smaller delays, i.e. the motion starts at earlier times, the enhancement is higher than for greater delays. This effect is visible for the measurements with and without amplifier and is due to the intensity dependency of the enhancement (see Eq. (5.23)).

In addition, we see that the enhancement curves for different delays look very different. Those differences are because the intensities in the enhanced regions are very different.

After the end of the motion, without amplifier the jump spectrum gets back to the level of the reference and has a similar course, while for the measurement with amplifier the jump spectrum is enhanced for a much longer time. In both cases the longer time compared to the voltage pulse width is an artefact of the piezo not following the applied voltage pattern exactly (see Section 4.4) and probably undergoing damped oscillation after the quick changes in the applied voltage because of its inertia. Unfortunately, we do not have a method to extract the exact motion from only time spectra so far.

5.3.2 Delay calibration and different switch on times

As already explained in Section 2.5.2, due to e.g. cable lengths there are several time delays so that time calibrations are necessary. From the enhancement, the starting points of the jump of the motion can be estimated in the measurements with different delays. This estimation is done by searching for the time, at which the enhancement rises above 1 and the rise is steep enough to not be caused by noise fluctuations in the enhancement. For the measurements with amplifier the spectra are shown in Fig. 5.9a. This figure includes more spectra than the ones shown in Fig. 5.8. A systematic error of 3 ns is assumed for the determination of the starting point.

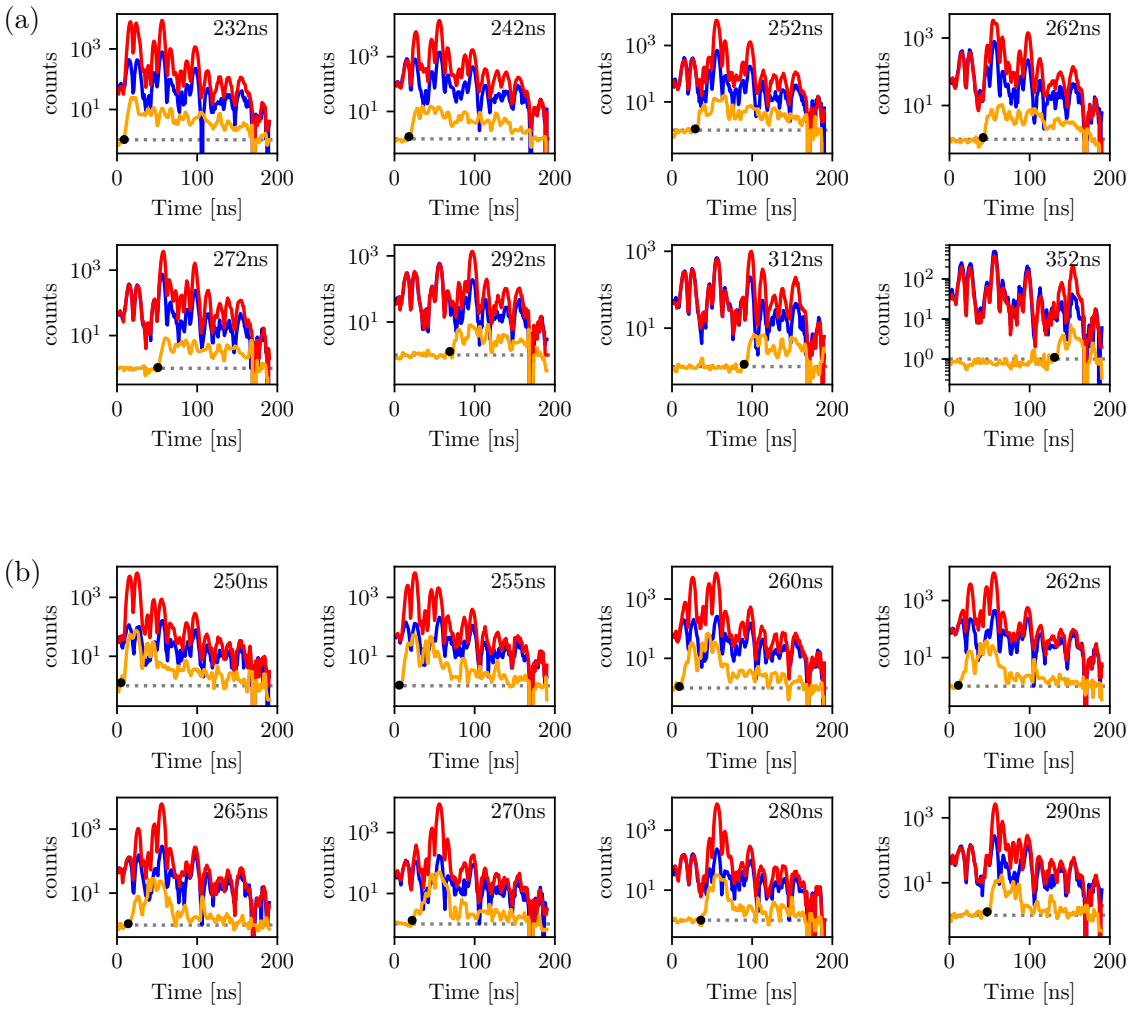

Figure 5.9: The jump (red) and reference spectra (blue) used for the time delay calibration with (a) and without (b) amplifier. In addition, the median filtered enhancement is shown (orange). The black dot indicates the estimated beginning of the motion. Delays of the respective measurements can be found in right upper corner.

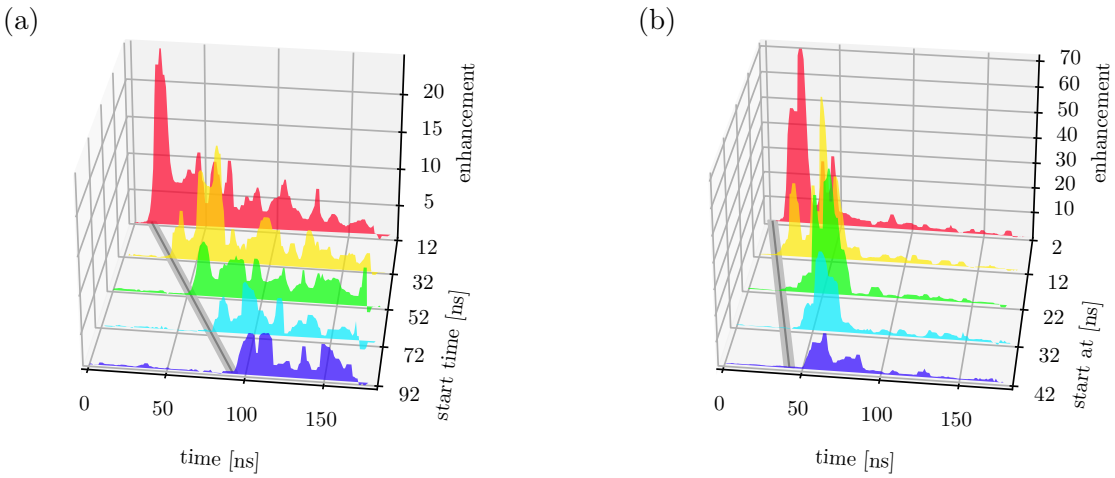

Figure 5.10: The enhancement as a function of time for different delays, i.e. starting times of the motion, shown for measurements with (a) and without (b) amplifier. The gray line indicates the calculated starting time, where the gray rectangle represents the error, with and without amplifier according to Eqs. (5.24) and (5.25), respectively.

Delays are given as the delay with respect to the trigger, that starts the voltage pattern in Fig. 5.7a, as set at the Agilent. The bunch in which the jump takes place is bunch 6 after the trigger. From the estimated starting points for the different delays, we find the starting point for an arbitrary delay, that can be set with the Agilent, measured with amplifier to be

$$t_{\text{start motion}}^{\text{with amplifier}} = (-222 \pm 3)\text{ns} + \text{delay}, \tag{5.24}$$

where the starting point of bunch 6 is at $t = 0$ ns. Negative starting times correspond to motions starting before bunch 6, e.g. in bunch 5. The error is the combined statistical and systematic error.

Similarly, for the results in Fig. 5.9b we find

$$t_{\text{start motion}}^{\text{without amplifier}} = (-248 \pm 4)\text{ns} + \text{delay} \tag{5.25}$$

for data measured without amplifier. The deviation of the time calibration with and without amplifier is caused by different cable lengths and internal delays in the amplifier.

With this delay time calibration in Eqs. (5.24) and (5.25) the starting times of the motion for measurements with different delays, e.g. shown in Fig. 5.8 can be calculated. The enhancement for various delays measured with and without amplifier can be seen in Fig. 5.10. The times on which the enhancement becomes significantly higher than one due to the motion lie on a straight line described by Eqs. (5.24) and (5.25), respectively. The straight lines are expected from time delay calibration. The only small deviations show that the switch on times of the enhancement, i.e. significantly higher intensities, can be chosen reliably.

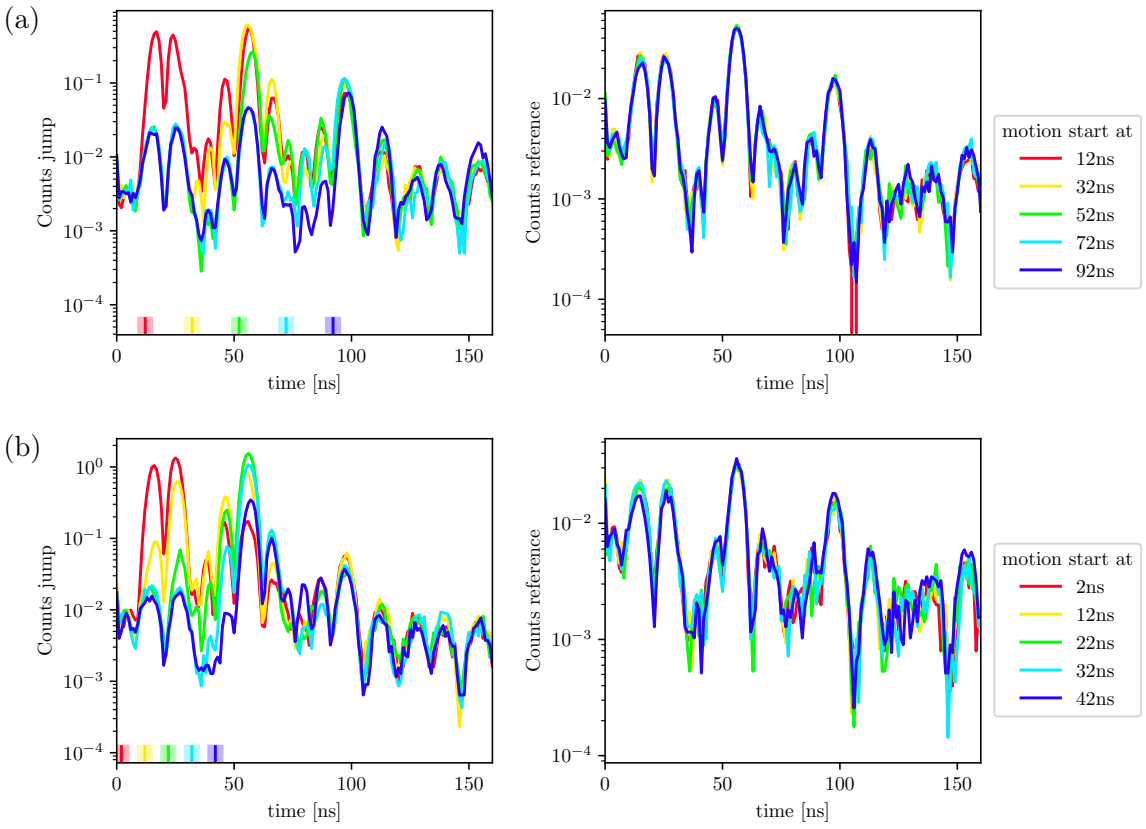

Figure 5.11: Jump (left) and reference (right) spectrum for different delays, i.e. starting times of motion for measurements with (a) and without (b) amplifier. The colored boxes indicate the starting point of the motion with errorbar calculated from Eqs. (5.24) and (5.25) The normalization is chosen so that the integrated reference spectrum is 1.

For the measurements without amplifier (Fig. 5.10b), the enhancement drops back to about 1 roughly 40 ns after the starting time. Thus, in addition to a switching on effect also a switching off effect due to the motion can be seen. The time in which the jump spectrum is significantly enhanced (about 40 ns) is longer than the pulse duration (20 ns) because the piezo motion does not follow the applied voltage pattern exactly as can be seen from the comparison between Figs. 4.8 to 4.10. The reason for the enhancement varying on a higher level behind the pulse than in front of it are probably damped oscillations of the piezo as a response to the rapid voltage changes of the pulse. To understand the shape of the enhancement, the exact piezo motion should be known as finite velocities causing Doppler shifts play a crucial role.

Comparing the jump and reference spectra for different delays gives additional insights. From Fig. 5.11 it can be seen that the references agree very well with each other. That shows that the reference spectrum is independent of the chosen delay. For a perfect instantaneous motion, we would expect that during their respective enhancement time, in which the motion is switched on, the jump spectra for the different delays agree with each other (see Fig. 5.3), which is not the case. The intensity of the quantum beat maxima drops with time. Hence, the noise becomes more and more important in the enhancement as indicated by Eq. (5.23).

For the measurements with amplifier (Fig. 5.11a) the enhancement does not drop back down to a similar level as before the motion started. In those measurements, there is more noise in the reference spectrum as explained in Sections 6.3 and 6.4. In addition, the enhancement during the motion is smaller than in the case without amplifier. Hence, the noise created by the oscillation after the applied pulse becomes more important.

5.3.3 Different voltages

In Fig. 5.12 jump and reference spectra as well as enhancement for different peak-to-peak voltages of the motion in Fig. 5.7a measured with amplifier are shown. The highest enhancements are generated with a peak-to-peak voltage of 1.0 V. Although the enhancements look different, similarities can be found in the spectra. Starting from about 85 ns, the spectra with motion agree with each other for all different peak-to-peak voltages. Between 22 ns, the motion start according to Eq. (5.24), and 85 ns the spectra with motion vary significantly for the different peak-to-peak voltages. Those differences indicate that the controlled motion has dropped significantly after 85 ns and is dominated by the noise motion from the ring down of the system.

The differences in between are caused by different phase jumps. This hypothesis is supported by the fact that 0.8 V and 1.4 V as well as 1.0 V and 1.2 V seem to be very similar. Because there is a roughly linear relation between applied peak-to-peak voltage, we can estimate the phase jumps corresponding to a certain applied voltage from the two motions and their applied voltages in Section 4.4. We find, that 1.0 V and 1.2 V lead to a phase of $\phi \approx \pi$. Hence, we expect them to be similar. For 0.8 V and 1.4 V the phases differ from π by $\delta\phi$, $\phi \approx \pi \pm \delta\phi$. Because $\phi = \pi$ destroys the

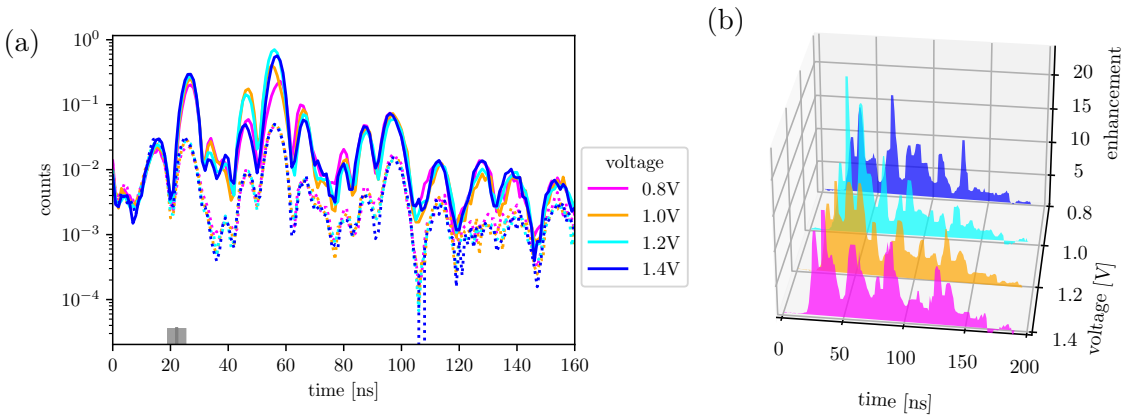

Figure 5.12: Jump (solid) and reference (dashed) spectra (a) as well as corresponding enhancement (b) for different voltages measured with amplifier. The delay is 240 ns so that the motion starts 22 ns after the arrival of the pulse as indicated by gray box in (a), respectively. The shaded box is the errorbar.

destructive interference maximally and the phase influence being symmetric around π (see Eq. (5.12)), we expect the results for 0.8 V and 1.4 V to be similar.

5.3.4 Different jump lengths

We also performed measurements without amplifier for different jump lengths by varying the voltage pulse width. Resulting spectra and enhancement can be seen in Fig. 5.13. The motion starts 13 ns before the pulse arrival. For all measurements a strong enhancement at early times is visible. Interestingly, the enhancements for 20 ns and 60 ns show a second peak that the other do not show. The long pulse (200 ns) shows an enhancement significantly above one for the whole bunch as expected. Unfortunately, the results are hard to interpret if the piezo motion caused by the applied voltage is not known.

5.3.5 Double pulses

After investigating the single pulse enhancement, we wanted to explore if it is possible to create double pulses by applying two voltage pulse. Because the polarization interferometer is operated at minimal intensity motion in forward or backward direction result in the same intensity output (see Eq. (5.12)). The difference of the motion direction can only be seen in the phase, not the intensity. Hence, two voltage pulses being in the same direction or in opposite directions have the equivalent signature in the interferometer. The two jumps are chosen to be in opposite directions due to noise reduction (see Section 6.3). The voltage pattern is shown in Fig. 5.7b and used without amplifier.

The jump spectra and enhancements for different gap widths are displayed in Fig. 5.14. The height of the spectrum peaks at about 60 ns can be highly influenced

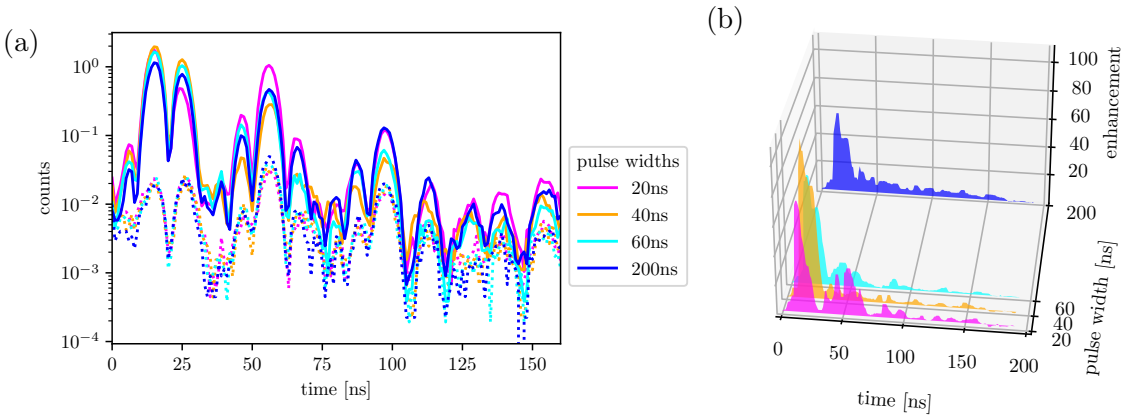

Figure 5.13: Jump (solid) and reference (dashed) spectra (a) as well as corresponding enhancement (b) for different jump lengths measured without amplifier. The delay is 235 ns so that the motion starts 13 ns before the arrival of the pulse.

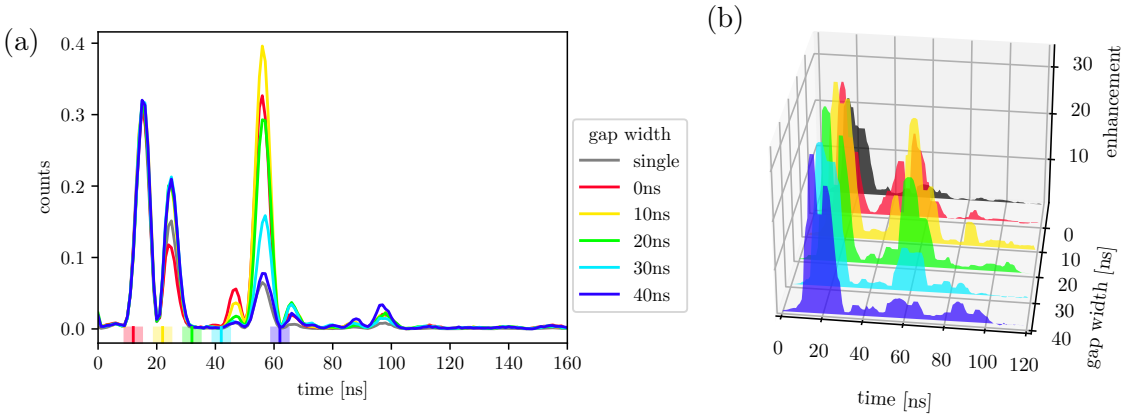

Figure 5.14: Jump spectra (a) and enhancements (b) for motion "up-Down_20ns_jumps_gap_*ns" for different gap widths at delay 240 ns so that the motion starts 8 ns before the arrival of the synchrotron radiation pulse. The dark gray line in (a) and area in (b) shows the jump spectrum and enhancement, respectively, for motion "one20nsJump", i.e. a single pulse, at the same delay. Its enhancement is scaled down by a factor of 5 for better visibility of the other enhancements. Note, that the single pulse measurement also has a different voltage pulse height. The colored boxes indicate the corresponding start of the second pulse calculated from Eq. (5.25) with errorbars. Normalization is chosen, such that counts in the jump spectrum between 0 ns and 15 ns, where in all measurements the same voltage is applied, are the same.

with the gap from being much less than the double peak at about 20 ns to much higher. Different peak heights are probably caused by different displacements and Doppler shifts due to finite rise times. In principle, the peak height is tunable with the displacement and thus the degree of constructive interference. The double peak at about 20 ns is caused by the choice of the delay. Only for the single pulse case and no gap, they differ from the other measurements.

In comparison to the result of "one20nsJump", i.e. only one pulse, the influence of the second pulse can be clearly seen in the enhancement, especially for small gaps. Also changing the gap widths shifts the second enhancement peak accordingly on the right order of timescale. However, the influence of the second pulse is getting lower the longer the gap. This change might be because of the intensity influence on the enhancement as shown in Eq. (5.23). In addition, the voltage pattern does not perfectly convert into a piezo motion of the same shape, such that the gap regions might not be the same in the different motions. The principal form of the first pulse in the enhancement is very similar for all measurements as expected because the first pulse of the voltage pattern stays the same while scanning the gap.

The discussed results are a clear first proof that double peaks could be achievable and tunable with the proposed setup. Nonetheless, still a lot of work needs to be done until controlled double pulses from this setup can be used for experiments.

5.4 Discussion of the experimental results

A first proof of principle analysis in Section 5.3.1 showed that with the polarization interferometer, the sample response can be switched on. The intensity increase at a certain time was further investigated in Section 5.3.2. It could be seen that the measurements without amplifier give a more pulse like structure for the enhancement as expected from the shape of the applied voltage and expected distortions by the amplifier.

Next, the influence of different parameters such as peak-to-peak voltage and voltage pulse widths were examined in Section 5.3.3 and Section 5.3.4, respectively. While the results for different voltages and thus different phase jumps are understood in principle, the results for different widths are discussed, but have not yet been understood.

Finally, in Section 5.3.5 it was demonstrated how double pulses could be created with the polarization interferometer, in principle. However, currently the double pulses are less controlled and less investigated.

The experimental results could probably be better understood if the piezo motion would be known. It might be possible to retrieve at least a first guess from time spectra by using the quantum beat analysis by Schindelmann et al. [108]. More details on this technique are given in Section 4.5.3.

In general, it seems as if the piezo motion without amplifier is closer to the applied voltage than in the setup with amplifier. The better performance could be expected, because the amplifier has a limited bandwidth and does not amplify every frequency

by the same factor. Hence, if the peak-to-peak voltage of 5 V, that can maximally be provided by the Agilent, is sufficient, it might be advantageous to not use the amplifier. With a piezo strain constraint $d_{33} = -33 \times 10^{-2}$ Å/m [123], the 5 V peak-to-peak voltage would be enough if no high peaks are contained in the voltage pattern.

Besides the improvement of the piezo motion, a different way to improve the temporal pulse shaping is noise reduction. The suppression of counts in the reference spectrum is mainly limited by noise, that always causes small movements of the two samples. Thus, even in the reference bunch some motion is present, such that the two samples do not interfere perfectly destructively and some light can pass the setup. The bigger those noise movements of the sample, the more light is detected in case of no motion applied actively. Hence, the switching effect, that can be produced with the controlled motion, is reduced. Those noises will be discussed in more detail in Chapter 6.

Chapter 6

Noise background analysis

The experimental setup of two samples in a row with a relative angle of magnetization α of $\pi/2$ (see Fig. 5.2) can be interpreted as an interferometer with the two arms being represented by the two orthogonal polarization states. The interferometer is explained in more detail in Section 5.1.3. Already small motions of one of the two samples can destroy the interference, such that the whole setup operated in the intensity minimum is very sensitive to background noise and provides a new tool to analyze it.

The background noise will be investigated in this chapter. First, in Section 6.1 the sensitivity of our system to sound waves is analyzed by directing loudspeakers to one of the two samples. Next, the noise in spectra without piezo motion is investigated in Section 6.2. The difference to a calculated static spectrum can be explained with noise motions of the samples. One origin are shock waves traveling through the acrylic glass as we will see in Section 6.3. Afterwards, the evolution of interference throughout a cycle of 40 bunches is analyzed in Section 6.4. The chapter is concluded with a discussion of the results in Section 6.5.

6.1 Morsing

At PETRA III, there is a regular test voice at 2:18am in the laboratories. During a measurement, we noticed that at that time the count rate increased significantly (factor of 3). Our interpretation was that the sound wave likely disturbed the destructive interference.

To demonstrate that it actually was the sound from the loudspeaker, we placed a loudspeaker next to one of the two samples (see Fig. 6.1). Next, we applied sine waves with a frequency of 60 Hz to it. The duration of those pulses can be controlled so that morsing is possible. In Fig. 6.2, the names of the three institutes related to the experiment (Max Planck Institute for Nuclear Physics, Deutsches Elektronen-Synchrotron and Helmholtz Institute Jena) are morsed with the loudspeaker and can be detected as sequences of constructive interference in the polarization interferometer. Hence, the sound waves give a strong signature. Unfortunately, this result means that also all other sounds in the laboratory, e.g. vacuum pumps or the RoentDek box, will disturb the destructive interference. The strength of the noise background will be analyzed in the rest of the chapter.

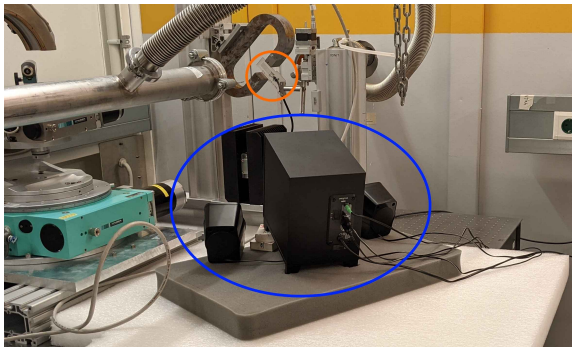

Figure 6.1: The setting of loudspeakers (blue ellipse) directed towards the sample on piezo (orange ellipse). They are placed on foam mats to reduce structure-borne sound so that the sound transmittance via air is dominant. Sine waves of 60 Hz with variable duration are used for morsing. Results are shown in Fig. 6.2. Photo by Jörg Evers.

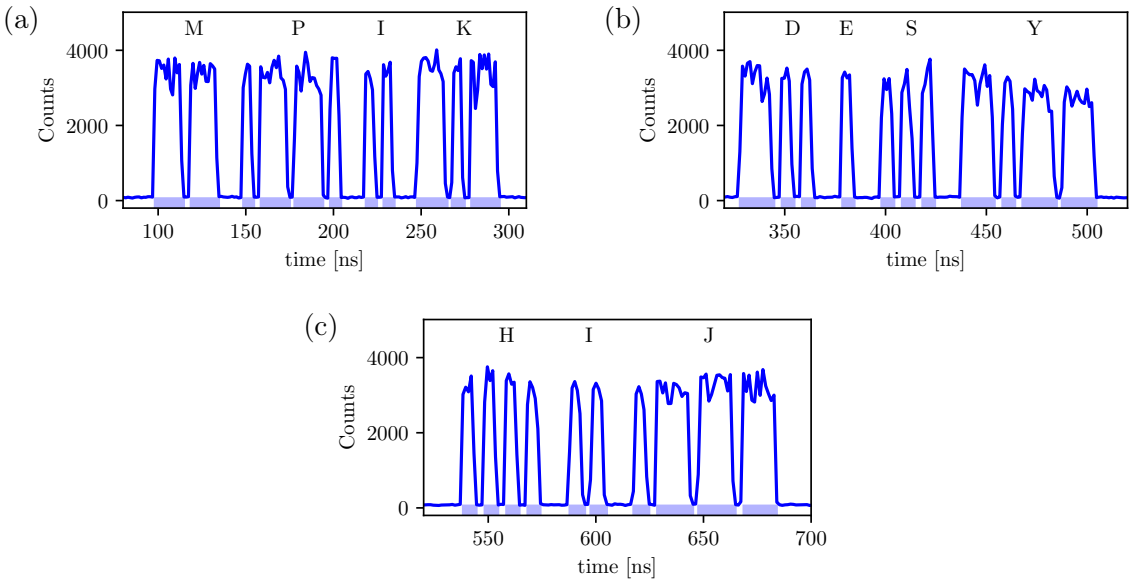

Figure 6.2: Morsing the names of the three big institutes related to the experiment with a 60 Hz sine wave: MPIK (-- ·--· ·· --·), DESY (-·· · ··· -·--), HIJ (···· ·· ·---). The sound waves disturb the destructive interference and show up as strong signatures in the count rate.

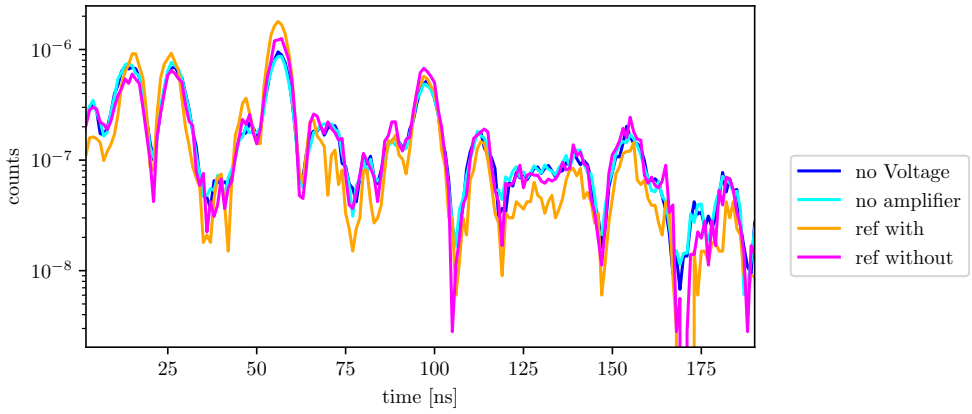

Figure 6.3: Different measured static time spectra are shown: "zero Voltage" (purple), i.e. no voltage applied to piezo, and "no Amplifier" (blue), i.e. amplifier unplugged in addition, are measurements from noise background checks. "ref with [amplifier]" (green) and "ref without [amplifier]" (orange) are example reference ranges as discussed in Section 5.3. The normalization is chosen so that the total number of counts in each spectrum is the same. The drop of intensity at about 170 ns for the two reference spectra with and without amplifier is due to the rising ramp of the reference voltage for bunch identification.

6.2 Noise in static spectra

6.2.1 Different static spectra

In Section 5.3 always the spectrum of the bunch before the one with motion was taken as a static reference spectrum to see how the setup performs from pulse to pulse.

However, more spectra without motion have been measured: time spectra without voltage applied and amplifier unplugged in addition. They are compared to a reference spectrum of the 40 bunch motion sequences measured with and without amplifier in Fig. 6.3. The two separate spectra are nearly identical, which shows that unplugging the amplifier in addition has no big influence. However, it could be that the small variations are not only caused by noise, but by the amplifier electronics. While the reference spectrum without amplifier also agrees with the two separate time spectra apart from minor differences in the peak heights, the reference spectrum measured with amplifier differs significantly from the other spectra. This deviation indicates that in the case without amplifier, in the reference bunch there is nearly no more piezo motion while with amplifier there are small remainings of the motion.

The intensity drops at about 170 ns in the reference spectra with and without amplifier are due to the reference voltage for bunch identification. At its rising edges, events cannot be sorted into the correct bunches properly.

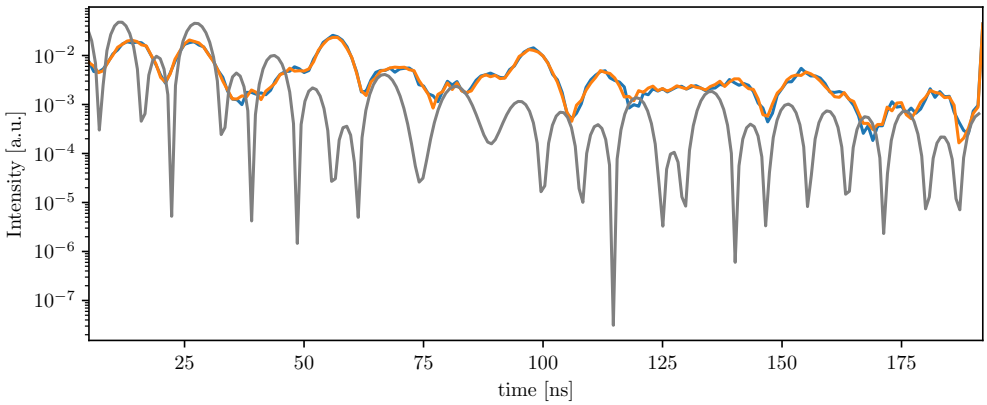

Figure 6.4: The calculated (gray) and measured with no voltage applied (blue) and additionally no amplifier used (orange) static time spectra are shown. The normalization is chosen so that all spectra have the same integrated number of counts.

6.2.2 Noise in static spectra

In Fig. 6.4, some static spectra from Fig. 6.3 are compared to simulated spectra with the material properties given in Table 5.1. There are big qualitative differences between the calculated and measured static spectra. Even if no voltage is applied in the whole measurement, i.e. no motion of the piezo, the system is not static. This observation indicates that there is some noise background that has a big influence on the interference.

6.2.3 Relative detuning caused by noise

In addition to the destruction of interference, any noise motion causes a relative detuning between the two sample because of Doppler shifts proportional to velocity. We assume the noise to have frequencies on a much smaller scale than the one of the decay so that they can be assumed as linear motions over the range of a single decay. The detuning of the target's resonances from each other partially destroys the destructive interference between the two samples.

As explained in the supplement of [41] this random motions can be described by an overall relative detuning. A fit of such a detuning to the measured data is shown in Fig. 6.5a. It can clearly be seen that the calculated spectrum with fitted relative detuning resembles the measured data much better than the one without. The fitted detuning is

$$\Delta_{\mathrm{rel}} = (0.752 \pm 0.10(\mathrm{syst.}) \pm 0.014(\mathrm{stat.}))\,\gamma. \tag{6.1}$$

The systematic error is the fit error, the statistical error from averaging over the two measured spectra without voltage applied to piezo.

In addition, in Fig. 6.5b, not only a single detuning is fitted, but a Gaussian

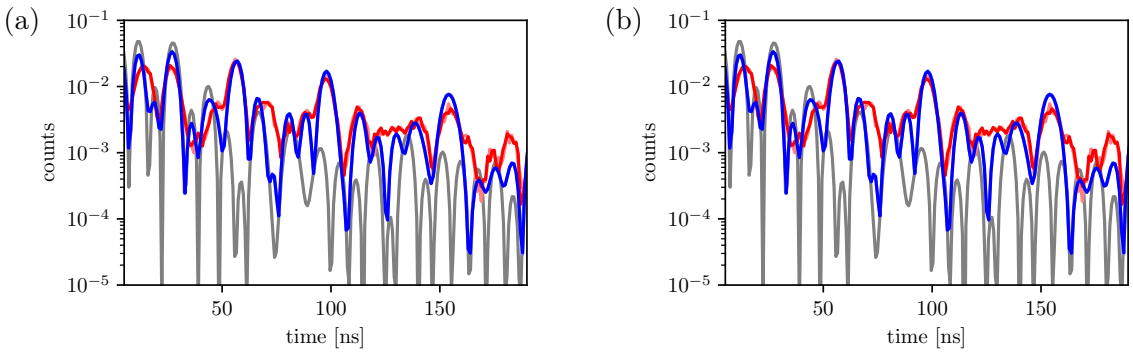

Figure 6.5: The measured static (red), calculated static (gray) and spectrum with fitted detuning (blue) are shown. In (a) a single relative detuning is fitted, in (b) a Gaussian distribution of relative detunings. The light colors correspond to no voltage applied, the strong colors to amplifier unplugged in addition. For the fit a Poissonian metric is used.

distribution of detunings. The result is centered around

$$\Delta_{\text{rel},0} = (3.24 \pm 0.11(\text{stat.})) \cdot 10^{-3}\gamma \tag{6.2}$$

and has a width of

$$\Delta_{\text{rel, width}} = (0.252 \pm 0.005(\text{stat.}))\,\gamma. \tag{6.3}$$

The resulting time spectra are basically identical for a single fitted detuning or a Gaussian distribution of detunings. Hence, for the rest of this chapter, the simpler case of fitting a single detuning with only one fit variable is preferred. This model is also the description used in [41].

6.3 Acoustic waves

6.3.1 Qualitative analysis

In Fig. 6.6 the integrated number of counts and the deviation of the time spectrum from a static reference spectrum per bunch are displayed for different motion patterns and delays. Different peak heights are due to the normalization, which is chosen so that there is one count on average per bunch in every measurement. The motion starts in bunches 5 or 6 depending on the chosen delay. It can clearly be seen that there must be another strong motion about 15 bunches later independent of the delay. For the measurements with amplifier additional peaks can be seen. This motion can be identified as a shock wave, that is created by the initial voltage pulse, traveling through the acrylic glass plate on which the piezo is mounted for stability and hitting the sample on its return. The velocity of this wave is

$$v = \frac{8\,\text{mm}}{15 \cdot 192\,\text{ns}} \approx 2.8 \cdot 10^3 \frac{\text{m}}{\text{s}}, \tag{6.4}$$

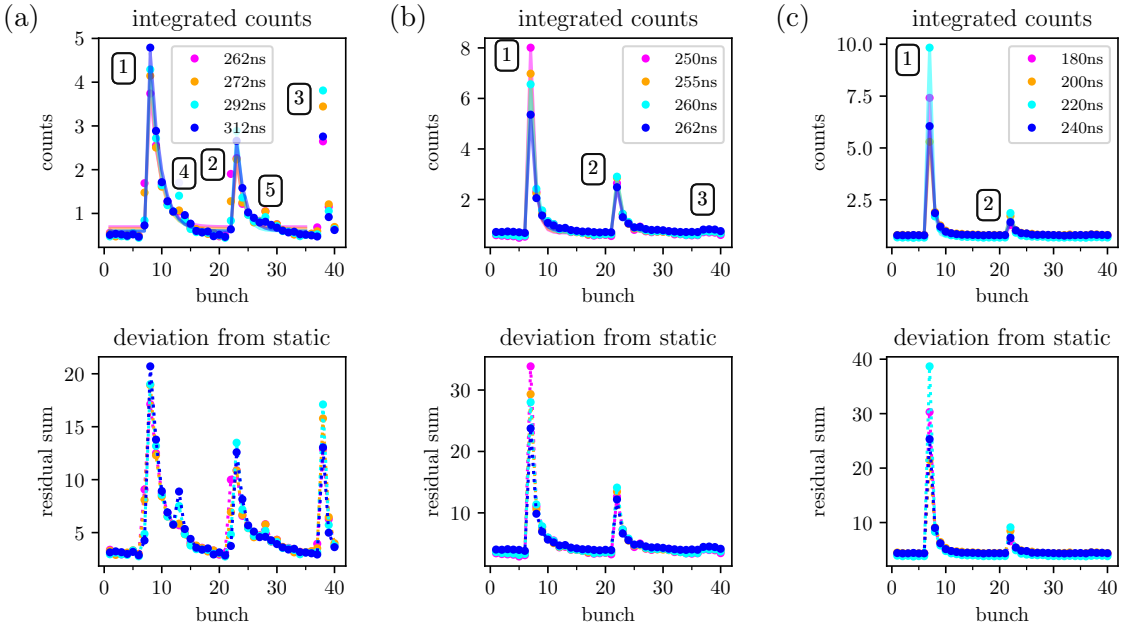

Figure 6.6: The integrated number of counts (top) and deviation from static (bottom) as a function of bunch number for different delays (see legends). The measurements are performed with motion "one20nsJump" with (a) and without (b) amplifier as well as motion "upDown_20ns_jumps" without gap and without amplifier (c). The solid lines show the fits of Eq. (6.5) to the integrated number of counts. For the deviation from static the residual sum in comparison with the measured reference spectrum is calculated, whereby a Poissonian metric is used. Fit results can be found in Table A.1. The normalization is chosen so that the average number of counts per bunch is one in each measurement. The numbers indicate the peaks caused by the revival of the shock wave.

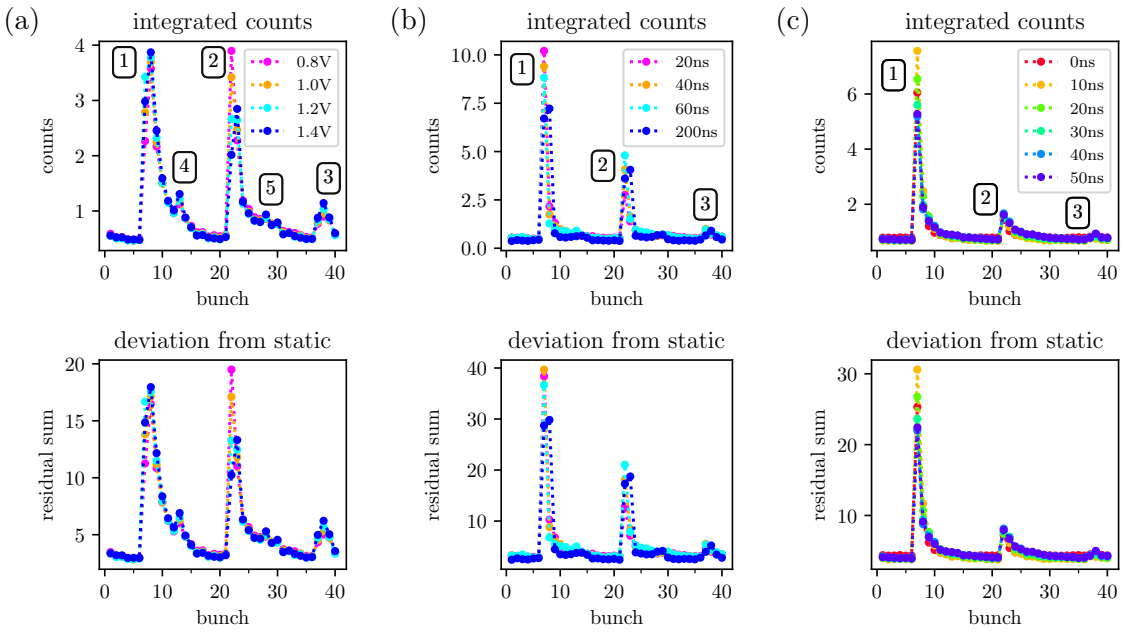

Figure 6.7: The integrated number of counts (top) and deviation from static (bottom) as a function of bunch number. The measurements are performed with motion "one20nsJump" with amplifier for different peak-to-peak voltages (a) and without amplifier for different pulse widths (b) as well as motion "upDown_20ns_jumps" without amplifier for different gaps (c). Definition of derivation from static and normalization are as in Fig. 6.6. The numbers indicate the peaks caused by the revival of the shock wave.

which is close to the speed of sound in PMMA of $2.54 \cdot 10^3 \frac{\mathrm{m}}{\mathrm{s}}$. The effect is reduced in the measurements without amplifier because the applied voltage at the piezo is lower. Therefore, the amplitude of the piezo motion is lower, which creates a smaller shock wave. This smaller shock wave takes less time to be on a same level as the background noise so that the additional peaks nearly vanish completely. The third peak at about bunch 36 can still be identified as a small rise in the number of integrated counts as well as the residual sum for the measurement with "one20nsJump" in (b).

At the position of the fourth peak at about bunch 13, the number of integrated counts and the residual sum slightly rise. This hardly visible change might just be within errors, but could also be a signature of the fourth peak. If the latter is the case, the shock wave has not decayed completely until about bunch 5, which we take as the reference spectrum. Thus, we wanted to reduce the shock wave further. The idea is to counteract the sound wave created by the first voltage pulse with a second sound wave with opposite amplitude by applying a second voltage pulse with the same voltage amplitude, but in the other direction as shown in Fig. 5.7b. From Fig. 6.6c it can be seen that this idea actually decreased the shock wave even more and only one revival of the shock wave leaves a signature.

The principal results are mainly independent of the applied voltage, pulse width and gap width as illustrated in Fig. 6.7. The main features such as a third peak, relative height of second peak and rough decay times are similar to the respective delay scans in Fig. 6.6 with (a) and without amplifier (b) as well as double pulse motion (c). Note that a pulse length of 200 ns stretches out over two bunches. Therefore, in this case the peaks range over two bunches.

6.3.2 Quantitative analysis

To study those shock waves quantitatively, an exponential decay function

$$f(t) = A_1 \exp\left(\frac{t-t_1}{\tau_1}\right)\theta(t-t_1) + A_2 \exp\left(\frac{t-t_2}{\tau_2}\right)\theta(t-t_2) + c \qquad (6.5)$$

is fitted to the first two peaks. Here $\theta(t)$ is the Heaviside-function and the values t_1 and t_2 are fixed to the position of the peaks. Two different decay times $\tau_{1/2}$ are fitted because in the first peak the piezo motion plays a role, while from the second peak onwards shock waves dominate. The resulting fits are displayed in Fig. 6.6 and its parameters can be found in Table A.1.

The mean decay times can be found in Table 6.1. While the mean of τ_1 differs significantly for the measurements ($\tau_1^i - \tau_1^j > 8\sigma$), the mean values of τ_2 agree within their errors ($\tau_2^i - \tau_2^j < 1.8\sigma$). The first decay is mainly governed by the decay of the actual piezo motion. As we have already seen in Section 5.3, with amplifier, the motion of the piezo is much longer than without amplifier. With this knowledge, it is understandable that the decay time is much longer than in the case without amplifier.

measurement	mean τ_1 [ns]	mean τ_2 [ns]
one pulse, with amplifier	1.81 ± 0.12	1.25 ± 0.18
one pulse, without amplifier	0.837 ± 0.020	1.07 ± 0.07
double pulse, without amplifier	0.603 ± 0.008	0.88 ± 0.10

Table 6.1: The mean decay times of the fits of function Eq. (6.5) shown in Fig. 6.6. Single fit results can be found in Table A.1.

The second decay is mainly governed by the motion due to the shock wave return. It seems as if there is still a tendency, that for bigger initial motions probably causing stronger shock waves, the decay time is bigger. Maybe τ_2 depends on the spectrum of the shock wave and spreading occurs. However, within the errors, the decay times do not vary significantly from each other. Because the shock wave in principle is the same in all three measurements, an agreement of the decay times is expected.

6.4 Building up interference over time

We now want to study how the coherence of the two samples evolves over the 40 bunches. To do so, the interference coefficient κ is defined as the prefactor of the interference term in the fit function

$$f_\kappa(t) = |E_1(t)|^2 + |E_2(t)|^2 + \kappa \cdot 2\Re\left[E_1(t)E_2(t)^*\right] \tag{6.6}$$

for two arbitrary electric fields. Here, those two field are the sample responses of the two samples. An interference coefficient of $\kappa = 1$ represents full interference, while $\kappa = 0$ indicates no interference at all. A deviation of κ from one can give a hint on the amount of noise in the setup.

The interference coefficient κ and a relative detuning between the two samples Δ like in Section 6.2.3 are fitted to the time spectrum of each bunch

$$f_{\kappa,\Delta}(t) = |E_1(t)|^2 + |E_2(t)|^2 + \kappa \cdot 2\Re\left[E_1(t)^{i\Delta t}E_2(t)^*\right]. \tag{6.7}$$

Results are shown in Fig. 6.8. For all three measurement types, the applied motion destroys the interference. During the motion decay, the interference builds up again until it reaches its undisturbed value of about one. Even though there is a relative detuning (see Section 6.2.3), the interference is close to one in the static case. The deviation from one indicates the background noise in the setup.

While for the measurements without amplifier the interference builds up again after only a few bunches, for the measurements with amplifier the building up takes until the next motion kick. Similarly, for the measurements without amplifier, most of the time the relative detuning is close to 1γ as in static case (see Eq. (6.2)), while with amplifier this baseline is about 4γ.

The interference coefficient κ varys significantly with the delay at the peaks, while away from the peaks it is very similar for different delays. The reason is that for

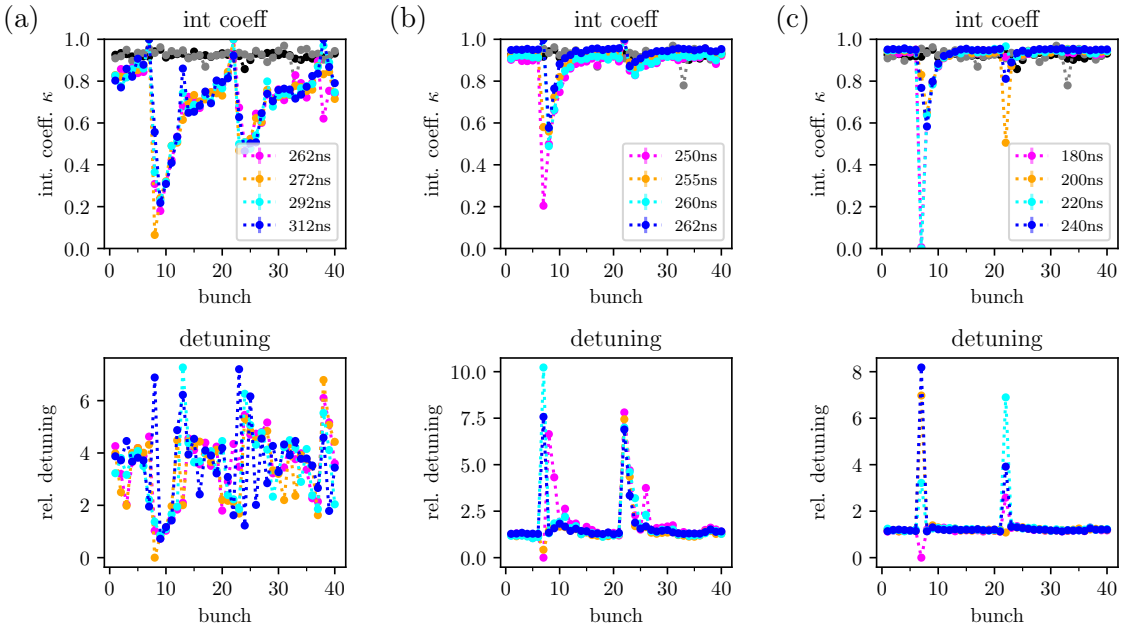

Figure 6.8: The resulting interference coefficient κ (top) and relative detuning between the two samples Δ (bottom) of the combined fit in Eq. (6.7) to the time spectrum in each single bunch. The measurements are performed with motion "one20nsJump" with (a) and without (b) amplifier as well as motion "upDown_20ns_jumps" without gap (c). For comparison, the two static measurements with no voltage applied (gray) and amplifier unplugged in addition (black) are shown. The respective delays are displayed in the legends. Normalization is chosen so that the total number of counts is the same.

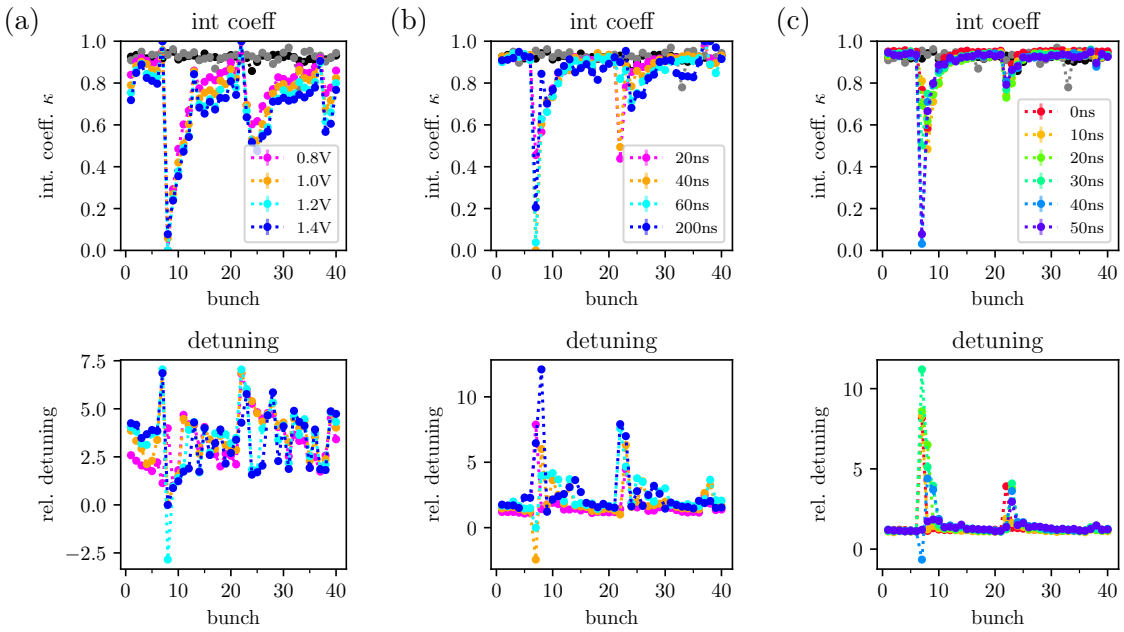

Figure 6.9: The resulting interference coefficient κ (top) and relative detuning between the two samples Δ (bottom) of the combined fit in Eq. (6.7) to the time spectrum in each single bunch. The measurements are performed with motion "one20nsJump" with amplifier for different voltages (a) and without amplifier for different pulse widths (b) as well as motion "upDown_20ns_jumps" without amplifier for different gaps (c). For comparison, the two static measurements with no voltage applied (gray) and amplifier unplugged in addition (black) are shown. The respective delays are displayed in the legends. Normalization is chosen so that the total number of counts is the same.

different delays the time range in which the jump spectrum is enhanced differs, but a fixed interference coefficient κ is fitted for the whole bunch spectrum.

Nonetheless, for the measurements with amplifier and the double-pulse voltage pattern without amplifier, interference coefficients close to zero are achieved. For the single pulse measurement without amplifier, the interference can not be disturbed on a similar level. This observation indicates, that there might be potential for optimization.

Like for the shock waves, the influence of different voltages, different pulse widths and different gap widths is analyzed in Fig. 6.9. For different voltages, the interference coefficient varies. The differences are expected because a lower voltage translates into a smaller motion and thus less disturbance. For the first peak a voltage of 1.2 V leads to the lowest interference. This result is in agreement with results in Fig. 5.12, where a voltage of 1.2 V together with a voltage of 1.0 V lead to the biggest enhancements.

In the plot for different pulse lengths, again the double peaks for the 200 ns long pulse, that stretches out over two bunches, are visible. The other influences of the pulse lengths have not yet been understood. Similarly, the minor differences for different gap widths are not understood currently.

However, in all three plots of Fig. 6.9, there are no qualitative differences for the scanned parameters, which indicates that the setup, i.e. with or without amplifier, and kind of motion, i.e. single or double pulse, has the significant impact.

6.5 Discussion of the results

Because of the operation at minimal intensity, the polarization polarimeter provides a platform to analyze background noise.

In Section 6.1, we saw that sound waves leave a clear signature in the time spectra. Thus, noise can be reduced by placing sound sources, e.g. vacuum pumps or the RoentDek box, far from the samples or even shielding the sample from sound waves.

In Section 6.2, some noise can be modeled by a relative detuning between the two samples. This model can be used to simulate the influence of noise in measurements of the polarization interferometer, e.g. the ones in Chapter 5. In addition, this relative detuning can quantify the amount of noise in the system. Because only fast measurable time spectra need to be measured, the amount of relative detuning between the two samples provides a useful tool to analyze different approaches for noise reduction live in the experiment.

Despite the noise from external sound waves or other vibrations, we have to deal with the shock waves in the acrylic glass plate, that move the sample on its revivals. In Section 6.3, we already showed that measurements without the amplifier at lower voltages can reduce the shock waves. Further reduction is possible with a second voltage pulse in the opposite direction so that two shock waves with opposite amplitudes are created. The reduction of shock waves is especially important if the motion cycles should be reduced to be shorter than 40 bunches. This reduction is

desirable because it increases the count rates in the bunch with motion. Besides the reduction with lower voltages and voltage pattern shaping, a different material instead of acrylic glass could have a positive impact.

Lastly, in Section 6.4 the coherence between the two samples was investigated. For the measurements without amplifier, the interference builds up much faster after being disturbed by the motion than for the ones with amplifier. This result is directly related to the shock waves. The maximally achievable interference is another indicator for the amount of noise.

The noise analyzed in this chapter is universal and does not depend on the polarization interferometer. It also influences the setups for spectral redistribution [65] and coherent control of nuclear excitons [41] as well as future setups. The knowledge gained in this chapter can help to interpret unexpected results and improve the experimental setups to reduce background noise.

Chapter 7

Summary and Outlook

In this chapter, the thesis results are summarized and an outlook on future directions is given.

Summary

The main results of this thesis can be divided into the two topics temporal phase and polarization interferometry. The main goal of the first part was to reconstruct phases (Chapter 3) and motions (Chapter 4). In the second part, experimental results of the polarization interferometry for temporal pulse shaping (Chapter 5) and noise background analysis (Chapter 6) were investigated.

In Chapter 3, we showed that the heterodyne phase reconstruction (HPR) scheme based on temporal phase interferometry and presented by Callens et al. [78] had difficulties to reconstruct the phase of the electric light field close to quantum beats. This is because the oscillation term is dominated by coupling effects between the two samples, that are neglected in [78] for simplicity. We analyzed those couplings and introduced correction terms to HPR in the extended heterodyne phase reconstruction (xHPR). In addition, this improved scheme increases the used data range and thus the statistics for the same amount of measured data. In a beamtime in May 2021, the method developed here was used as a primary analysis tool.

Reconstructing the phase of a measurement with and without motion gives access to the motion as explained in Chapter 4. The performance of our new motion-reconstruction method (HMR) has been analyzed and compared to other techniques. In comparison with the formerly used evolutionary algorithm scheme, it is more efficient regarding measurement time because of longer reconstruction times and regarding evaluation time due to a simpler evaluation procedure. Thus, less measurements are needed and the evaluation is faster. Hence, several motions can be characterized in less time. Therefore, iterative motion optimization as well as usage of several moving samples are feasible with reasonable effort. In addition, the only model assumption needed in HMR is that there is no coupling between the moving sample on a piezo and the analyzer sample on a Mössbauer drive. This approximation is valid if at least four transitions are driven, such that quantum beat minima do not drop to zero, and Mössbauer detunings close to the resonances are excluded. Hence, HMR is an important step on the way to a model free motion characterization. Being successfully tested in live evaluation at a beamtime in May

2021, HRM will probably become the standard method for motion-reconstruction in our experiments (see [41, 65]) and might also be interesting for others whose setups fulfill the discussed requirements.

Not only the detection side of nuclear quantum optics, but also incident light pulse manipulation was considered in this thesis. In Chapter 5, measurements from the first experiment on mechanically-induced refractive index enhancement were analyzed. The central idea is to use the motion-controlled refractive index to manipulate the interference between two samples in a polarization interferometer. Because the output of the polarimeter is directly related to the interference between the two samples, the motion can control the temporal shape of the output pulse. The switching-on process due to the motion is clearly visible in the experimental data. In the measurements without amplifier, also a switching-off effect can be seen, such that single pulses can be created in a controlled way. Different voltages, i.e. different phases between the two samples, agree with the expectations. Furthermore, different voltage pulse widths applied to the piezo are analyzed, but not understood yet. Besides, we found evidence that tunable double pulses can be created with the setup. In contrast to the double pulses created in [41], the intensities can be controlled and in principle also pulse train sequences with more than two pulses are possible. However, the motion and background noise control needs to be improved significantly before temporal pulse shaping would be available for subsequent experiments.

Chapter 6 focused on the noise background in the polarization interferometer. We showed that external sound waves can disturb the destructive interference significantly if emitted close to the sample. Furthermore, a new measurement mode, that collects sequences of 40 pulses instead of formerly used four pulse sequences, is introduced. This new method made the detection of shock waves traveling through the acrylic glass, onto which the piezo is glued, possible in first place. Applying a piezo motion in only one bunch enables a time window of 39 bunches to analyze the decay of the piezo motion. The shock waves leave clear signatures upon their revival. The effect of the shock waves can be reduced by lower voltages at the piezo and the creation of two shock waves with opposite amplitudes. In addition, the evolution of the interference between the two samples is investigated. Depending on the decay of the shock wave, after the controlled disturbance with the piezo motion, the interference builds up faster or slower for shorter and longer shock wave decay times, respectively. Besides the analysis of internal noise like shock waves or external noise, e.g. sound waves, first attempts on modeling the noise have been done. Those attempts allow us to model some noise in theoretical simulations of further experimental schemes.

Summarizing, temporal phase interferometry provides a great toolbox for reconstructing electric field phases and phase-related observables, such as small motions. Polarization interferometry can be used for temporal pulse shaping and the analysis of background noise.

Outlook

The presented results open a number of promising research avenues.

The possibility of reconstructing complex amplitudes of the electric light field has not yet been in used in our data evaluation. Its additional phase information compared to having only access to intensities might improve fitting routines, such as the material characterization.

Although xHPR is already an improvement on HPR, further progress can be made by the inclusion of second order correction terms for more accuracy. Even though the second order correction terms have already been calculated, a simple second order fit model is still an open project. Besides, it might be possible to find less restrictive approximations that still give a simple fit model, but allow regions even closer to the quantum beats. This would improve the fit results by higher statistics because more data from a single measurement can be used in the analysis.

Furthermore, combining xHPR with the method for phase reconstruction by Goerttler et al. [79] might give better results, especially in the case where only two lines are driven and quantum beat minima are important. Truncating the measured data in Fourier space instead of fitting a cosine function at every time step solves the problem with less visibility at quantum beat minima automatically. The Fourier transform would be performable including the correction terms because they do not have any time dependence.

Progress of xHPR/HPR might directly be transferred to the heterodyne motion detection (HMR). Nonetheless, HMR itself improves the motion reconstruction and opens up new possibilities. The advantage of longer reconstruction times in HMR can be used to reduce the measurement time because fewer delay measurements are needed. The resulting measurement time reduction allows us to optimize our motions with the "magic-waveform" approach [110]: From a comparison between the applied voltage pattern and the resulting motion, the response function of the whole system to the voltage signal can be calculated. The inverse of the system response function gives the necessary voltage for a desired motion. This had previously been tried at beamtimes in 2019 and 2021 without HMR and seems to be promising. The new possibility of reconstructing more motions with less measurement time using HMR significantly improves the method by allowing us to perform several iterations of the "magic-waveform" approach to optimize the results. The possibility of creating arbitrary piezo motions would be the next step in piezo-controlled schemes. Not only can step-functions be optimized, but also arbitrary motions are the key to temporal pulse shaping.

In addition, we would like to analyze the stability of the "magic waveform" approach with respect to small variations. As we have seen in Section 4.4, different reconstruction methods result in slightly different version of the motions. Thus it is unclear, which reconstruction version is closest to the actual motion. Using different motions in the "magic waveform" approach might result in different voltage patterns. If the variations from the different motion versions are significant, a measure to estimate the deviation of a reconstructed motion from the actual motion has to be

found.

In particular, such optimized motions could be the key to arbitrary pulse generation. In the evaluated experimental data, we showed that temporal pulse shaping is possible in principle. However, the motions realized in the first experiment are far from optimum. Thus the control and visibility of the shaped pulses should increase with optimized motions. First approaches to achieve that with only one iteration of the "magic-waveform" approach did not seem to give better motions, but iterative usage might be the key here if it improves the resulting motions. The principal limit of pulse shaping is given by the finite rise times of the piezo. Despite optimizing the motion, a faster piezo could give the desired sharper edges.

The other possibility to increase the visibility of the shaped pulses is to decrease the background noise in the reference spectra. Here, Chapter 6 gave us interesting insights on what the noise background looks like and how this noise can be reduced. Some noise reduction aproaches might even be measurable in the laboratory without synchrotron radiation. For example, the shock waves should be visible, when scanning the mechanical resonances of the piezo glued onto the acrylic glass plate.

Although some properties depend on used materials, e.g. the shock waves on the thickness of the acrylic glass plate, the noise in general is not setup specific and is most probably also present in other measurements like the ones on spectral redistribution [65] and coherent control of nuclear excitons [41, 110]. Analyzing the noise with an Allan deviation method introduced in [41, 110] in the context of nuclear scattering might give additional insights. The polarization interferometer operates at the intensity minimum, while the setups in [41, 110] do not. Hence, contributions of uncontrolled motions in forwards and backwards direction, that might cancel each other away from the minimum, might leave signatures in the Allan deviation in the polarization interferometer.

In addition, the polarization interferometer can be used to detect the presence of sub-Ångstrom motions on times scales, that are large enough so that significantly more photons are detected in the case with motion than in the static case. This is for sure the case for motions on the tens of ms level, but might also be possible for faster motions. The signature would be similar to the one of morsing in Section 6.1.

Besides the polarization interferometer as the first experiment carried out in the context of mechanically-induced index enhancement [94, 95], experimental schemes to measure polarization conversion from linear to circular, which we also proposed in this context, have to be developed further. From calculated frequency spectra we already saw, that in the polarization interferometer setup the second, static sample could work as a circular polarization filter. This configuration would imprint signatures on the frequency spectra measured with different angles between polarizer and analyzer. Further investigation on this project is needed before an experimental setup can be proposed.

In conclusion, there are various interesting ideas based on the work presented in this thesis, both on phase and motion reconstruction as well as the polarization interferometry setup. Controllable piezo-motion is already a widely-used technique. Thus, many experimental schemes would benefit from improvements in this direc-

tion. In contrast, the polarization setup and mechanically-induced refractive index enhancement in general are rather new schemes. They seem to be promising for light polarization, such as temporal pulse shaping as well as polarization control. Their principle applicability is not restricted to nuclear quantum optics, such that the whole field of x-ray quantum optics and even optical quantum optics could benefit from it.

Acknowledgements

I would like to thank the Max Planck Institute for Nuclear Physics, especially the division of Christoph Keitel, for providing me a valuable research environment for this thesis, including the beamtime at DESY in Hamburg.

In particular, I am grateful to my supervisor Jörg Evers for giving me enough freedom to follow my own ideas while still guiding me through the project to protect me from running into dead ends. I really enjoyed the beamtime and appreciate the responsibility you put in my hands. In this context, I would also like to thank everyone who made the beamtime possible in those difficult times. Special thanks go to René Steinbrügge, Olaf Leupold and Ilya Sergeev from the beamline as well as Dominik Lentrodt, Jörg Evers, Kai Schulze and Lars Bocklage.

Besides the beamtime, I enjoyed the joint lunch breaks and discussions, online and in person, with my colleagues Dominik Lentrodt, Lukas Wolff, Pim van den Heuvel and Oliver Diekmann. Let me also thank Dominik Lentrodt, Lukas Wolff, Oliver Diekmann and Ruth Winter for proofreading this thesis. In addition, I would like to thank Thomas Pfeifer for being interested in my research projects and volunteering to be the second corrector of my thesis.

Ein weiterer Dank geht an meine Freunde, die mir auch in diesen ungewöhnlichen Zeiten viel Spaß und Freude außerhalb der Physik bereitet haben.

Zu guter Letzt möchte ich meiner Familie danken. Ihr habt mir nicht nur die Möglichkeit zu einem einmaligen Auslandsaufenthalt in London gegeben, sondern vor allem auch in schwierigen Zeiten immer wieder gezeigt, was Zusammenhalt und füreinander da zu sein bedeutet. Vielen Dank für Eure vielfältige Unterstützung während des gesamten Studiums!

Appendix A

Additional material

A.1 Motion reconstruction

Reconstructed versus calculated static phase. A comparison between the motion results with static phase reconstructed with Callens scheme or calculated from material properties is shown in Fig. A.1 for only linear lines driven and Fig. A.2 for all lines driven. Like for the example plots in Fig. 4.2, the two motions in each panel agree within their errors. Thus, the choice of how the static motion is received does not influence the reconstructed motion.

Additional figures for linear lines. For completeness, additional figures for only the linear lines driven corresponding to the respective figures with all lines driven in the main text are shown in this paragraph. The corresponding figures for all lines driven can be found in the referenced sections of the main text.

The pure HMR results of all motion parts as discussed Section 4.2 are shown in Fig. A.3. The parts agree within the overlapping regions.

A comparison between the pure results and optimized splines as in Section 4.3 can be found in Fig. A.4. Due to the smaller reconstruction times compared to all lines driven, less support points are needed. For most motion parts $N = 4$ points are enough. However, like for all lines driven a few motion parts need a higher number of support points (here $N = 8$). Using even more points, $N = 10$, does not change the results significantly.

The agreement between the reconstruction motion parts with Callens scheme and evolutionary algorithms as discussed Section 4.5.1 is shown in Fig. A.5.

A.2 Noise

The fit results of the decay time fits in Section 6.3 are shown in Table A.1.

	delay	A_1	A_2	c	τ_1	τ_2	t_1 (fixed)	t_2 (fixed)
(a)	262ns	5.245	3.658	0.695	1.860 ± 0.359	1.149 ± 0.522	7.0	22.0
	272ns	6.305	3.37	0.659	1.660 ± 0.213	1.3 ± 0.4	7.0	22.0
	292ns	6.267	5.623	0.601	1.844 ± 0.155	1.088 ± 0.178	7.0	22.0
	312ns	7.001	4.008	0.594	1.857 ± 0.156	1.473 ± 0.267	7.0	22.0
(b)	250ns	27.927	4.577	0.671	0.745 ± 0.040	1.167 ± 0.191	6.0	21.0
	255ns	22.119	5.673	0.694	0.791 ± 0.035	1.029 ± 0.117	6.0	21.0
	260ns	16.91	5.402	0.687	0.937 ± 0.045	1.103 ± 0.133	6.0	21.0
	262ns	14.285	4.625	0.763	0.876 ± 0.038	0.999 ± 0.108	6.0	21.0
(c)	180ns	42.117	1.172	0.784	0.541 ± 0.018	1.168 ± 0.328	6.0	21.0
	200ns	16.8	3.371	0.818	0.755 ± 0.019	0.753 ± 0.096	6.0	21.0
	220ns	78.598	6.126	0.71	0.464 ± 0.014	0.598 ± 0.107	6.0	21.0
	240ns	24.186	1.638	0.809	0.653 ± 0.015	1.013 ± 0.159	6.0	21.0

Table A.1: The fit results of fitting Eq. (6.5) as shown in Fig. 6.6. Results are given for different delays of motions (a) "one20nsJump" with amplifier, (b) "one20nsJump" without amplifier, (c) "upDown_20ns_jumps" without amplifier. Errors are the standard variation of the fitting result and are only given for the decay times $\tau_{1/2}$ because we are mainly interested in those parameters.

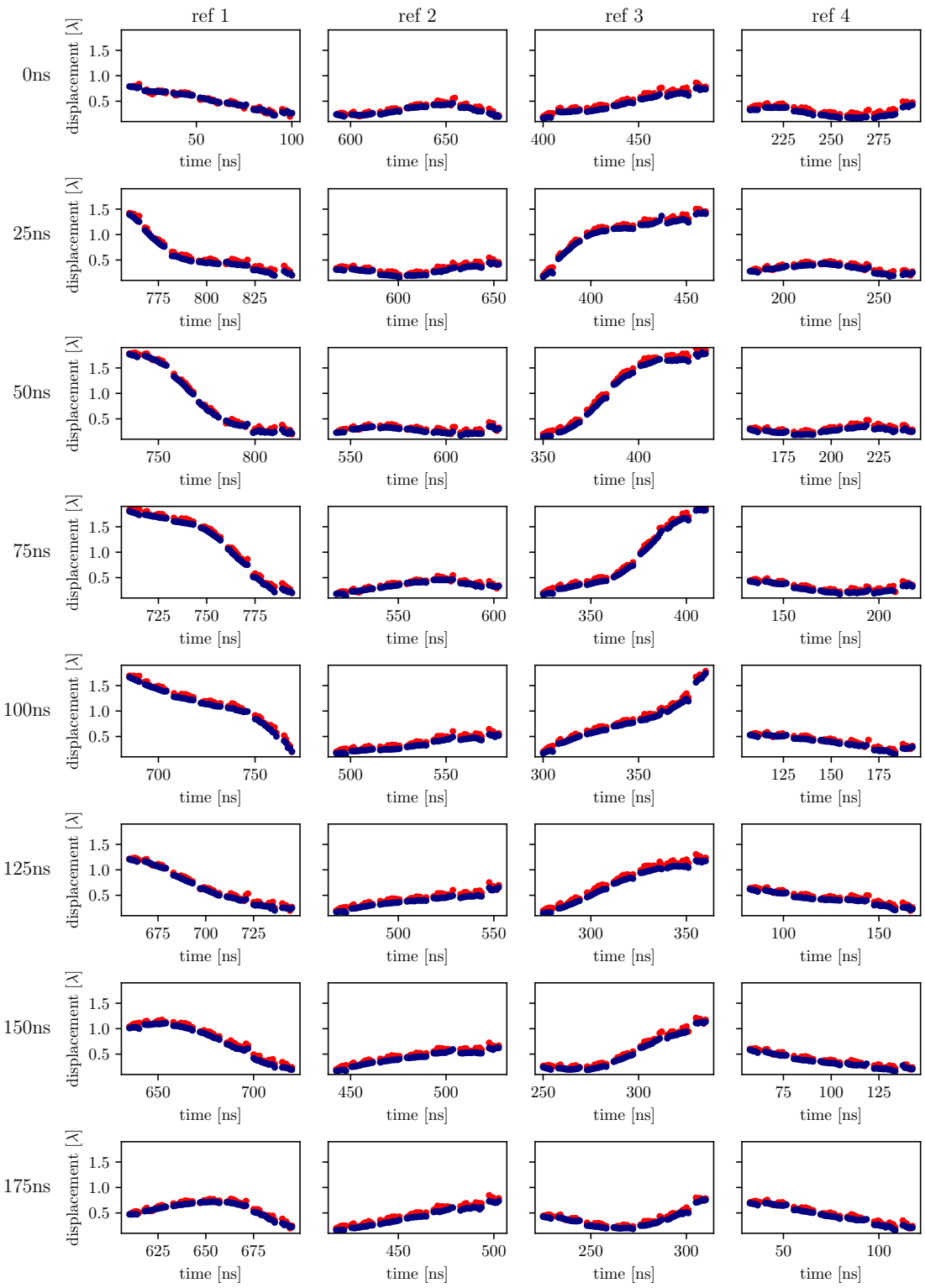

Figure A.1: Comparison of static phase being reconstructed with xHPR (red) and calculated from material properties (blue) for all motion parts of motion "ramp2019". This is measured with only the two linear lines being driven. Excluded points are not shown.

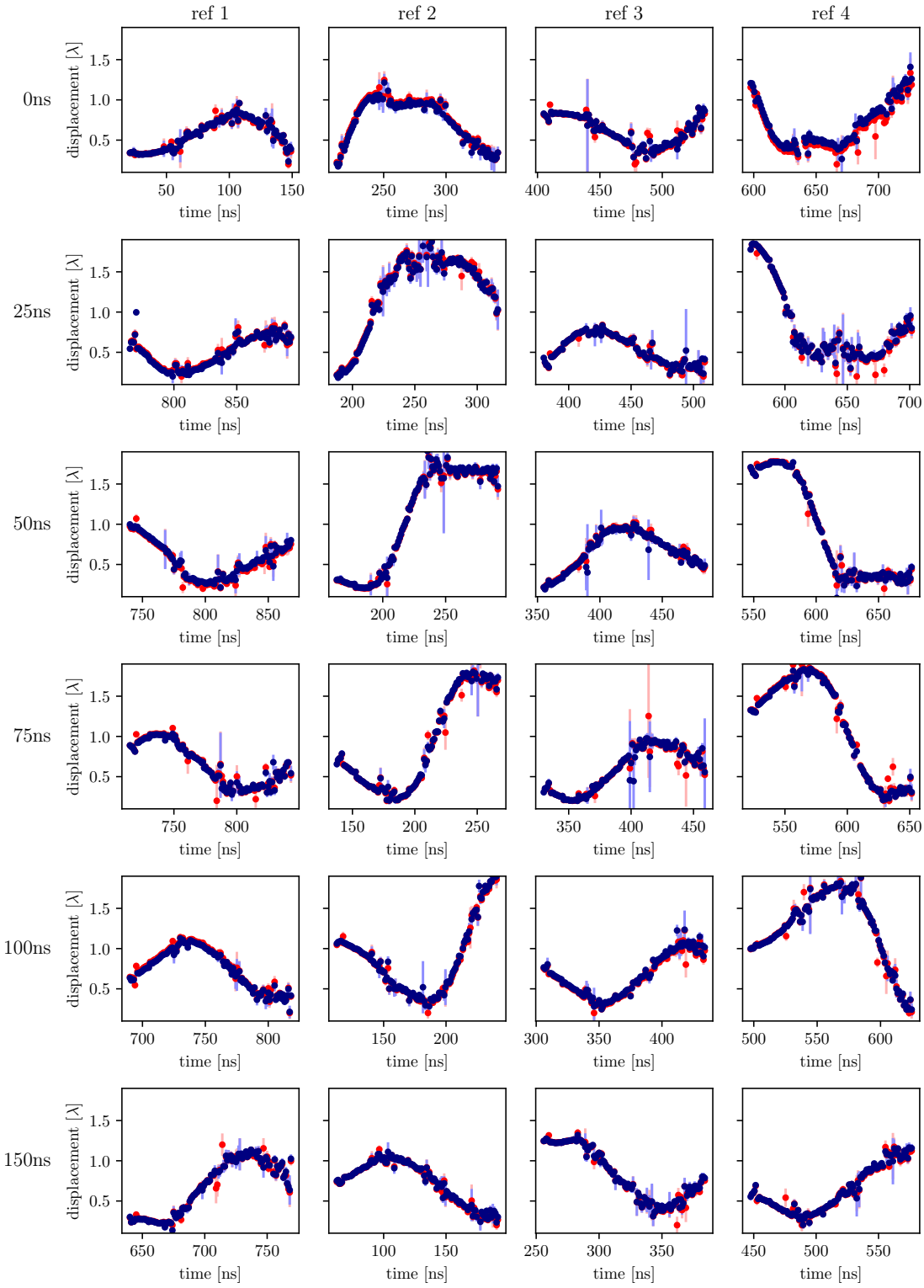

Figure A.2: Comparison of static phase being reconstructed with xHPR (red) and calculated from material properties (blue) for all motion parts of motion "magic2021". This is measured with all six lines being driven. Excluded points are not shown.

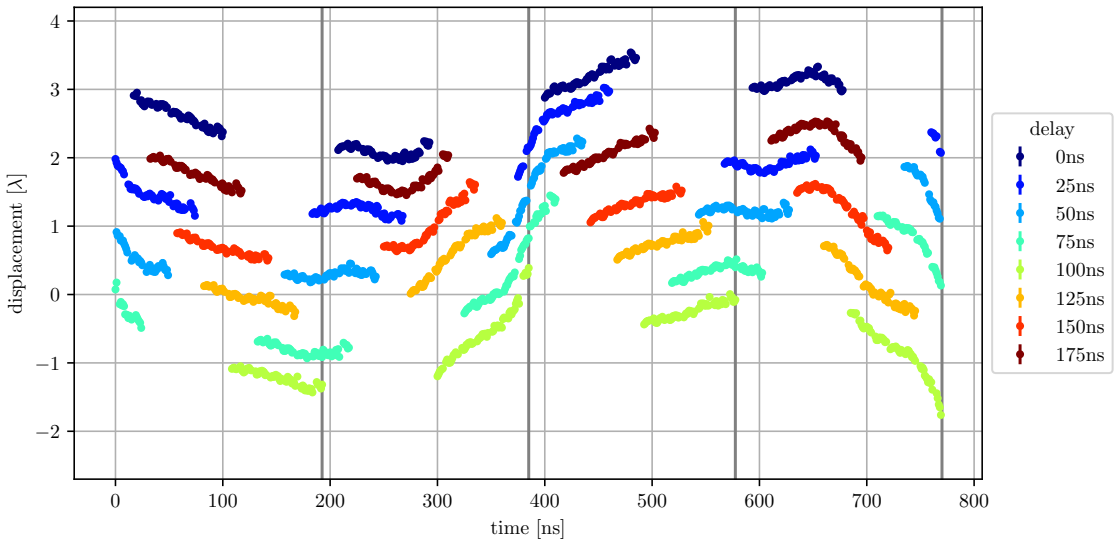

Figure A.3: All reconstructed motion parts for "ramp2019" measured with with only the two lines driven. The colors correspond to the different delays as indicated by the legend. Displacement offsets of the motion parts are arbitrary as discussed in Section 2.3.1 (more detail in main text). The motions parts agree within the errors. Excluded values are not shown for clarity. The gray vertical lines indicate the arrival of a synchrotron pulse for a delay of 0 ns.

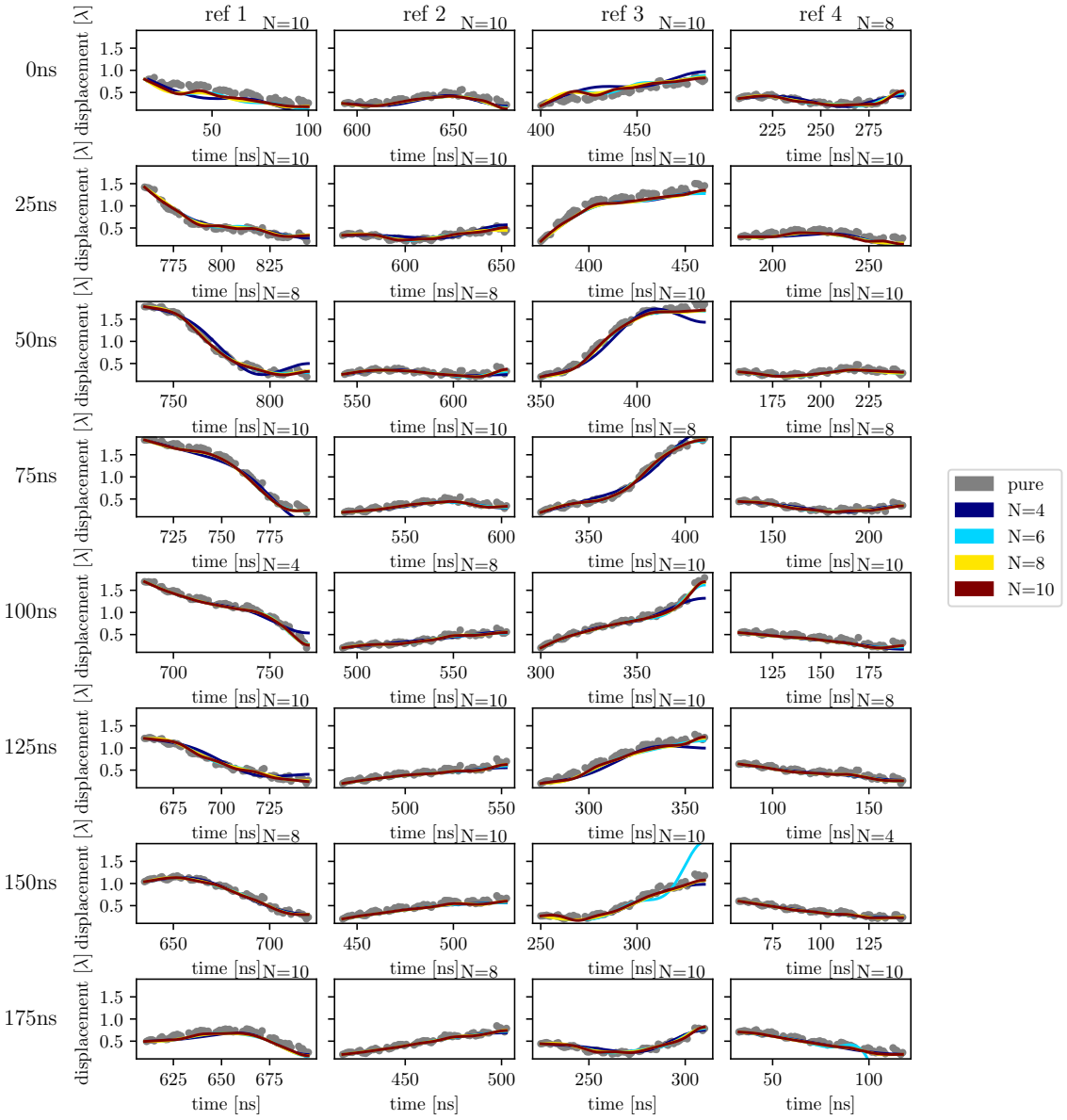

Figure A.4: The pure HMR data (gray dots) as well as the optimized splines for several numbers of support points N (solid lines) are shown for the different motion parts of motion "ramp2019", which is reconstructed with only the two linear lines driven. The N that fits the pure data best is printed in the respective right upper corner. For most panels, the optimized splines for different numbers of support points look rather similar. However, there are some for which a high number of support points ($N \geq 8$) is needed to represent the motion part properly.

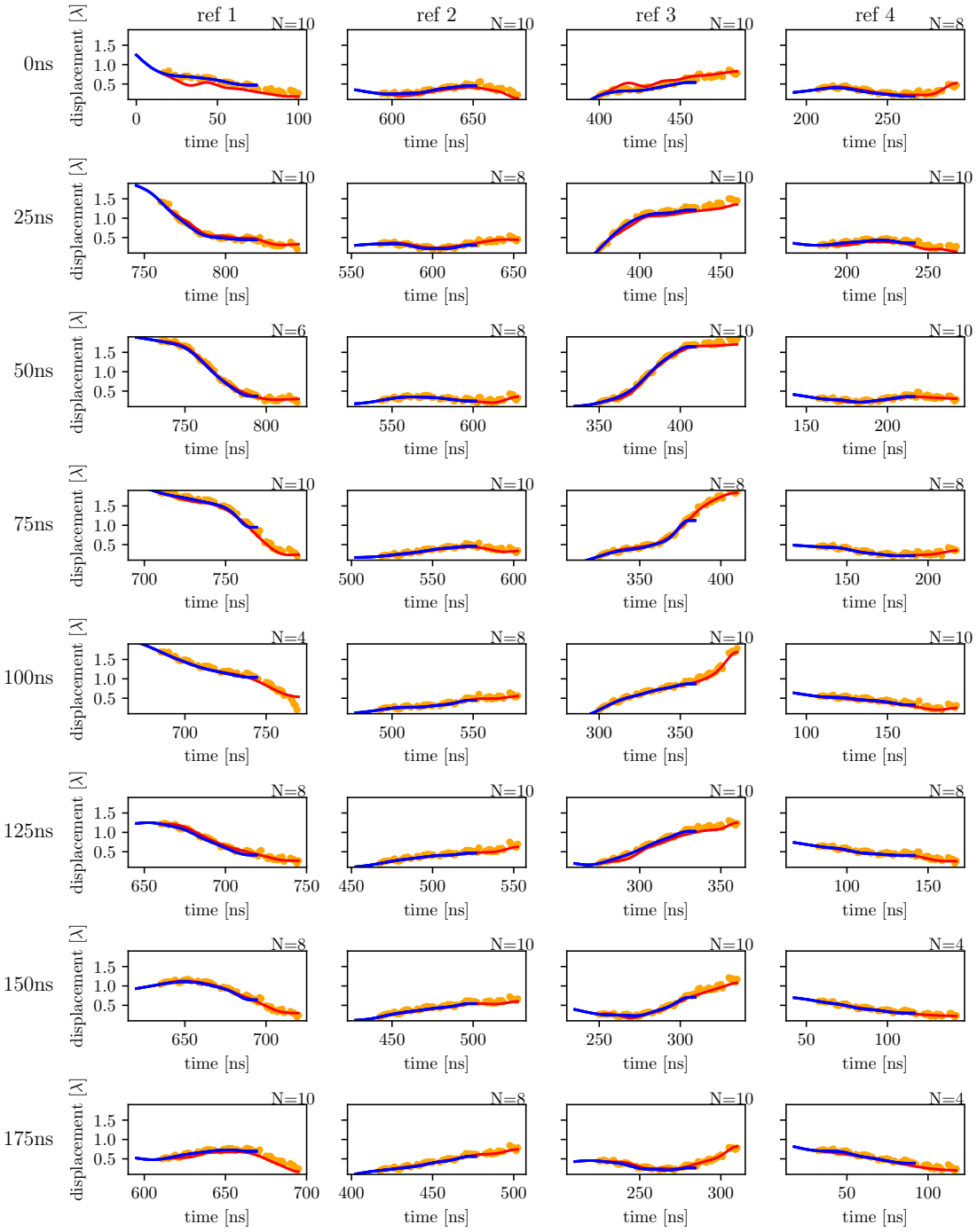

Figure A.5: The pure HRM data from Fig. A.3 (orange), the optimized spline (red) and the optimized result from evolutionary algorithms (blue) are shown for the different histograms from which they are extracted. The plotted optimized spline with support number N as indicated in the right upper corner is the one with lowest deviation from pure HMR data. For a comparison of different support number see Fig. A.4).

Bibliography

[1] B. W. Adams et al. "X-ray quantum optics". In: *Journal of Modern Optics* 60.1 (2013), pages 2–21. DOI: 10.1080/09500340.2012.752113.

[2] W. C. Röntgen. "Uber eine neue Art von Strahlen". In: *Annalen der Physik* 300.1 (1898), pages 1–11.

[3] R. F. Mould. *A century of X-rays and radioactivity in medicine: with emphasis on photographic records of the early years*. CRC Press, 1993. ISBN: 9780750302241.

[4] W. T. Astbury and F. O. Bell. "Some recent developments in the X-ray study of proteins and related structures". In: *Cold Spring Harbor Symposia on Quantitative Biology*. Volume 6. Cold Spring Harbor Laboratory Press. 1938, pages 109–121. DOI: 10.1101/SQB.1938.006.01.013.

[5] J. D. Watson and F. H. Crick. "Molecular structure of nucleic acids: a structure for deoxyribose nucleic acid". In: *Nature* 171.4356 (1953), pages 737–738. DOI: 10.1038/171737a0.

[6] D. Sayre and H. N. Chapman. "X-ray microscopy". In: *Acta Crystallographica Section A* 51.3 (May 1995), pages 237–252. DOI: 10.1107/S0108767394011803.

[7] H. N. Chapman et al. "Femtosecond X-ray protein nanocrystallography". In: *Nature* 470.7332 (2011), pages 73–77. DOI: 10.1038/nature09750.

[8] L. Zhang et al. "Crystal structure of SARS-CoV-2 main protease provides a basis for design of improved α-ketoamide inhibitors". In: *Science* 368.6489 (2020), pages 409–412. DOI: 10.1126/science.abb3405.

[9] C. Kittel and P. McEuen. *Introduction to solid state physics*. Volume 9. Wiley New Jersey, 2018. ISBN: 978-1-119-45416-8.

[10] K. J. Gaffney and H. N. Chapman. "Imaging Atomic Structure and Dynamics with Ultrafast X-ray Scattering". In: *Science* 316.5830 (2007), pages 1444–1448. DOI: 10.1126/science.1135923.

[11] W. H. Bragg and W. L. Bragg. "The reflection of X-rays by crystals". In: *Proceedings of the Royal Society of London. Series A, Containing Papers of a Mathematical and Physical Character* 88.605 (1913), pages 428–438. DOI: 10.1098/rspa.1913.0040.

[12] L. Dubrovinsky et al. "The most incompressible metal osmium at static pressures above 750 gigapascals". In: *Nature* 525.7568 (2015), pages 226–229. DOI: 10.1038/nature14681.

[13] M. Le Tacon et al. "Two energy scales and two distinct quasiparticle dynamics in the superconducting state of underdoped cuprates". In: *Nature Physics* 2.8 (2006), pages 537–543. DOI: 10.1038/nphys362.

[14] J. Als-Nielsen and D. McMorrow. *Elements of Modern X-ray Physics, 2011*. Volume 61. 2011. DOI: 10.1002/9781119998365.

[15] T. Maiman. "Stimulated Optical Radiation in Ruby". In: *Nature* 187.4736 (1960), pages 493–494. DOI: 10.1038/187493a0.

[16] J. M. Raimond, M. Brune, and S. Haroche. "Manipulating quantum entanglement with atoms and photons in a cavity". In: *Rev. Mod. Phys.* 73 (3 Aug. 2001), pages 565–582. DOI: 10.1103/RevModPhys.73.565.

[17] D. Leibfried et al. "Quantum dynamics of single trapped ions". In: *Rev. Mod. Phys.* 75 (1 Mar. 2003), pages 281–324. DOI: 10.1103/RevModPhys.75.281.

[18] A. D. Ludlow et al. "Optical atomic clocks". In: *Rev. Mod. Phys.* 87 (2 June 2015), pages 637–701. DOI: 10.1103/RevModPhys.87.637.

[19] M. Brune et al. "Quantum Rabi Oscillation: A Direct Test of Field Quantization in a Cavity". In: *Phys. Rev. Lett.* 76 (11 Mar. 1996), pages 1800–1803. DOI: 10.1103/PhysRevLett.76.1800.

[20] C. Monroe et al. "A "Schrödinger Cat" Superposition State of an Atom". In: *Science* 272.5265 (1996), pages 1131–1136. DOI: 10.1126/science.272.5265.1131.

[21] H. Häffner, C. Roos, and R. Blatt. "Quantum computing with trapped ions". In: *Physics Reports* 469.4 (2008), pages 155–203. ISSN: 0370-1573. DOI: 10.1016/j.physrep.2008.09.003.

[22] D. E. Browne and T. Rudolph. "Resource-Efficient Linear Optical Quantum Computation". In: *Phys. Rev. Lett.* 95 (1 June 2005), page 010501. DOI: 10.1103/PhysRevLett.95.010501.

[23] W. D. Phillips and H. J. Metcalf. "Cooling and trapping atoms". In: *Scientific American* 256.3 (1987), pages 50–57. URL: https://www.jstor.org/stable/24979340.

[24] C. N. Cohen-Tannoudji and W. D. Phillips. "New mechanisms for laser cooling". In: *Phys. Today* 43.10 (1990), pages 33–40. DOI: 10.1063/1.881239.

[25] S. Chu. "Laser trapping of neutral particles". In: *Scientific American* 266.2 (1992), pages 70–77. URL: http://www.jstor.org/stable/24938942.

[26] A. Ashkin et al. "Observation of a single-beam gradient force optical trap for dielectric particles". In: *Opt. Lett.* 11.5 (May 1986), pages 288–290. DOI: 10.1364/OL.11.000288.

[27] B. P. Abbott et al. "Observation of Gravitational Waves from a Binary Black Hole Merger". In: *Phys. Rev. Lett.* 116 (6 Feb. 2016), page 061102. DOI: 10.1103/PhysRevLett.116.061102.

[28] S. Ruby. "Mössbauer experiments without conventional sources". In: *Le Journal de Physique Colloques* 35.C6 (1974), pages C6–209. DOI: 10.1051/jphyscol:1974623.

[29] R. Röhlsberger and J. Evers. "Quantum Optical Phenomena in Nuclear Resonant Scattering". In: *Modern Mössbauer Spectroscopy: New Challenges Based on Cutting-Edge Techniques*. Edited by Y. Yoshida and G. Langouche. Singapore: Springer Singapore, 2021, pages 105–171. ISBN: 978-981-15-9422-9. DOI: 10.1007/978-981-15-9422-9_3.

[30] E. Gluskin et al. "A classical Hanbury Brown–Twiss experiment with hard X-rays". In: *Journal of Synchrotron Radiation* 6.5 (Sept. 1999), pages 1065–1066. DOI: 10.1107/S090904959900268X.

[31] Y. Shih. "The Physics of Ghost Imaging". In: *Classical, Semi-classical and Quantum Noise*. Edited by L. Cohen, H. V. Poor, and M. O. Scully. New York, NY: Springer US, 2012, pages 169–222. ISBN: 978-1-4419-6624-7. DOI: 10.1007/978-1-4419-6624-7_14.

[32] J. Javanainen and P. L. Gould. "Linear intensity dependence of a two-photon transition rate". In: *Phys. Rev. A* 41 (9 May 1990), pages 5088–5091. DOI: 10.1103/PhysRevA.41.5088.

[33] S. Tanaka and S. Mukamel. "Coherent X-Ray Raman Spectroscopy: A Nonlinear Local Probe for Electronic Excitations". In: *Phys. Rev. Lett.* 89 (4 July 2002), page 043001. DOI: 10.1103/PhysRevLett.89.043001.

[34] S. Shwartz et al. "X-Ray Parametric Down-Conversion in the Langevin Regime". In: *Phys. Rev. Lett.* 109 (1 July 2012), page 013602. DOI: 10.1103/PhysRevLett.109.013602.

[35] P. Eisenberger and S. L. McCall. "X-Ray Parametric Conversion". In: *Phys. Rev. Lett.* 26 (12 Mar. 1971), pages 684–688. DOI: 10.1103/PhysRevLett.26.684.

[36] Y. Yoda et al. "X-ray parametric scattering by a diamond crystal". In: *Journal of Synchrotron Radiation* 5.3 (May 1998), pages 980–982. DOI: 10.1107/S0909049597020232.

[37] R. Röhlsberger et al. "Collective Lamb Shift in Single-Photon Superradiance". In: *Science* 328.5983 (2010), pages 1248–1251. ISSN: 0036-8075. DOI: 10.1126/science.1187770.

[38] A. I. Chumakov et al. "Superradiance of an ensemble of nuclei excited by a free electron laser". In: *Nature Physics* 14.3 (2018), pages 261–264. DOI: 10.1038/s41567-017-0001-z.

[39] R. Röhlsberger et al. "Electromagnetically induced transparency with resonant nuclei in a cavity". In: *Nature* 482.7384 (2012), pages 199–203. DOI: 10.1038/nature10741.

[40] K. P. Heeg et al. "Vacuum-Assisted Generation and Control of Atomic Coherences at X-Ray Energies". In: *Phys. Rev. Lett.* 111 (7 Aug. 2013), page 073601. DOI: 10.1103/PhysRevLett.111.073601.

[41] K. P. Heeg et al. "Coherent X-ray- optical control of nuclear excitons". In: *Nature* 590.7846 (2021), pages 401–404. DOI: 10.1038/s41586-021-03276-x.

[42] F. Vagizov et al. "Coherent control of the waveforms of recoilless γ-ray photons". In: *Nature* 508.7494 (2014), pages 80–83. DOI: 10.1038/nature13018.

[43] A. Pálffy, C. H. Keitel, and J. Evers. "Single-Photon Entanglement in the keV Regime via Coherent Control of Nuclear Forward Scattering". In: *Phys. Rev. Lett.* 103 (1 July 2009), page 017401. DOI: 10.1103/PhysRevLett.103.017401.

[44] Y. V. Shvyd'ko et al. "Storage of Nuclear Excitation Energy through Magnetic Switching". In: *Phys. Rev. Lett.* 77 (15 Oct. 1996), pages 3232–3235. DOI: 10.1103/PhysRevLett.77.3232.

[45] R. N. Shakhmuratov, F. Vagizov, and O. Kocharovskaya. "Radiation burst from a single γ-photon field". In: *Phys. Rev. A* 84 (4 Oct. 2011), page 043820. DOI: 10.1103/PhysRevA.84.043820.

[46] DESY. *Machine Parameters PETRA III (Design Values)*. http://photon-science.desy.de/facilities/petra_iii/machine/parameters/index_eng.html. Acessed: 08.09.2021.

[47] ESRF. *ID18 - Nuclear Resonance Beamline*. https://www.esrf.fr/home/UsersAndScience/Experiments/MEx/ID18/beamline_layout/optics/xsource.html. Acessed: 14.10.2021.

[48] B. W. McNeil and N. R. Thompson. "X-ray free-electron lasers". In: *Nature photonics* 4.12 (2010), pages 814–821. DOI: 10.1038/nphoton.2010.239.

[49] C. Pellegrini, A. Marinelli, and S. Reiche. "The physics of x-ray free-electron lasers". In: *Rev. Mod. Phys.* 88 (1 Mar. 2016), page 015006. DOI: 10.1103/RevModPhys.88.015006.

[50] C. G. Schroer et al. "PETRA IV: the ultralow-emittance source project at DESY". In: *Journal of Synchrotron Radiation* 25.5 (Sept. 2018), pages 1277–1290. DOI: 10.1107/S1600577518008858.

[51] M. Eriksson et al. "Commissioning of the MAX IV Light Source". In: *Proc. of International Particle Accelerator Conference (IPAC'16), Busan, Korea, May 8-13, 2016* (Busan, Korea). International Particle Accelerator Conference 7. 10.18429/JACoW-IPAC2016-MOYAA01. Geneva, Switzerland: JACoW, June 2016, pages 11–15. ISBN: 978-3-95450-147-2. DOI: 10.18429/JACoW-IPAC2016-MOYAA01.

[52] B. Adams et al. *Scientific Opportunities with an X-ray Free-Electron Laser Oscillator*. 2019. URL: https://arxiv.org/abs/1903.09317.

[53] K. P. Heeg, C. H. Keitel, and J. Evers. *Inducing and detecting collective population inversions of Mössbauer nuclei*. 2016.

[54] A. Junker, A. Pálffy, and C. H. Keitel. "Cooperative effects in nuclear excitation with coherent x-ray light". In: 14.8 (Aug. 2012), page 085025. DOI: 10.1088/1367-2630/14/8/085025.

[55] R. L. Mössbauer. "Kernresonanzfluoreszenz von gammastrahlung in Ir 191". In: *Zeitschrift für Physik* 151.2 (1958), pages 124–143. URL: https://link.springer.com/content/pdf/10.1007/BF01344210.pdf.

[56] R. L. Mössbauer. "Recoilless Nuclear Resonance Absorption of Gamma Radiation". In: *Science* 137.3532 (1962), pages 731–738. DOI: 10.1126/science.137.3532.731.

[57] R. Röhlsberger. *Nuclear condensed matter physics with synchrotron radiation: Basic principles, methodology and applications*. Volume 208. Springer Science & Business Media, 2004. DOI: doi.org/10.1007/b86125.

[58] G. Shirane, D. E. Cox, and S. L. Ruby. "Mössbauer Study of Isomer Shift, Quadrupole Interaction, and Hyperfine Field in Several Oxides Containing Fe^{57}". In: *Phys. Rev.* 125 (4 Feb. 1962), pages 1158–1165. DOI: 10.1103/PhysRev.125.1158.

[59] H. J. Hay et al. "Measurement of the Red Shift in an Accelerated System Using the Mössbauer Effect in Fe^{57}". In: *Phys. Rev. Lett.* 4 (4 Feb. 1960), pages 165–166. DOI: 10.1103/PhysRevLett.4.165.

[60] R. V. Pound and G. A. Rebka. "Gravitational Red-Shift in Nuclear Resonance". In: *Phys. Rev. Lett.* 3 (9 Nov. 1959), pages 439–441. DOI: 10.1103/PhysRevLett.3.439.

[61] C. McCammon. "Mössbauer Spectroscopy with High Spatial Resolution: Spotlight on Geoscience". In: *Modern Mössbauer Spectroscopy: New Challenges Based on Cutting-Edge Techniques*. Edited by Y. Yoshida and G. Langouche. Singapore: Springer Singapore, 2021, pages 221–266. ISBN: 978-981-15-9422-9. DOI: 10.1007/978-981-15-9422-9_5.

[62] F. Wagner and A. Kyek. "Mössbauer spectroscopy in archaeology: introduction and experimental considerations". In: *Hyperfine Interactions* 154.1 (2004), pages 5–33. DOI: 10.1023/B:HYPE.0000032112.94624.95.

[63] V. Schünemann. "From Small Molecules to Complex Systems: A Survey of Chemical and Biological Applications of the Mössbauer Effect". In: *Modern Mössbauer Spectroscopy: New Challenges Based on Cutting-Edge Techniques*. Edited by Y. Yoshida and G. Langouche. Singapore: Springer Singapore, 2021, pages 173–219. ISBN: 978-981-15-9422-9. DOI: 10.1007/978-981-15-9422-9_4.

[64] G. Klingelhöfer et al. "Jarosite and Hematite at Meridiani Planum from Opportunity's Mössbauer Spectrometer". In: *Science* 306.5702 (2004), pages 1740–1745. DOI: 10.1126/science.1104653.

[65] K. P. Heeg et al. "Spectral narrowing of x-ray pulses for precision spectroscopy with nuclear resonances". In: *Science* 357.6349 (2017), pages 375–378. DOI: 10.1126/science.aan3512.

[66] L. von der Wense et al. "Direct detection of the 229 Th nuclear clock transition". In: *Nature* 533.7601 (2016), pages 47–51. DOI: 10.1038/nature17669.

[67] K. P. Heeg and J. Evers. "X-ray quantum optics with Mössbauer nuclei embedded in thin-film cavities". In: *Phys. Rev. A* 88 (4 Oct. 2013), page 043828. DOI: 10.1103/PhysRevA.88.043828.

[68] A. A. Michelson and E. W. Morley. "On the Relative Motion of the Earth and of the Luminiferous Ether". In: *Sidereal Messenger, vol. 6, pp. 306-310* 6 (1887), pages 306–310. URL: http://adsabs.harvard.edu/pdf/1887SidM...6..306M.

[69] L. Zehnder. *Ein neuer Interferenzrefraktor*. 1891.

[70] L. Mach. "Ueber einen Interferenzrefraktor". In: *Zeitschrift für Instrumentenkunde* 12.3 (1892), page 89.

[71] A. Perot and C. Fabry. "On the application of interference phenomena to the solution of various problems of spectroscopy and metrology". In: *The Astrophysical Journal* 9 (1899), page 87. URL: http://adsabs.harvard.edu/pdf/1899ApJ.....9...87P.

[72] O. Carnal and J. Mlynek. "Young's double-slit experiment with atoms: A simple atom interferometer". In: *Phys. Rev. Lett.* 66 (21 May 1991), pages 2689–2692. DOI: 10.1103/PhysRevLett.66.2689.

[73] D. W. Keith et al. "An interferometer for atoms". In: *Phys. Rev. Lett.* 66 (21 May 1991), pages 2693–2696. DOI: 10.1103/PhysRevLett.66.2693.

[74] S. Fray et al. "Atomic Interferometer with Amplitude Gratings of Light and Its Applications to Atom Based Tests of the Equivalence Principle". In: *Phys. Rev. Lett.* 93 (24 Dec. 2004), page 240404. DOI: 10.1103/PhysRevLett.93.240404.

[75] T. L. Gustavson, P. Bouyer, and M. A. Kasevich. "Precision Rotation Measurements with an Atom Interferometer Gyroscope". In: *Phys. Rev. Lett.* 78 (11 Mar. 1997), pages 2046–2049. DOI: 10.1103/PhysRevLett.78.2046.

[76] U. Bonse and M. Hart. "AN X-RAY INTERFEROMETER". In: *Applied Physics Letters* 6.8 (1965), pages 155–156. DOI: 10.1063/1.1754212.

[77] K. Creath. "Phase-Shifting Holographic Interferometry". In: *Holographic Interferometry: Principles and Methods*. Edited by P. K. Rastogi. Berlin, Heidelberg: Springer Berlin Heidelberg, 1994, pages 109–150. ISBN: 978-3-540-48078-5. DOI: 10.1007/978-3-540-48078-5_5.

[78] R. Callens et al. “Phase determination in nuclear resonant scattering using a velocity drive as an interferometer and phase shifter”. In: *Phys. Rev. B* 72 (8 Aug. 2005), page 081402. DOI: 10.1103/PhysRevB.72.081402.

[79] S. Goerttler et al. “Time-Resolved sub-Ångström Metrology by Temporal Phase Interferometry near X-Ray Resonances of Nuclei”. In: *Phys. Rev. Lett.* 123 (15 Oct. 2019), page 153902. DOI: 10.1103/PhysRevLett.123.153902.

[80] H. Takasaki and Y. Yoshino. “Polarization Interferometer”. In: *Appl. Opt.* 8.11 (Nov. 1969), pages 2344–2345. DOI: 10.1364/AO.8.002344.

[81] P. Grangier et al. “Squeezed-light–enhanced polarization interferometer”. In: *Phys. Rev. Lett.* 59 (19 Nov. 1987), pages 2153–2156. DOI: 10.1103/PhysRevLett.59.2153.

[82] K. Okitsu. “Polarization interferometry of X-ray diffraction”. In: *Journal of the Physical Society of Japan* 62.3 (1993), pages 911–917. DOI: 10.1143/JPSJ.62.911.

[83] A. Q. R. Baron et al. “Silicon avalanche photodiodes for direct detection of X-rays”. In: *Journal of Synchrotron Radiation* 13.2 (Mar. 2006), pages 131–142. DOI: 10.1107/S090904950503431X.

[84] H. A. Hauptman. “The phase problem of X-ray crystallography”. In: 54.11 (Nov. 1991), pages 1427–1454. DOI: 10.1088/0034-4885/54/11/002.

[85] D. L. Misell. “A method for the solution of the phase problem in electron microscopy”. In: 6.1 (Jan. 1973), pages L6–L9. DOI: 10.1088/0022-3727/6/1/102.

[86] D. Gabor. “A new microscopic principle”. In: *nature* 161 (1948), pages 777–778.

[87] L. Lepetit, G. Chériaux, and M. Joffre. “Linear techniques of phase measurement by femtosecond spectral interferometry for applications in spectroscopy”. In: *J. Opt. Soc. Am. B* 12.12 (Dec. 1995), pages 2467–2474. DOI: 10.1364/JOSAB.12.002467.

[88] E. Tokunaga, A. Terasaki, and T. Kobayashi. “Frequency-domain interferometer for femtosecond time-resolved phase spectroscopy”. In: *Opt. Lett.* 17.16 (Aug. 1992), pages 1131–1133. DOI: 10.1364/OL.17.001131.

[89] W. Sturhahn. “Phase problem in synchrotron Mössbauer spectroscopy”. In: *Phys. Rev. B* 63 (9 Jan. 2001), page 094105. DOI: 10.1103/PhysRevB.63.094105.

[90] J. F. A. Haber. “Hard X-ray quantum optics in thin-film nanostructures”. PhD thesis. Universität Hamburg, 2016. DOI: 10.3204/PUBDB-2017-02595.

[91] E. Marsh and R. Grejda. “Experiences with the master axis method for measuring spindle error motions”. In: *Precision Engineering* 24.1 (2000), pages 50–57. ISSN: 0141-6359. DOI: 10.1016/S0141-6359(99)00027-6.

[92] C. Regal, J. Teufel, and K. Lehnert. "Measuring nanomechanical motion with a microwave cavity interferometer". In: *Nature Physics* 4.7 (2008), pages 555–560. DOI: 10.1038/nphys974.

[93] M. Aspelmeyer, T. J. Kippenberg, and F. Marquardt. "Cavity optomechanics". In: *Rev. Mod. Phys.* 86 (4 Dec. 2014), pages 1391–1452. DOI: 10.1103/RevModPhys.86.1391.

[94] M. L. Gerharz. "Dynamical polarization control in X-ray quantum optics". Bachelor's Thesis. Ruprecht-Karls-Universität Heidelberg, 2019. URL: https://pure.mpg.de/pubman/faces/ViewItemOverviewPage.jsp?itemId=item_3117611.

[95] M. L. Gerharz and J. Evers. "Fast resonant adaptive x-ray optics via mechanically-induced refractive-index enhancement". in prep.

[96] S. G. Alcock et al. "Dynamic adaptive X-ray optics. Part I. Time-resolved optical metrology investigation of the bending behaviour of piezoelectric bimorph deformable X-ray mirrors". In: *Journal of Synchrotron Radiation* 26.1 (Jan. 2019), pages 36–44. DOI: 10.1107/S1600577518015953.

[97] D. Mukhopadhyay et al. "X-ray photonic microsystems for the manipulation of synchrotron light". In: *Nature communications* 6.1 (2015), pages 1–7. DOI: 10.1038/ncomms8057.

[98] P. Chen et al. "Ultrafast photonic micro-systems to manipulate hard X-rays at 300 picoseconds". In: *Nature communications* 10.1 (2019), pages 1–9. DOI: 10.1038/s41467-019-09077-1.

[99] T. S. Toellner et al. "Synchrotron Mössbauer spectroscopy using high-speed shutters". In: *Journal of Synchrotron Radiation* 18.2 (Mar. 2011), pages 183–188. DOI: 10.1107/S090904951003863X.

[100] V. Dmitrienko and V. Belyakov. "Polarisation conversion of X-rays in single crystals". In: *Sov. Tech. Phys. Lett* 6 (1980), pages 621–622.

[101] I. Polikarpov. "Adjustable x-ray phase plate and phase modulator". In: *Applied Physics Letters* 73.15 (1998), pages 2096–2097. DOI: 10.1063/1.122389.

[102] E. Zolotoyabko and J. P. Quintana. "Control of synchrotron x-ray diffraction by means of standing acoustic waves". In: *Review of Scientific Instruments* 75.3 (2004), pages 699–708. DOI: 10.1063/1.1645652.

[103] A. Grigoriev et al. "Subnanosecond piezoelectric x-ray switch". In: *Applied Physics Letters* 89.2 (2006), page 021109. DOI: 10.1063/1.2219342.

[104] M. Sander et al. "Demonstration of a picosecond Bragg switch for hard X-rays in a synchrotron-based pump–probe experiment". In: *Journal of Synchrotron Radiation* 26.4 (July 2019), pages 1253–1259. DOI: 10.1107/S1600577519005356.

[105] S. Sakshath et al. "Optical pump - nuclear resonance probe experiments on spin crossover complexes". In: *Hyperfine Interactions* 238.1 (2017), page 89. DOI: 10.1007/s10751-017-1461-3.

[106] R. Azzam. "Polarization Michelson interferometer (POLMINT): its use for polarization modulation and temporal pulse shearing". In: *Optics Communications* 98.1 (1993), pages 19–23. ISSN: 0030-4018. DOI: https://doi.org/10.1016/0030-4018(93)90751-P.

[107] P. Helistö et al. "Gamma echo". In: *Phys. Rev. Lett.* 66 (15 Apr. 1991), pages 2037–2040. DOI: 10.1103/PhysRevLett.66.2037.

[108] P. Schindelmann et al. "Radiative decoupling and coupling of nuclear oscillators by stepwise Doppler-energy shifts". In: *Phys. Rev. A* 65 (2 Jan. 2002), page 023804. DOI: 10.1103/PhysRevA.65.023804.

[109] R. N. Shakhmuratov, F. Vagizov, and O. Kocharovskaya. "Single gamma-photon revival from sandwich absorbers". In: *Phys. Rev. A* 87 (1 Jan. 2013), page 013807. DOI: 10.1103/PhysRevA.87.013807.

[110] P. H. van den Heuvel. "Arbitrary phase control of X-ray pulses with zeptosecond phase stability". https://pure.mpg.de/pubman/faces/ViewItemOverviewPage.jsp?itemId=item_3324046. Master's thesis. Ruprecht-Karls-Universität Heidelberg, 2021.

[111] D. Allan. "Statistics of atomic frequency standards". In: *Proceedings of the IEEE* 54.2 (1966), pages 221–230. DOI: 10.1109/PROC.1966.4634.

[112] K. P. Heeg. private communication.

[113] W. Sturhahn. "CONUSS and PHOENIX: Evaluation of nuclear resonant scattering data". In: *Hyperfine Interactions* 125.1 (2000), pages 149–172. DOI: 10.1023/A:1012681503686.

[114] K. P. Heeg. "X-Ray quantum optics with Mössbauer nuclei in thin-film cavities". PhD thesis. University of Heidelberg, 2014. DOI: 10.11588/heidok.00017869.

[115] J. Mendez-Garza et al. "Synthesis and surface modification of spindle-type magnetic nanoparticles: gold coating and PEG functionalization". In: *Journal of Biomaterials and Nanobiotechnology* 4 (2013), pages 222–228. DOI: 10.4236/jbnb.2013.43027.

[116] DESY. *P01 High Resolution Dynamics Beamline*. https://photon-science.desy.de/facilities/petra_iii/beamlines/p01_dynamics/index_eng.html. Acessed: 14.10.2021.

[117] M. O. Scully et al. "Directed Spontaneous Emission from an Extended Ensemble of N Atoms: Timing Is Everything". In: *Phys. Rev. Lett.* 96 (1 Jan. 2006), page 010501. DOI: 10.1103/PhysRevLett.96.010501.

[118] G. Smirnov. "Nuclear resonant scattering of synchrotron radiation". In: *Hyperfine Interactions* 97.1 (1996), pages 551–588. DOI: 10.1007/BF02150198.

[119] P. Reiser. "Time domain control of x-ray quantum dynamics". Master's thesis. Ruprecht-Karls-Universität Heidelberg, 2014.

[120] B. Herkommer. "Measuring the energy spectra of unknown samples using coherent control of the complex phase of X-rays". Master's thesis. Ruprecht-Karls-Universität Heidelberg, 2019. URL: https://pure.mpg.de/pubman/faces/ViewItemOverviewPage.jsp?itemId=item_3192911.

[121] B. E. Saleh and M. C. Teich. *Fundamentals of photonics*. john Wiley & sons, 2019.

[122] D. P. Siddons, U. Bergmann, and J. B. Hastings. "Polarization effects in resonant nuclear scattering". In: *Hyperfine Interactions* 123.1 (1999), pages 681–719. DOI: 10.1023/A:1017096512347.

[123] S. P. Division. *Piezo Film Sensors Technical Manual P/N 1005663-1 REV B*. Measurement Specialities Inc. URL: http://www.ehag.ch/PDF-Files/MSI/techman.pdf.

[124] *Keysight 81150A and 81160A Pulse Function Arbitrary Noise Generators*. Keysight Technologies. URL: https://www.keysight.com/de/de/assets/7018-01537/data-sheets/5989-6433.pdf.

[125] D. Lentrodt. "Ab initio approaches to x-ray cavity QED". PhD thesis. University of Heidelberg, 2021. URL: https://pure.mpg.de/pubman/faces/ViewItemOverviewPage.jsp?itemId=item_3347524.

[126] S. McKinley and M. Levine. *Cubic spline interpolation*. https://mse.redwoods.edu/darnold/math45/laproj/Fall98/SkyMeg/Proj.PDF. Lecture Notes. Acessed: 24.09.2021. 1998.

[127] D. M. Olsson and L. S. Nelson. "The Nelder-Mead Simplex Procedure for Function Minimization". In: *Technometrics* 17.1 (1975), pages 45–51. DOI: 10.1080/00401706.1975.10489269.

[128] I. Rechenberg. "Evolutionsstrategien". In: *Simulationsmethoden in der Medizin und Biologie*. Edited by B. Schneider and U. Ranft. Berlin, Heidelberg: Springer Berlin Heidelberg, 1978, pages 83–114. ISBN: 978-3-642-81283-5. DOI: 10.1007/978-3-642-81283-5_8.

[129] C. A. Coello Coello. "An Introduction to Evolutionary Algorithms and Their Applications". In: *Advanced Distributed Systems*. Edited by F. F. Ramos, V. Larios Rosillo, and H. Unger. Berlin, Heidelberg: Springer Berlin Heidelberg, 2005, pages 425–442. ISBN: 978-3-540-31674-9. DOI: 10.1007/11533962_39.

[130] J. J. Moré. "The Levenberg-Marquardt algorithm: implementation and theory". In: *Numerical analysis*. Springer, 1978, pages 105–116. URL: https://link.springer.com/content/pdf/10.1007/BFb0067700.pdf.

[131] J. C. Lagarias et al. "Convergence properties of the Nelder–Mead simplex method in low dimensions". In: *SIAM Journal on optimization* 9.1 (1998), pages 112–147. DOI: 10.1137/S1052623496303470.

[132] T. Schoonjans et al. “The xraylib library for X-ray–matter interactions. Recent developments”. In: *Spectrochimica Acta Part B: Atomic Spectroscopy* 66.11 (2011), pages 776–784. ISSN: 0584-8547. DOI: 10.1016/j.sab.2011.09.011.

[133] T. Mitsui et al. “^{5}7Fe polarization-dependent synchrotron Mössbauer spectroscopy using a diamond phase plate and an iron borate nuclear Bragg monochromator”. In: *Journal of Synchrotron Radiation* 22.2 (Mar. 2015), pages 427–435. DOI: 10.1107/S1600577514028306.

[134] B. Marx-Glowna et al. “Advanced X-ray polarimeter design for nuclear resonant scattering”. In: *Journal of Synchrotron Radiation* 28.1 (Jan. 2021), pages 120–124. DOI: 10.1107/S1600577520015295.

Erklärung:

Ich versichere, dass ich diese Arbeit selbstständig verfasst habe und keine anderen als die angegebenen Quellen und Hilfsmittel benutzt habe.

Heidelberg, den 01.11.2021 ..... Miriam Gerlach .....